MECHFAIL: A TOTAL-SYSTEM PERFORMANCE ASSESSMENT CODE MODULE FOR EVALUATING ENGINEERED BARRIER PERFORMANCE UNDER MECHANICAL LOADING CONDITIONS

Prepared for

U.S. Nuclear Regulatory Commission
Contract NRC–02–02–012

Prepared by

G. Douglas Gute, Goodluck Ofoegbu, Fernand Thomassy, Sui-Min Hsiung, George Adams, Amitava Ghosh, Biswajit Dasgupta, Asadul H. Chowdhury, and Sitakanta Mohanty

Center for Nuclear Waste Regulatory Analyses
San Antonio, Texas

November 2002

PREVIOUS REPORT IN SERIES

Name	Date
Assessment of Mechanical Response of Drip Shields Under Repository Environment—Progress Report	May 2000
Assessment of Mechanical Response of Drip Shields Under Repository Environment—Progress Report 2	November 2001

ABSTRACT

The objective of this study was to develop an approach for estimating the potential number of drip shield and waste package failures attributable to rockfall and seismic events over the 10,000-year regulatory period of interest. To meet this objective, a framework was developed for a new Total-system Performance Assessment code module (MECHFAIL) designed to assess the effects of mechanical loading (i.e., static and dynamic rockfall loads and seismicity) on the engineered barrier subsystem. This module includes abstractions that can be used to assess (i) the spatial and temporal distributions of rockfall loads, both static and dynamic; (ii) the number of individual seismic events that can be expected to occur during the regulatory period and the characterization of their respective ground motion time histories (i.e., peak ground accelerations); (iii) the mechanical effects of rockfall and seismic loads on the drip shields and waste packages: and (iv) the applicable failure mechanisms and their respective failure criteria. These individual abstractions have been incorporated into the MECHFAIL module so the potential number of drip shield and waste package failures attributable to rockfall and seismic events for the 10,000-year regulatory period of interest can be calculated and provided as input to the Total-system Performance Assessment code. The effects of material and structural degradation caused by various corrosion processes (including stress corrosion cracking), fabrication flaws, weld residual stresses, hydrogen embrittlement, and so on are not considered at the present time.

Potential failure mechanisms of the drip shield that have been accounted for in the MECHFAIL module include accumulated equivalent plastic strains that exceed the allowable ductility of the drip shield materials (i.e., the Titanium Grade 7 plates and Titanium Grade 24 bulkheads) attributable to dynamic rock block impacts and creep caused by static rockfall loads. The potential for drip shield buckling under static rockfall loads and seismic excitation is accounted for as well. Although the abstractions have yet to be completed, the MECHFAIL module includes placeholders for assessing waste package damage caused by direct seismic shaking and interactions with the drip shield caused by static and dynamic rockfall loads. As with the drip shield, the damage incurred by the waste package outer barrier is characterized in terms of the accumulated equivalent plastic strain. The von Mises stress of the waste package outer barrier is also evaluated to facilitate the assessment of stress corrosion cracking as a potential failure mechanism. Failure of the drift by thermal, mechanical, hydrological, and chemical degradation processes has been accounted for using a time-based drift degradation rate. In addition, the effects of seismic events, which occur at discrete times, on drift degradation have been explicitly included in the MECHFAIL module. The time-varying aspects of drift degradation are correlated with the accumulation of static rockfall loads and occurrence of dynamic rockfall loads acting on the drip shield.

Assuming an elliptical drift degradation geometry and bulking factors within the range of 1.15 to 1.5, it was demonstrated that the bounding static rockfall loads will lie somewhere in the range of 40 to 160 tonne/m [26,890 to 107,550 lb/ft] along the length of the drift. It has been assumed that these loads will fully manifest themselves within the first 1,000 years after cessation of maintenance of the ground support system. The basis for this assumption is provided in the report. The methodology used to derive the distribution of rock block sizes within the lower lithophysal and middle nonlithophysal rock units is presented as well. It was determined, because of its highly fractured nature, that the formation of discrete rock blocks of any consequence within the lower lithophysal rock unit is unlikely. The analysis of the middle

nonlithophysal rock unit, however, indicated that there are rock blocks of sufficient size to cause damage to the drip shield and, potentially, the waste package (by driving the drip shield into the waste package after impact). The distribution of rock block sizes within the middle nonlithophysal rock unit is such that approximately 60 percent will have a volume less than 1 m^3 [35.3 ft^3], which corresponds to a rock block mass of 2.7 tonne [5,955 lb] {assuming a rock mass density of 2.7 tonne/m^3 [169 lb/ft^3]}. Twenty-five percent have a volume of 1 to 2 m^3 [35.3 to 70.6 ft^3] {2.7 to 5.4 tonne [5,955 to 11,910 lb]} and the remaining15 percent have a volume greater than 2 m^3 [70.6 ft^3] {5.4 tonne [11,910 lb]}.

The results obtained from finite element models of the drip shield subjected to static rockfall loads indicate that the drip shield may buckle under loads as small as 23 tonne/m [15,460 lb/ft]. Moreover, static rockfall loads sufficient to initiate creep of the drip shield Titanium Grade 7 plate can be as low as 15 tonne/m [10,083 lb/ft] and, for the Titanium Grade 24 bulkhead, 20 tonne/m [13,444 lb/ft]. These threshold loads were found to increase significantly if credit is taken for the structural support provided by the accumulated rockfall rubble that builds up around the drip shield side walls. How much credit to take for the in the presence of rock rubble accumulated around the drip shield side walls was difficult to quantify, however, because of the sensitivity of the buckling and creep threshold loads to the effective Young's modulus assumed for the accumulated rockfall rubble. As a result, a beta function defining the drip shield buckling load was generated. This curve was created assuming that the drip shield will not buckle under static rockfall loads less than 25 tonne/m [16,800 lb/ft] and no more than 20 percent of the drip shields will have a buckling load threshold greater than 60 tonne/m [40,330 lb/ft]. Preliminary MECHFAIL analyses indicate that approximately 75 percent of the drip shields will fail from buckling under static rockfall loads 520 years after cessation of maintenance of the ground support system.

The work related to the development of MECHFAIL is intended to facilitate the completion of the various Key Technical Issue agreements between the U.S. Department of Energy and U.S. Nuclear Regulatory Commission that pertain to the performance assessment of the engineered barrier subsystem when subjected to rockfall and seismic ground motions.

3/72

CONTENTS

CONTENTS (Continued)

4/72

CONTENTS (Continued)

5/72

FIGURES

FIGURES (Continued)

FIGURES (Continued)

TABLES

ACKNOWLEDGMENTS

This report was prepared to document work performed by the Center for Nuclear Waste Regulatory Analyses (CNWRA) for the U.S. Nuclear Regulatory Commission (NRC) under Contract No. NRC–02–02–012. The activities reported here were performed on behalf of the NRC Office of Nuclear Material Safety and Safeguards, Division of Waste Management. The report is an independent product of the CNWRA and does not necessarily reflect the views or regulatory position of the NRC.

The authors thank W. Patrick and B. Sagar for their reviews of this report. The authors are thankful to A. Ramos for assisting with the word processing and preparation of the final report and to C. Cudd, A. Woods, and J. Pryor for the editorial review.

QUALITY OF DATA, ANALYSES, AND CODE DEVELOPMENT

DATA: All CNWRA-generated original data contained in this report meet quality assurance requirements described in the CNWRA Quality Assurance Manual. Sources for other data should be consulted for determining the level of quality for those data. The work presented in this report is documented in CNWRA Scientific Notebooks 391, 409, 410, 417, and 422.

ANALYSES AND CODES: Finite element analyses in this report were conducted by the CNWRA using the commercial computer codes ABAQUS/Standard and ABAQUS/Explicit Versions 5.8–16 and 6.2. Pre- and post-processing of the finite element models were accomplished using the commercial computer code ABAQUS/CAE, and HyperMesh. ABAQUS/Standard, ABAQUS/Explicit, ABAQUS/CAE, and HyperMesh are controlled under the CNWRA software Quality Assurance procedure (TOP–018, Development and Control of Scientific and Engineering Software). Spreadsheet calculations were accomplished using Microsoft® Excel 97 SR–2. Additional calculations were performed using Mathcad 2000 Professional.

1 INTRODUCTION

1.1 Background

The U.S. Department of Energy (DOE) has been studying the Yucca Mountain site in Nevada for more than 15 years to determine whether it is suitable for building a geologic repository for the nation's spent nuclear fuel and high-level waste (DOE, 1998a). The proposed repository design employs an engineered barrier subsystem in concert with the desert environment and geologic features of Yucca Mountain to limit water contacting the spent nuclear fuel and high-level waste for thousands of years. Two primary components of the engineered barrier subsystem are the drip shield and waste package (CRWMS M&O, 1999a). Other potential components of the engineered barrier subsystem include backfill and emplacement drift seals. The basic concept of geologic disposal at Yucca Mountain is the placement of carefully prepared and packaged nuclear waste in excavated tunnels in tuff about 350 m [1,148 ft] below the surface and 225 m [738 ft] above the water table. In this condition, the engineered barriers are intended to work with the natural barriers—the geology and climate of Yucca Mountain—to contain and isolate the nuclear waste for thousands of years. For example, the evolving engineered barrier component designs include materials chosen to be compatible with the underground thermal and geochemical environment, and the layout of tunnels takes into consideration the geology of the mountain (DOE, 1998a).

Through successive evaluations, the repository design evolved to the Viability Assessment reference design (DOE, 1998a,b). This reference design represented a snapshot of the ongoing design process, thus providing a frame of reference to describe how the proposed repository at Yucca Mountain could work. Following the presentation of the Viability Assessment reference design for the proposed repository to the U.S. Congress, the License Application Design Selection was completed by the DOE (CRWMS M&O, 1999a,b,c). The goal of the License Application Design Selection was to develop and evaluate a diverse range of conceptual repository designs that would be compatible with the geologic attributes of the Yucca Mountain site and to recommend an initial design concept for the possible Site Recommendation and License Application documents. Ultimately, the potential benefits of five variations of the Viability Assessment reference design were studied to identify design attributes that could improve the functional characteristics of the proposed repository. A new repository reference design has been adopted by the DOE as a consequence. This new design, referred to as Enhanced Design Alternative II, uses more extensive thermal management techniques than the Viability Assessment design to redirect water flow through the rock mass between the emplacement drifts (CRWMS M&O, 1999b). The new Enhanced Design Alternative II design also differs from the Viability Assessment design in that steel structural materials are now primarily used in the drifts instead of concrete to avoid possible adverse chemical reactions pertaining to corrosion, as well as mobilization and movement of radionuclides.

The repository design strategy has been brought further into focus by the Yucca Mountain Science and Engineering Report (CRWMS M&O, 2001). For example, the initial intent and design functionality of the drip shield was limited to protecting the waste package from dripping water originating from the drift ceiling. As documented in the Yucca Mountain Science and Engineering Report, however, DOE is currently attempting to design the drip shield to protect the waste package from all potential rockfall loads (i.e., both static and dynamic) and, as a result, limit the potential number of waste packages that may be breached because of this form

of mechanical disruption (CRWMS M&O, 2001). Static rockfall loads are caused by the accumulation of discrete rock blocks and rubble that have fallen from the drift ceiling over time. Dynamic rockfall loads occur when individual discrete rock blocks are dislodged from the drift ceiling and free-fall until impacting the drip shield. The seismic hazard curve is an important input parameter for approximating the occurrence of rockfall in the emplacement drifts because of earthquake-induced ground shaking.

In addition to rockfall, other credible mechanically disruptive events include seismicity, faulting, and igneous activity. With regard to seismic effects alone, two potential failure mechanisms have been identified. Depending on the peak ground acceleration of the seismic event and the concomitant dynamic response of the drip shield and waste package, stresses sufficient to cause localized plastic deformations may occur. The occurrence of plastic deformations implies the existence of residual stresses that are sufficient for stress corrosion cracking to occur. It has not been definitively established, however, whether the environment within the emplacement drifts is conducive to stress corrosion cracking. Accumulated plastic strains caused by repeated seismic events represents the other potential failure mechanism.

Even though the presence of engineered or naturally occurring backfill (i.e., accumulated rockfall rubble) significantly reduces the fault displacement magnitude needed to exert loads on the drip shield and waste package, the expected magnitudes of fault displacement will not cause significant drip shield or waste package damage. In addition, as an extra mitigative design feature, no waste packages will be emplaced near any known faults. The closest a waste package can be emplaced to a known fault is called the fault-setback distance. Moreover, the potential effect of faulting on the drip shield is likely to be limited to the misalignment of adjacent drip shield units. The extent of the water infiltration pathways created from this misalignment is expected to be small and, given the limited spatial occurrence of faulting and the aforementioned fault-setback requirement, the potential effects of fault slip on drip shield and waste package performance is considered to be negligible.

The abstractions required to characterize the occurrence and consequences of igneous intrusion are unique and unrelated to structural deformation (i.e., in the geological sense) and seismicity. As a result, this mechanically disruptive event is addressed separately and is outside the scope of work addressed in this report.

1.2 Objective and Scope

The objective of this study is to develop an approach for estimating the potential number of drip shield and waste package failures attributable to rockfall and seismic events over the 10,000-year regulatory period of interest. Meeting this objective requires the development of quantitative functions, commonly referred to as abstractions, that can be used to assess (i) the spatial and temporal distributions of rockfall loads, both static and dynamic; (ii) the number of individual seismic events that can be expected to occur during the regulatory period and the characterization of their respective ground motion time histories (i.e., peak ground accelerations, peak ground velocities, frequency response spectrums, energy density functions); (iii) the mechanical effects of rockfall and seismic loads on the drip shields and waste packages; and (iv) the applicable failure mechanisms and their respective failure criteria. These individual abstractions will be incorporated into the MECHFAIL module such that the potential number of drip shield and waste package failures attributable to rockfall and seismic

events over the 10,000-year regulatory period of interest can be calculated and provided as input to the Total-system Performance Assessment code. It is important to note that the effects of material and structural degradation caused by various corrosion processes (including stress corrosion cracking), fabrication flaws, weld residual stresses, hydrogen embrittlement, are not considered at this time.

The scope of this report encompasses the following:

- Overview of the conceptual design of the MECHFAIL program module
- The technical basis and abstraction methodology for approximating the number of seismic events and their respective peak ground acceleration during the 10,000-year regulatory period
- The development of the abstractions used to approximate the spatial and temporal distributions of static and dynamic rockfall loads
- Performance analyses of the drip shield subjected to static rockfall loads (process level model results and abstractions)
- Performance analyses of the drip shield and waste package interaction caused by static rockfall loads (process level model results and abstractions)
- Performance analyses of the drip shield subjected to dynamic rockfall loads (process level model results and abstractions)
- Natural frequency and mode shape analyses for the drip shield

The scope of the work is sufficient to facilitate the completion of the various key technical issue agreements that have been made between the DOE and U.S. Nuclear Regulatory Commission that pertain to the performance assessment of the engineered barrier subsystem when subjected to rockfall and seismic ground motions. The specific key technical issue agreements relevant to the work documented in this report are identified in Table 1-1. The full text of the agreements identified in Table 1-1 can be found in Appendix A.

Table 1-1. Related Key Technical Issue Subissues and Agreements			
Key Technical Issue	**Subissue**	**Status**	**Related Agreements***
Container Life and Source Term	Subissue 1—Effects of Corrosion Processes on the Lifetime of the Containers	Closed-Pending	CLST.1.14
	Subissue 2—Effects of Phase Instability of Materials and Initial Defects on the Mechanical Failure and Lifetime of the Containers	Closed-Pending	CLST.2.02 CLST.2.06 CLST.2.08
	Subissue 3—The Rate at Which Radionuclides in Spent Nuclear Fuel Are Released from the Engineered Barrier Subsystem Through the Oxidation and Dissolution of Spent Nuclear Fuel	Closed-Pending	CLST.3.10
Repository Design and Thermal-Mechanical Effects	Subissue 3—Thermal-Mechanical Effects	Closed-Pending	RDTME.3.17 RDTME.3.19
Structural Deformation and Seismicity	Subissue 2—Seismicity	Closed-Pending	SDS.2.04
Total System Performance Assessment and Integration	Subissue 2—Scenario Analysis and Event Probability	Closed-Pending	TSPAI.2.02 (Comments 34, 35, 37, 39, 78, and 79)
	Subissue 3—Model Abstraction	Closed-Pending	TSPAI.3.06

*Key Technical Issue Agreement GEN.1.01 (Comment 3) pertains to multiple integrated subissues, as well as some specific issues related to this integrated subissue.

2 OVERVIEW OF THE MECHFAIL TOTAL-SYSTEM PERFORMANCE ASSESSMENT MODULE

The MECHFAIL Total-system Performance Assessment code module is organized on a spatial grid element basis. The spatial grid elements are discrete subdivisions of the repository footprint. For the Total-system Performance Assessment code Version 5.0 beta, each of the 10 standard subareas utilized within the code have been further divided within MECHFAIL using two spatial grid elements per subarea. Each grid element within a given subarea represents the spatial volume percentage of lithophysal and nonlithophysal rock units. Therefore, MECHFAIL is comprised of 20 spatial grid elements with each grid element assigned various properties and parameters consistent with the rock unit it is intended to represent as described in subsequent chapters of this report.

In a given time increment, each spatial grid element will experience some amount of rockfall caused by thermal, mechanical, hydrological, and chemical drift degradation processes. The specific amount of rockfall that occurs over the time increment is determined by the drift degradation rate of the spatial grid element. As explained in more detail in Section 4.1, the drift degradation rate of each spatial grid element depends on the drift degradation time and the maximum drift degradation zone failure height assigned to the spatial grid element. Additional rockfall attributed to discrete seismic events is also accounted for (see Section 4.2). Dynamic rock block impact loads acting on the engineered barrier subsystem (i.e., the drip shield and waste package) are assumed to occur only when there is a seismic event (see Section 4.2.2). In addition, it has been assumed that the effects of dynamic rock block impacts on the engineered barrier subsystem will be mitigated when the drip shield crown becomes buried under a 0.5-m [1.6-ft] depth of rockfall rubble. Analyses have yet to be performed to justify this assumption, however. Although the effects of dynamic rock block loads on the engineered barrier subsystem are no longer assessed once the accumulated rockfall rubble exceeds this threshold, its contribution to the static rockfall load is still accounted for. The drift degradation zone failure height that corresponds to the amount of rockfall that is needed to mitigate the effects of dynamic rock block impact loads is referred to as the impact mitigation height. Lastly, additional accumulation of rockfall rubble is not allowed after the maximum drift degradation failure zone height is reached (see Section 4.1). In other words, static rockfall loads are bounded using the conservation of mass principle described in Section 4.1.

Failure of the individual components of the engineered barrier subsystem (i.e., drip shield and waste package) caused by static and dynamic rockfall loads and direct seismic shaking is achieved when the accumulated equivalent plastic strains for a given material exceeds the minimum allowable percentage of elongation as defined by the appropriate ASTM International Standard or, in the case of the drip shield, when structural buckling occurs. Equivalent plastic strain is analogous to von Mises stress in that it is the uniaxial equivalent of a three-dimensional state of plastic strain. Total equivalent plastic strain was chosen as the failure parameter because it facilitates the accumulation of damage created by discrete events. For example, discrete rock block impacts with the drip shield will cause large variations in stress (i.e., the stress at the maximum displacement relative to the residual stress level after elastic recovery within the drip shield components). The total strain (i.e., the sum of elastic and plastic strain) within the drip shield, however, is dominated by the plastic strain. Any reduction in total strain attributable to elastic recovery is, from a practical engineering point of view, negligible. Furthermore, because the effects of strain hardening (i.e., increases in yield stress) are not

accounted for in the drip shield or waste package material damage abstractions from one event to the next, any potential errors or uncertainties should be adequately bounded. A more refined approach for assessing the accumulated damage to the drip shield created by dynamic rock block impacts and creep can be developed if it is found that the current method results in these particular failure mechanisms being risk significant.

Figure 2-1 is a flow chart illustrating the overall functionality of the MECHFAIL module. As can be seen, the framework for evaluating the effects of both static and dynamic rockfall and direct seismic shaking on the engineered barrier subsystem has been completed. Abstractions for assessing the damage to the drip shield for both static and dynamic rockfall loads have been completed and implemented within the MECHFAIL Module subroutine PROCESSELEMENTS (see Figure 2-2). These abstractions include the effective increase in static rockfall loads that occur during a seismic event (see Section 5.3.1). Abstractions of potential drip shield and waste package interactions for both static and dynamic rockfall loads have yet to be completed, however. The abstraction of the effects of direct seismic shaking of the waste package for varying earthquake magnitudes is still under development as well. Creep of the various titanium alloys used in the construction of the drip shield is evaluated if the stress within the individual drip shield components from the static rockfall loads exceed the requisite threshold (see Section 5.3.2).

The MECHFAIL module interfaces to the Total-system Performance Assessment code through the executive module (EXEC). MECHFAIL receives the Total-system Performance Assessment timesteps and the distribution of seismic events throughout these timesteps from the executive module. The MECHFAIL module also receives a drip shield thickness versus time distribution by way of the executive module, but this distribution is not used within MECHFAIL at the present time. Additional analyses of the drip shield in various stages of material degradation are required before relationships correlating rockfall loads and drip shield thickness with drip shield failures can be formulated. MECHFAIL returns information to the executive module that corresponds to the Total-system Performance Assessment code timesteps it received. The results returned to the Total-system Performance Assessment code via the executive module are the fraction of drip shields, waste packages, and drifts that have failed and the waste package outer barrier stress. The waste package outer barrier stress may be used in future revisions of the Total-system Performance Assessment code to assess the potential effects of stress corrosion cracking. Similarly, the percentage of drift failures can be used to assess the potential effects of increased seepage into the drifts.

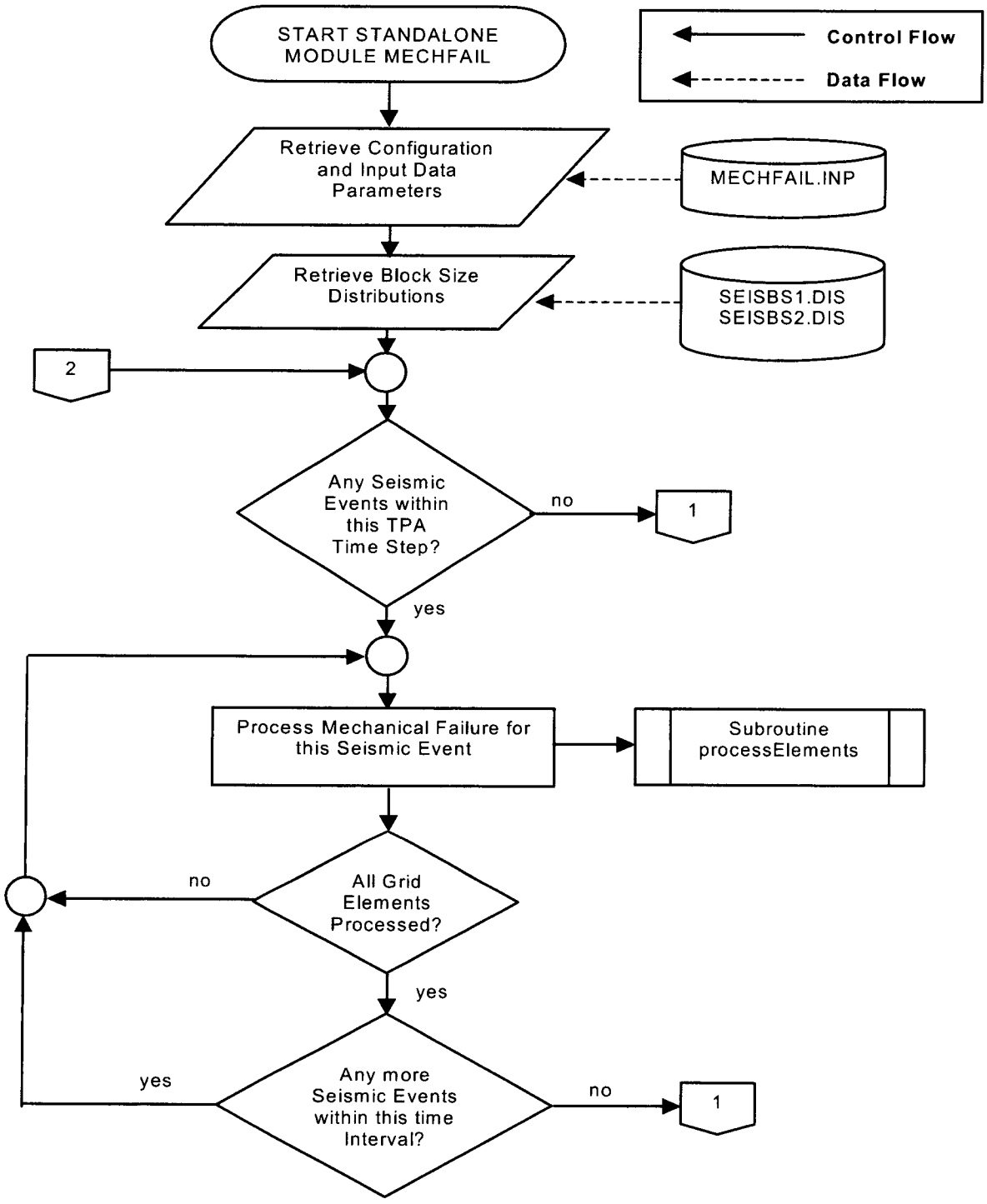

Figure 2-1. Flowchart of the MECHFAIL Module

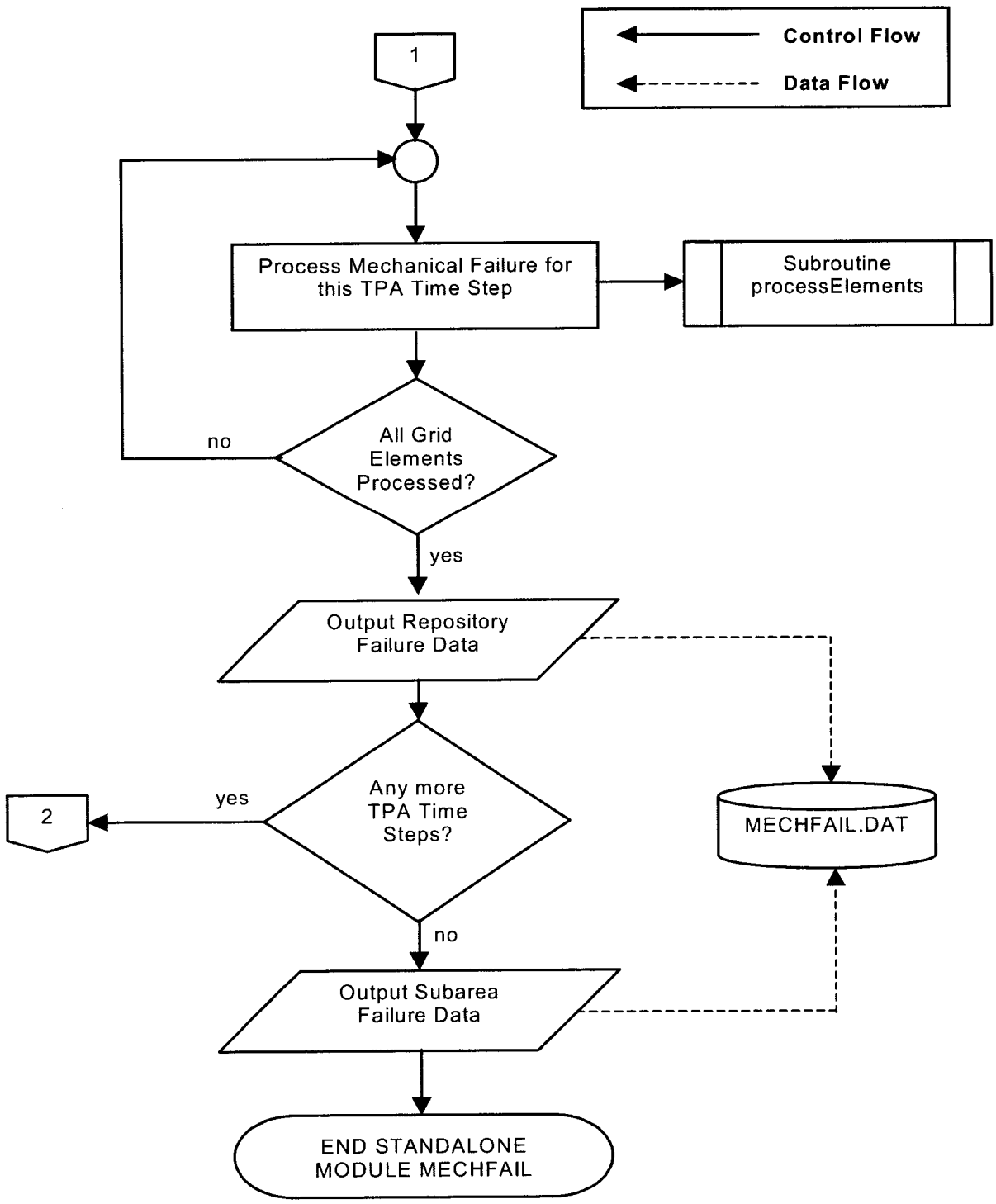

Figure 2-1. Flowchart of the MECHFAIL Module (Continued)

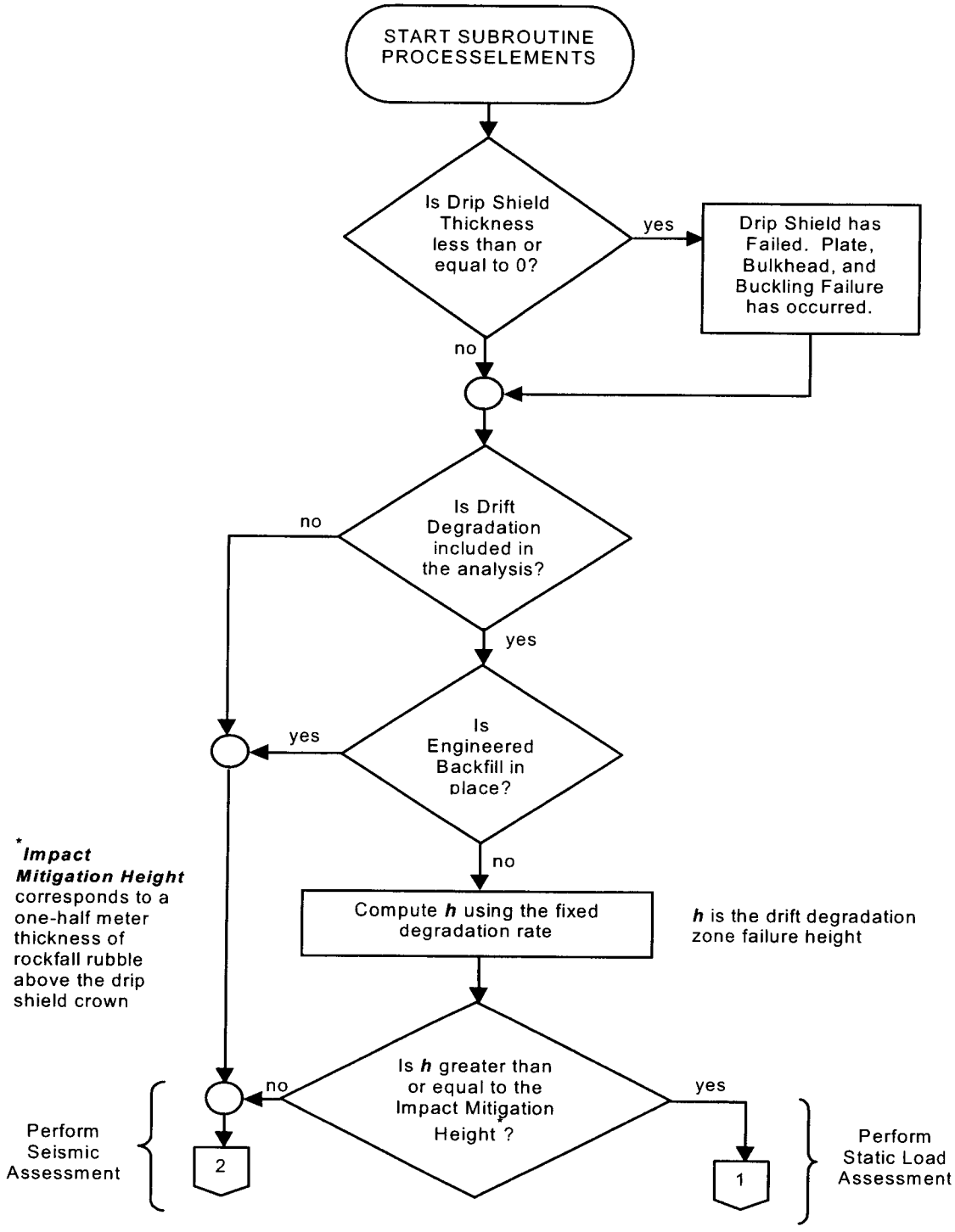

Figure 2-2. Flowchart of the PROCESSELEMENTS Subroutine

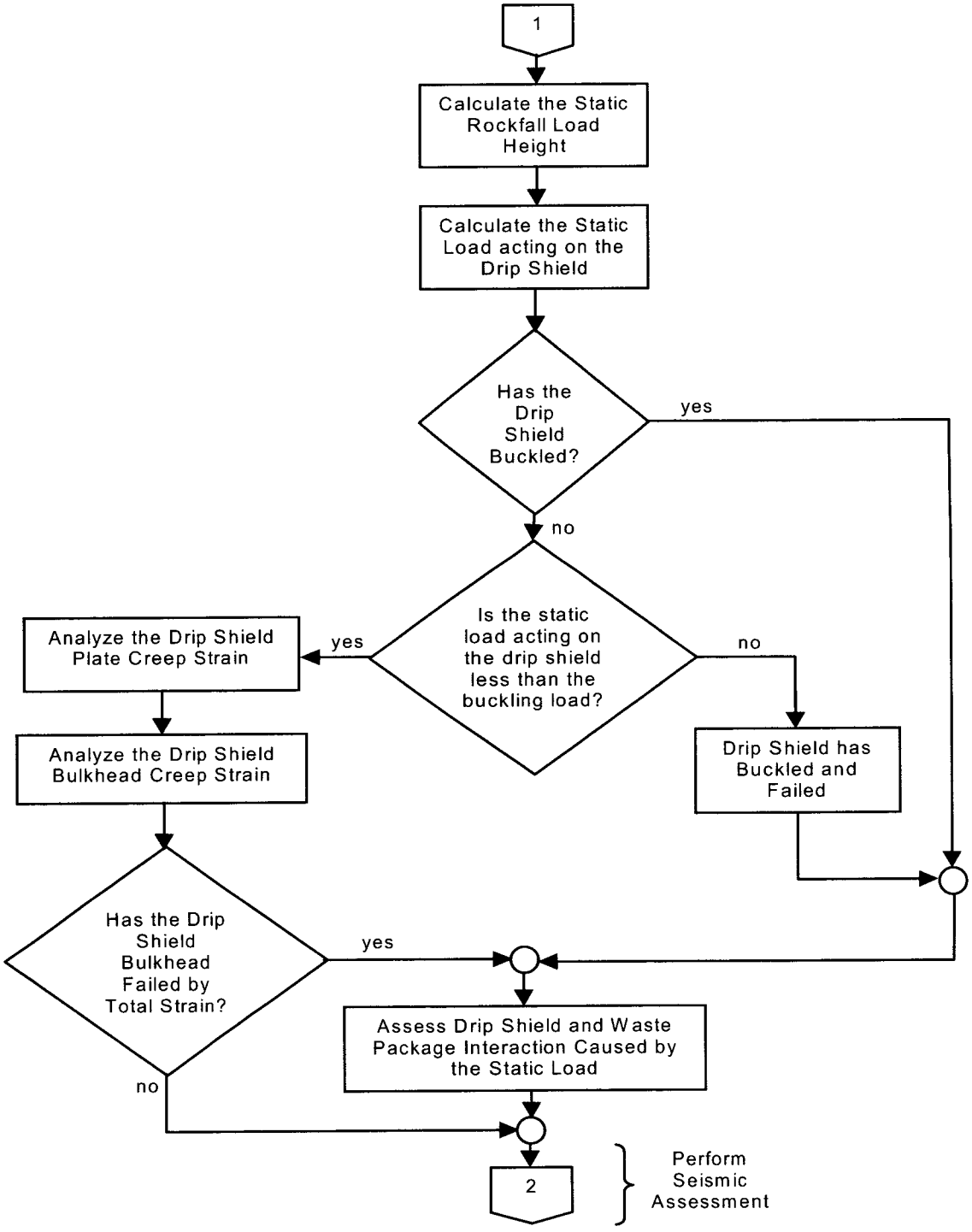

Figure 2-2. Flowchart of the PROCESSELEMENTS Subroutine (Continued)

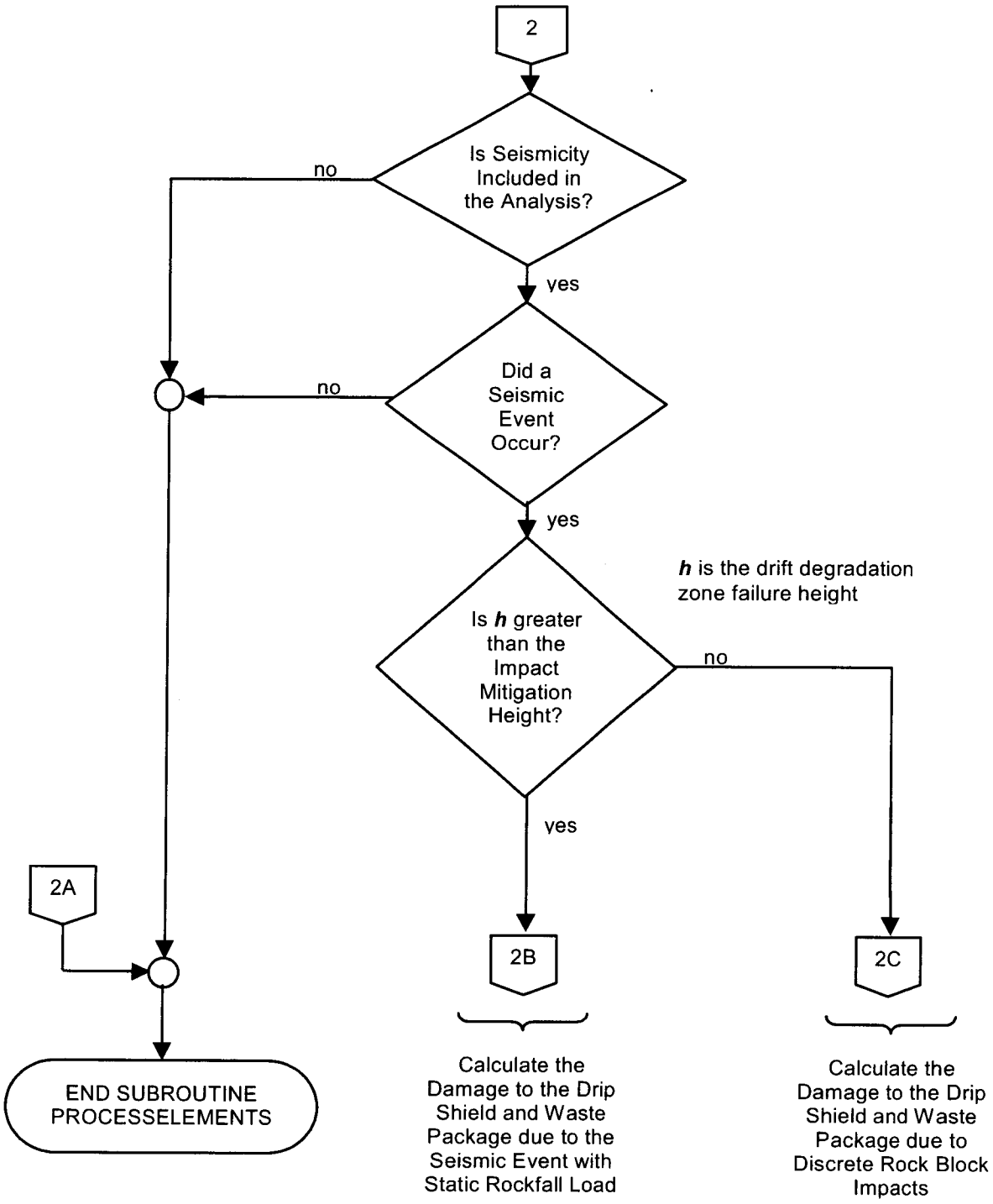

Figure 2-2. Flowchart of the PROCESSELEMENTS Subroutine (Continued)

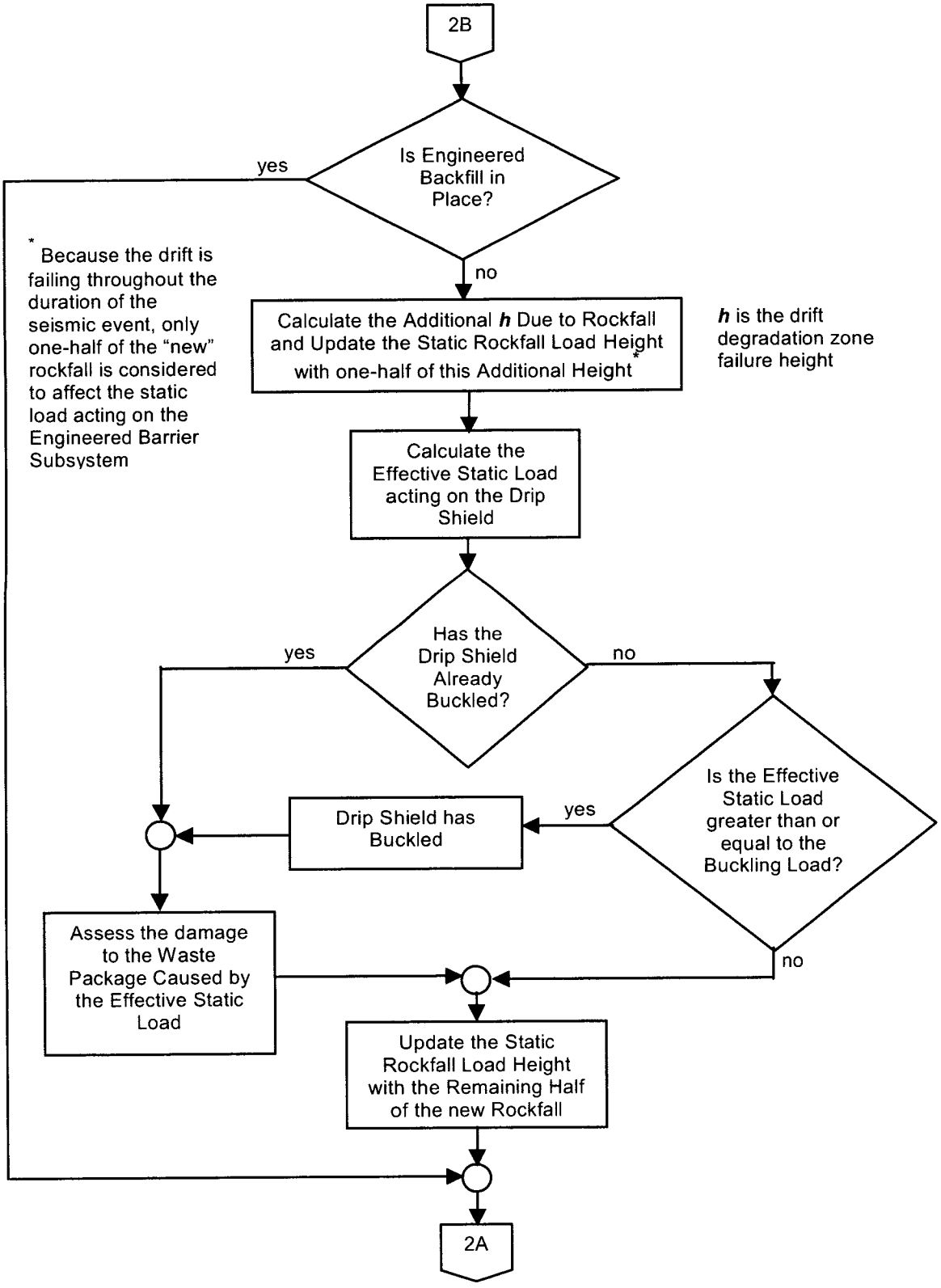

Figure 2-2. Flowchart of the PROCESSELEMENTS Subroutine (Continued)

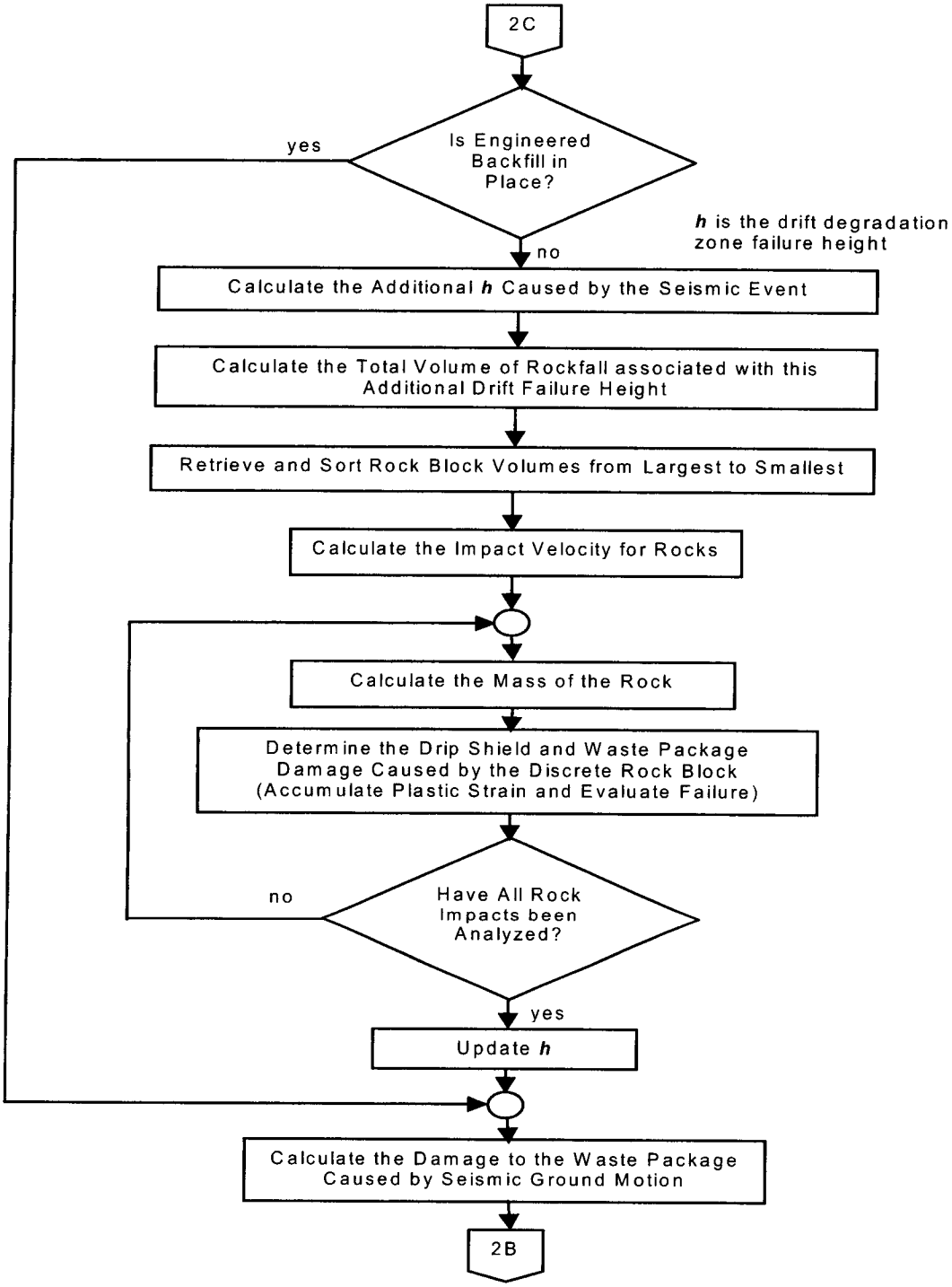

Figure 2-2. Flowchart of the PROCESSELEMENTS Subroutine (Continued)

3 SEISMIC HAZARD CURVE ABSTRACTION

Determination of the volume of rockfall requires the synthetic generation of the evolution of seismic events during the simulation period of interest, including the time of occurrence of a seismic event and the magnitude of the event. This chapter describes sampling the time and magnitude of occurrence of seismic events from a given hazard curve as implemented in the Total-system Performance Assessment code Version 5.0 beta.

3.1 Seismic Hazard Curve

A seismic hazard curve relates the magnitude and frequency of occurrence (or recurrence rate) of the events. The seismic hazard curve used in the U.S. Nuclear Regulatory Commission (NRC) approach to total-system performance assessment is represented in terms of a relationship between the recurrence interval and the magnitude of the mean peak horizontal ground acceleration (Figure 3-1). This curve represents the mean peak horizontal ground acceleration hazard curve provided by CRWMS M&O (1999d). This hazard curve is based on data from a probabilistic hazard analyses for fault displacement and vibratory ground motion at Yucca Mountain (DOE, 1995). The seismic hazard curve presented in Figure 3-1 applies to the free surface ground motions at the Yucca Mountain site. Recent information presented by the U.S. Department of Energy (DOE)[1] indicates that it will be using the Yucca Mountain free surface ground motions for the subsurface repository horizon design basis ground motions.

The sampled mean peak horizontal ground accelerations and the corresponding recurrence time intervals are provided as inputs to MECHFAIL. The continuous hazard curve in the Total-system Performance Assessment code is represented by 10 discrete intervals for the mean peak horizontal ground acceleration ranging between 0.05 to 6.0 g (see Table 3-1). The return periods for these ground motions are within the range of 142 to 100,000,000 years (i.e., a frequency of exceedance between 7.0643×10^{-3}/year and 1.0×10^{-8}/year).

3.2 Sampling of Event Time

The occurrence of seismic events is assumed to follow a Poisson process. When events occur according to a Poisson process, the time between occurrences (interarrival times) of the events has an exponential distribution. The mean recurrence time or return period for a simple Poisson process is $1/\upsilon$ where υ is the mean recurrence rate, that is the average number of occurrences of the event per unit time interval. In the basecase, the return period is 100 years, the fastest return period (i.e., the smallest recurrence interval). This return period means that on an average, once in 100 years a seismic event will occur (assuming that the Poisson process is a reasonable model for the occurrence of seismic events in the area). Event occurrence times and magnitude of the events are not correlated. In other words, large magnitude seismic events can occur at the same times as small magnitude events, but less frequently.

---

[1]DOE and NRC Public Meeting. Las Vegas, Nevada. August 6–8, 2002.

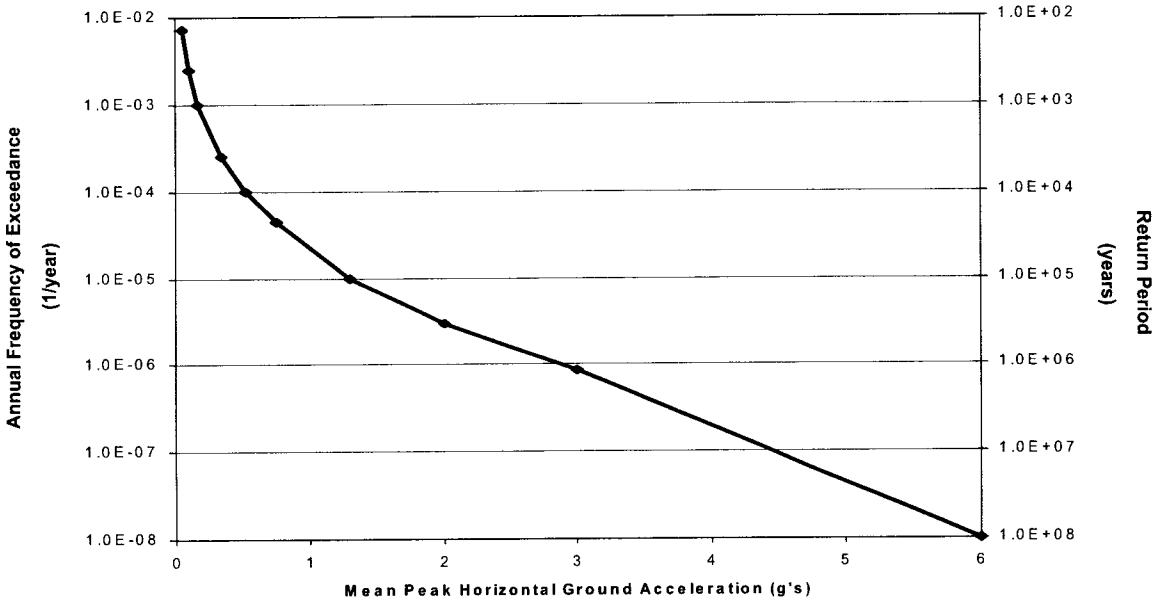

Figure 3-1. Seismic Hazard Curve Relating Annual Frequency of Exceedance and Return Period to Mean Peak Horizontal Ground Acceleration

Table 3-1. Seismic Hazard Curve Data Input to the Total-system Performance Assessment Code

Mean Peak Horizontal Ground Acceleration,* g's	Return Period,* years
0.050	142
0.100	409
0.169	1,000
0.350	3,968
0.534	10,000
0.750	22,340
1.305	100,000
2.000	336,261
3.00	1,158,062
6.00†	100,000,000†

*CRWMS M&O. "Seismic Ground Motion Hazard Inputs." WP–NEP–99309.T. MOL.19991005.0147. Las Vegas, Nevada: CRWMS M&O. 1999.
† DOE and NRC Public Meeting. Las Vegas, Nevada. August 6–8, 2002.

Figure 3-2 shows a histogram of sampled seismic event return periods in Total-system Performance Assessment code Version 5.0 beta. As expected, the histogram is converging to an exponentially decreasing frequency of exceedance (i.e., increasing return periods). A total of 53 seismic events were sampled during the 10,000-year regulatory time period and 557 events in a 100,000-year period. The position of the spikes in Figure 3-3 represent the times at which the sampled seismic events occurred in 100,000 years and the height of the spikes represent the sampled magnitudes of the individual events.

The assumptions inherent in this approach are the following:

- Any seismic event of a magnitude withing the allowable range can occur at any time
- The occurrence(s) of an event in a given time interval is independent of that in any other nonoverlapping time interval
- The probability of occurrence of an event in a small interval, Δt, is proportional to Δt, and is given by $\nu\Delta t$ (assumed to be constant); and the probability of two or more occurrences in Δt is negligible

3.3 Sampling of Seismic Event Magnitude

After the time of seismic events is established, then the event magnitude (in the case of the Total-system Performance Assessment code, expressed as the mean peak horizontal ground acceleration) is sampled according to the recurrence rate. First, the probability of occurrence of a given magnitude is computed. Then, corresponding to each seismic event time, a mean peak horizontal ground acceleration value is sampled according to its recurrence probability.

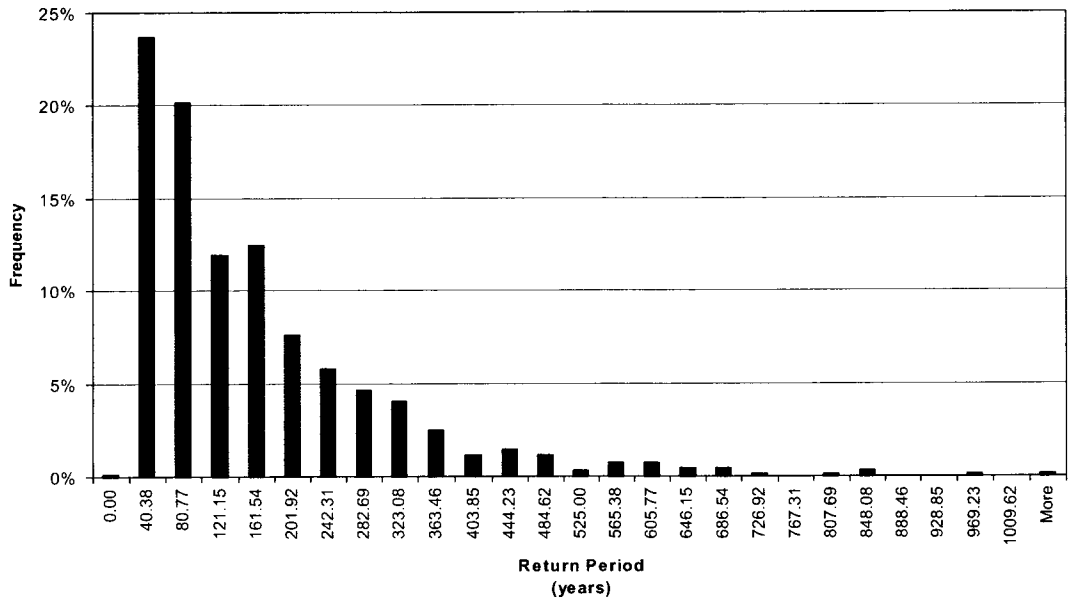

Figure 3-2. Histogram Showing Convergence to Exponentially Distributed Samples of Return Periods (Sampling Limited to 100,000 years)

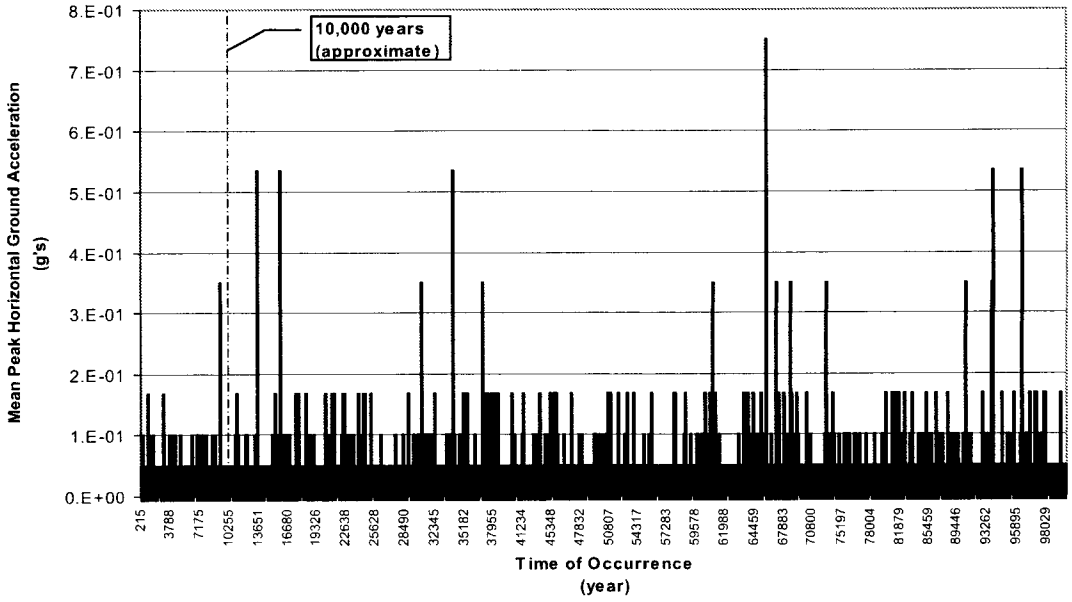

Figure 3-3. Sampled Values of Mean Peak Horizontal Ground Acceleration as a Function of Time (Each Vertical Bar Represents One Seismic Event)

4 APPROXIMATION OF ROCKFALL LOAD MAGNITUDES AND PROBABILITIES

The following discussion conveys the methodologies and assumptions used to establish bounding static and dynamic rockfall loads. Static rockfall loads are created by the accumulation of rockfall rubble over time as the structural integrity of the drifts degrade from the combined effects of thermal, mechanical, hydrological, and chemical processes. Dynamic rockfall loads occur when individual, discrete rock blocks become dislodged from the drift ceiling and free-fall under the influence of gravity to impact either the drip shield or waste package. At the present time, it is assumed that dynamic rockfall loads will occur only during seismic events (see Section 4.2.2).

The accumulation of rockfall caused by nonseismic thermal, mechanical, hydrological, or chemical processes will contribute to natural backfilling of the emplacement drifts. The nonseismic thermal-mechanical-hydrological processes include progressive fracture growth and slip of existing fractures and larger-scale discontinuities in response to the sustained gradients of temperature, fluid-pressure, and stress induced by the repository thermal loading. These degradation mechanisms will be aided by mechanical weakening of the rock from geochemical alteration processes such as reviewed in Ofoegbu (2000). The accumulated rockfall rubble from these processes and any seismically induced rockfall will impose sustained static loads on the engineered barrier subsystem.

For the current engineered barrier subsystem design, the waste package will be exposed to direct rockfall loads only during the preclosure operational period. After emplacement of the drip shields, the waste packages will be affected by rockfall only indirectly by way of potential interactions with the drip shield.

4.1 Characterization of Accumulated Rockfall Static Loads

The bounding static rockfall loads have been estimated using the fundamental conservation of mass principle. In addition, the relationship between the initial volume of the *in-situ* rock mass in the drift degradation zone, V_o, to its volume after falling from the drift ceiling, V_f, by way of a proportionality constant called the bulking factor, b_f [see (Eq. 4-1)], is used. The bulking factor accounts for the increase in volume of the rock mass after it has become fractured and broken into rubble.

$$b_f V_O = V_f \tag{4-1}$$

The bulking factors for the lower lithophysal and middle nonlithophysal rocks at the repository horizon have yet to be determined, so bulking factor values for common soils and rock types (see Table 4-1) were used to develop estimates. The lower lithophysal unit is highly fractured, has a relatively low rock mass strength, and tends to break into thin shards and plates, so the maximum value of bulking factor for the rock is expected to be similar to the bulking factor for shale (i.e., approximately equal to 1.5). The minimum value of bulking factor for the rock is expected to be small because of the effects of the lithophysal cavities on the bulking behavior.

Table 4-1. Bulking Factors for Common Soils and Rock Types	
Material	**Bulking Factor***
Clay (Low Plasticity Index)	1.30
Clay (High Plasticity Index)	1.40
Clay and Gravel	1.35
Sand	1.05
Sand and Gravel	1.15
Gravel	1.05
Chalk	1.50
Shales	1.50
Limestone	1.63
Sandstone (Porous)	1.60
Sandstone (Cemented)	1.61
Basalt	1.64
Granite	1.72
*http://www.dur.ac.uk/~des0www4/cal/roads/earthwk/earthwk.html	

The lithophysal cavities range in size from approximately 0.01–1.0 m [0.033–3.28 ft][1] and will tend to reduce the bulking factor if some of the broken-rock particles are smaller than some of the cavities. The minimum value of bulking factor for the lithophysal unit is set to 1.15 based on a consideration of the potential effects of the cavities on the bulking behavior (i.e., $1.15 < b_f < 1.5$ for the lower lithophysal rock). The middle nonlithophysal rock unit has a larger fracture spacing and rock-mass strength, and tends to break up into blocks, so the bulking factor is expected to be larger than for the lower lithophysal rock. The middle nonlithophysal rock is assigned values of bulking factor in the range of 1.35–1.5. Uniform distributions are used to define the variability of the bulking factor within the specified ranges for the two rock types. As demonstrated in Section 4.1.1, the magnitude of the bounding static rockfall load varies significantly for bulking factors within the range of 1.1 to 1.5. Smaller bulking factors result in higher static rockfall loads.

[1]Sweetkind, D.S., S.C. Beason, and D.C. Buesch. Overview of the Stratigraphy and Structural Setting of Yucca Mountain, Nevada, USA. *Paper submitted to International Journal of Rock Mechanics and Mining Sciences and Geomechanics Abstracts.* August 2002 (in press).

19/72

4.1.1 Accumulated Rockfall Static Load Distribution

The magnitude of the bounding static rockfall loads is controlled by the mass of rockfall rubble that accumulates on top of the drip shield. The upper-bound amount of rockfall rubble supported by the drip shield can be determined by calculating the volume of rock needed to fill the combined volume of the initial drift void space and the new void space created by rockfall and accounting for the bulking factor [see (Eq. 4-2)]. Note the similarities between Eqs. (4-1) and (4-2).

$$b_f V_o = (V_o + V_d) \tag{4-2}$$

where

b_f — bulking factor
V_o — drift degradation zone volume
V_d — drift void volume
V_f = $V_o + V_d$

Assuming this behavior occurs uniformly over the entire length of a drift, the loads can be derived on a per unit length basis. Moreover, the mathematical relationships can be written on a cross-sectional area basis as opposed to a volumetric one [see (Eq. 4-3)]. A graphical representation of Eq. (4-3) is provided in Figure 4-1.

$$b_f A_o = (A_o + A_d) \tag{4-3}$$

where

A_o — cross-sectional area of the drift degradation zone
A_d — drift void cross-sectional area
A_f = $A_o + A_d$

Because the drift void cross section can be readily calculated from available information (CRWMS M&O, 2000a), the key to the problem is establishing a reasonable approximation of the geometry for the cross-sectional area of the drift degradation zone. Three different geometries for A_o were investigated to determine the relative effects of this choice on the bounding static rockfall load. These assumed areas will be referred to as the trapezoidal (see Figure 4-2a), triangular (see Figure 4-2b), and elliptical (see Figure 4-2c) drift degradation geometries. It is important to observe that the triangular and elliptical cross-sectional areas have a single unique solution for A_o for a given bulking factor. A unique solution for A_o also establishes a unique solution for the bounding static rockfall load (i.e., for a given bulking factor). The trapezoidal drift degradation geometry, on the other hand, requires an additional parameter, θ, which is defined in Figure 4-2a, to determine the magnitude of the static rockfall load acting on the drip shield.

After A_o has been determined, the resulting load acting on the drip shield can be approximated by assuming the rockfall rubble exerts a continuous distribution of pressure over the surface of

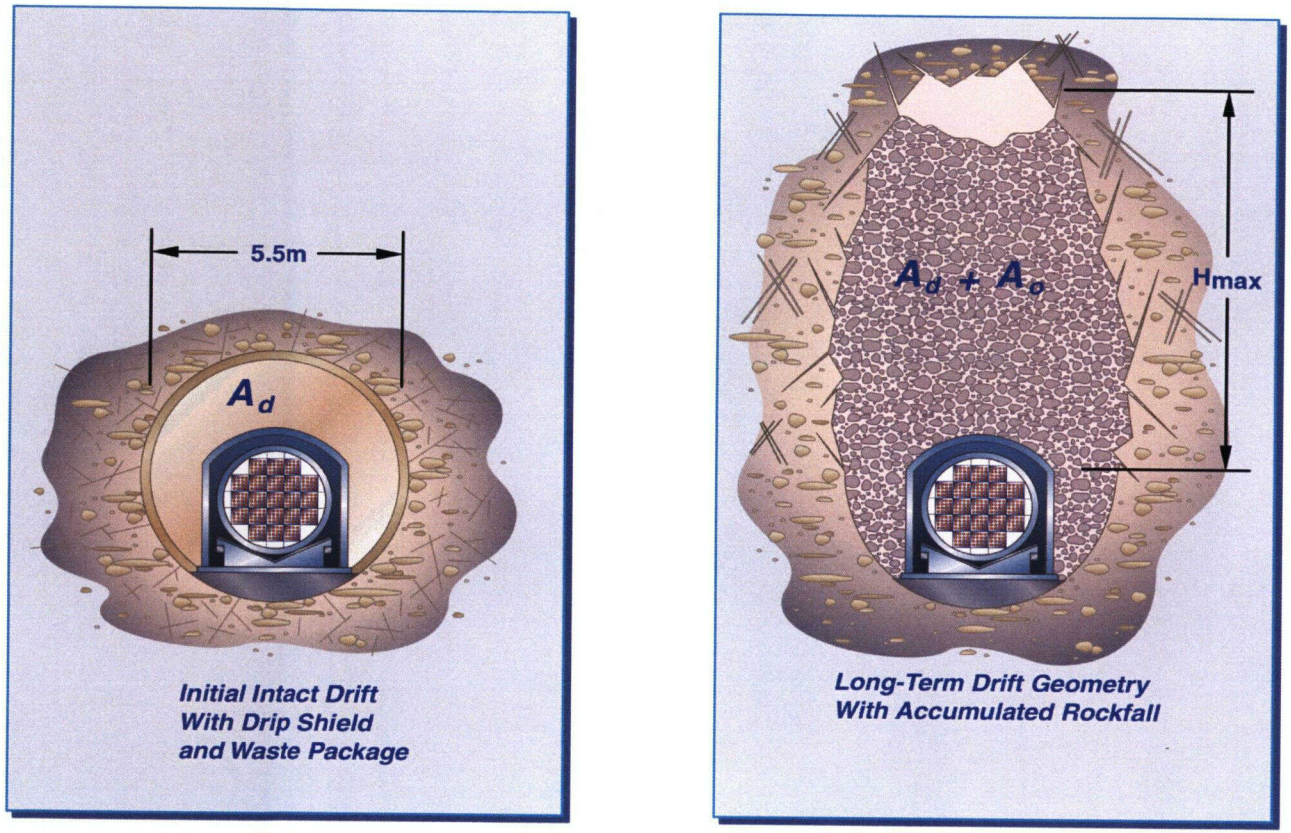

Figure 4-1. Illustration of the Drift Void and Drift Degradation Zone Area Parameters

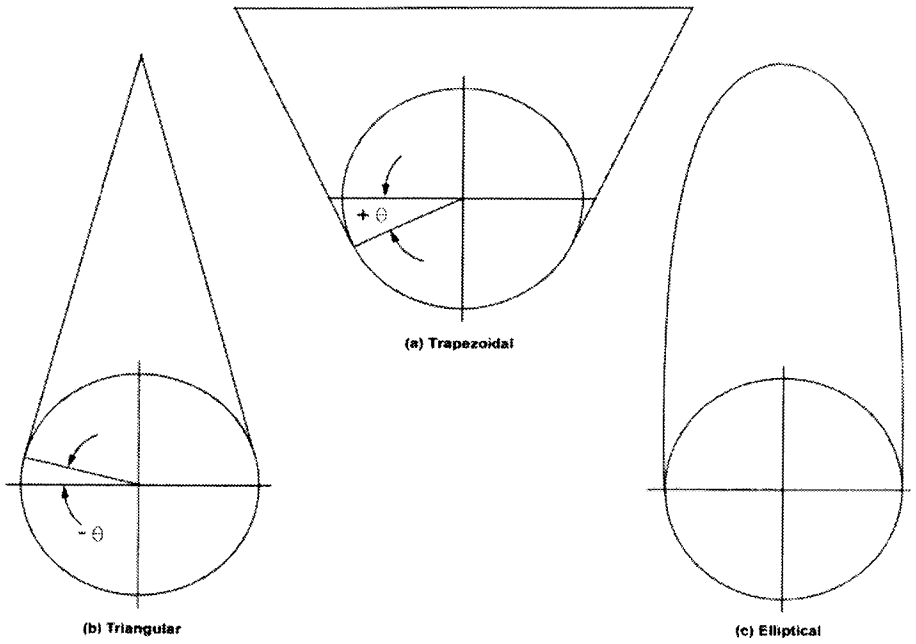

Figure 4-2. Potential Drift Degradation Geometries

the drip shield crown. The distribution of the pressure acting on the drip shield is approximated by Eq. (4-4). Figure 4-3 illustrates the variables used in Eq. (4-4).

$$\rho_{eff} = \rho_o \frac{V_o}{V_f} \tag{4-6}$$

where

x	—	variable defining the transverse distance from the drip shield crown center
$P(x)$	—	rock rubble pressure at x from the drip shield crown
ρ_{eff}	—	effective density of the rock rubble
g	—	gravitational acceleration
$h(x)$	—	rock rubble height at x from the drip shield crown

The effective density of the rock rubble, ρ_{eff}, required in Eq. (4-4) is determined using the conservation of mass principle. Specifically,

Solving Eq. (4-5) for ρ_{eff} gives

$$P(x) \cong \rho_{eff} g h(x) \tag{4-4}$$

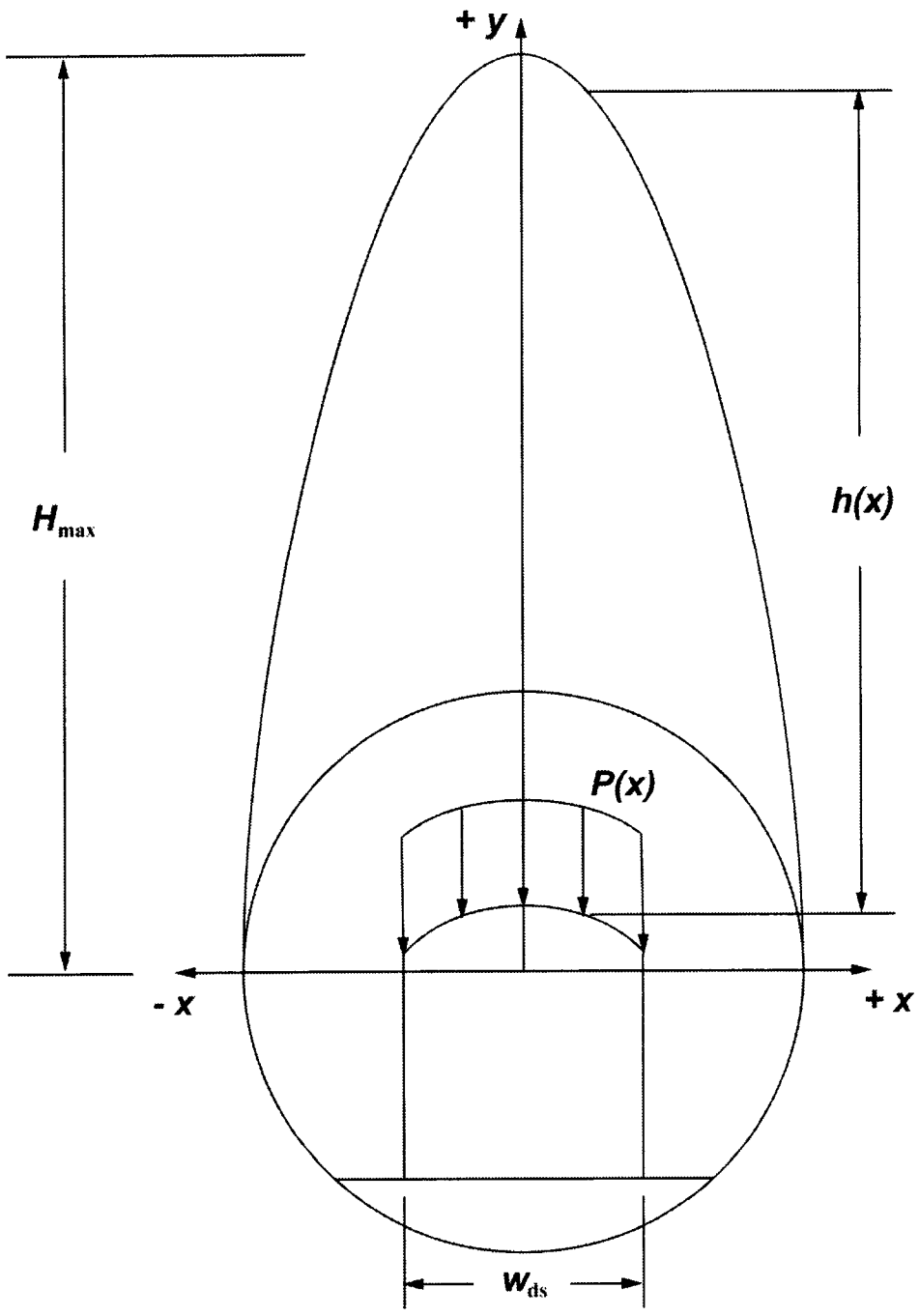

Figure 4-3. Parameters Used to Approximate Drip Shield Crown Pressure Loads

Using Eq. (4-1), Eq. (4-6) can be recast as

$$\rho_{\text{eff}} = \frac{\rho_o}{b_f} \tag{4-7}$$

The resultant static rockfall load acting on the drip shield crown, per unit length, is obtained by integrating Eq. (4-4) over the width of the drip shield [see (Eq. 4-8)].

$$\begin{aligned} \frac{F}{L} &= \int_{-\frac{w_{ds}}{2}}^{+\frac{w_{ds}}{2}} P(x)\,dx \\ &= 2\int_0^{+\frac{w_{ds}}{2}} P(x)\,dx \\ &= 2\frac{\rho_o g}{b_f}\int_0^{+\frac{w_{ds}}{2}} h(x)\,dx \end{aligned} \tag{4-8}$$

where

w_{ds} — drip shield width

Figure 4-4 plots the resultant static rockfall load acting on the drip shield for the trapezoidal and triangular drift degradation geometries for varying values of the bulking factor. As pointed out earlier, the trapezoidal drift degradation geometry requires an additional parameter, θ, to determine the magnitude of the static rockfall load acting on the drip shield. Therefore, the effects of θ on the resultant static rockfall load acting on the drip shield for variations of the trapezoidal drift degradation geometry are represented by the positive values of this parameter in Figure 4-4. The unique bounding static rockfall loads for the triangular drift degradation geometry for varying values of the bulking factor are also plotted in Figure 4-4. The unique solution for the bounding static rockfall load using the triangular drift degradation geometry is plotted in terms of its unique negative value of θ.

Figure 4-5 is a plot of the bounding static rockfall loads for the elliptical drift degradation geometry and varying values of the bulking factor. Figure 4-6 is a plot of the corresponding maximum elliptical drift degradation zone failure height as a function of the bulking factor.

As can be seen from Figures 4-4 and 4-5, the bounding static rockfall loads for the trapezoidal drift degradation geometry are significantly smaller than those for the triangular and elliptical versions. Experience with mining-induced caving (e.g., Brady and Brown, 1985) indicates that the elliptical geometry is more likely than either the trapezoidal or triangular geometries if the host rock is homogeneous and rockfall is controlled by mechanical processes. The elliptical drift-degradation geometry, which is often described as chimney caving in mining engineering, is associated with two types of homogeneous rock conditions: (i) soils or weak rocks, such as sand, clay, or weak shale, sandstone, chalk, or similar materials; and (ii) a regularly jointed rock mass, in which rockfall is controlled by the unraveling of the discontinuities. In such rock-mass conditions, rockfall in an unsupported opening may lead to the formation of a chimney-shaped degradation zone. The height of such a degradation zone is controlled by the bulking characteristics of the rock. The lower lithophysal rock is similar to a weakly cemented sandstone, based on observations of rockfall characteristics in a recently completed exploratory

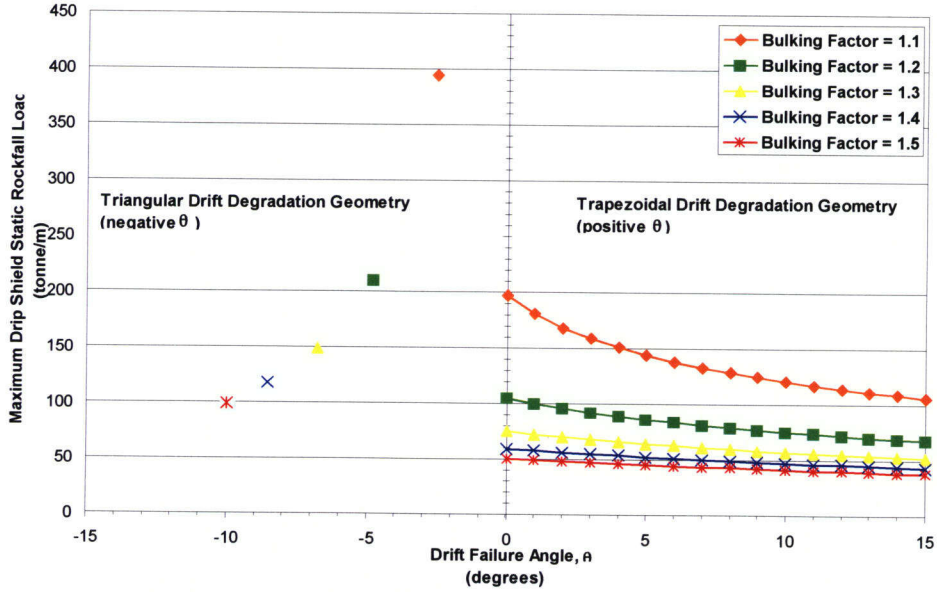

Figure 4-4. Maximum Static Rockfall Load Acting on the Drip Shield Crown for the Trapezoidal (+ θ) and Triangular (- θ) Drift Degradation Geometries for Different Bulking Factors

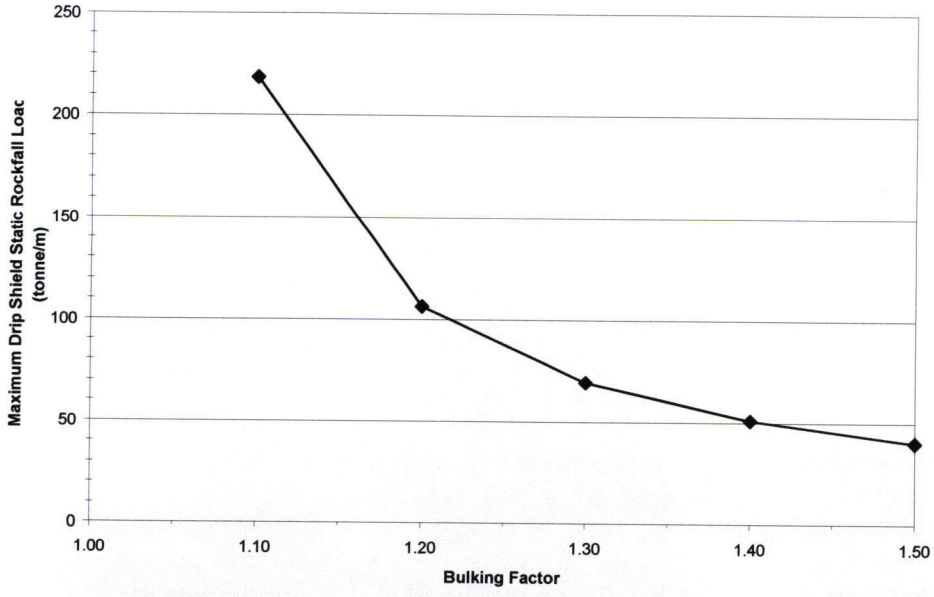

Figure 4-5. Maximum Drip Shield Static Rockfall Load as a Function of the Bulking Factor for the Elliptical Drift Degradation Geometry

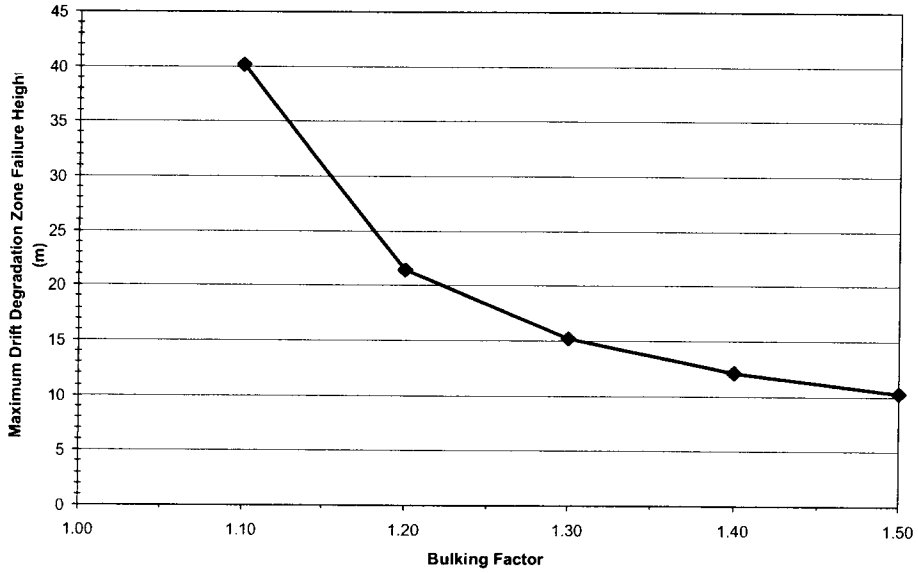

Figure 4-6. Maximum Drift Degradation Zone Failure Height as a Function of the Bulking Factor for the Elliptical Drift Degradation Geometry

drift at Yucca Mountain and on information provided by the U.S. Department of Energy (DOE) staff. Also, the middle nonlithophysal unit is known to be regularly jointed, having three regularsets and one random set of joints (CRWMS M&O, 2000b). These two rock units, therefore, belong to the class of rock masses for which caving is likely to follow the elliptical geometry.

The long-term configuration of an emplacement drift and the associated static rockfall load have been determined using a mass-balance analysis, in which the height of the drift-degradation zone is controlled by the bulking behavior of the rock. The mass-balance approach does not consider the forces and material resistance that control rockfall but is based on the principle that rockfall would occur if, and only if, the available space can accommodate the rubble formed from the rockfall. An alternative approach based on a limit-equilibrium analysis is now presented to further explore the potential variability of the drift degradation zone failure height.

The limit-equilibrium analysis is based on a procedure widely used to evaluate the potential for chimney caving above underground mines (Brady and Brown, 1985). Consider, for example, the static equilibrium of a rectangular block of rock above an emplacement drift. The base of the block is at the same elevation as the drift spring line. The width of the block is the same as the drift diameter, D. The length, L, of the block (along the drift axis) is arbitrary; however, L is set equal to D for the analysis. The block extends to the ground surface, but a section of the block up to a height, h, above the drift roof may fall as determined by the static equilibrium conditions. Therefore, h represents the height of the degradation zone. The equilibrium of the potentially unstable block is controlled by the weight, the overburden pressure on the top surface, and the shear resistance on the four vertical boundary surfaces of the block.

It can be shown by summing these forces to zero, representing the limit-equilibrium condition, that the height of the degradation zone is given by the equation

$$h = z + \frac{c}{\mu K \gamma} - \left[\left(z + \frac{c}{\mu K \gamma} \right)^2 - \frac{Dz}{2\mu K} \right]^{1/2} \qquad (4\text{-}9)$$

where γ, μ, and c are the average unit weight, friction coefficient, and cohesion parameter for the rock mass; z is the depth of the drift axis below the ground surface; and K is the horizontal-to-vertical stress ratio. The following parameter values were used for the analysis: D = 5.5 m [18.0 ft], z = 300 m [984 ft], γ = 0.025 MN/m^3 [159 lb/ft^3], and μ = 0.8 (which is equivalent to a friction angle of approximately 40 degrees). The results calculated using Eq. (4-9) are shown in Figure 4-7, which illustrates the variation of the potential drift degradation zone failure height as c and K are varied.

The decrease in K to near-zero values represents a change that would occur during a seismic event. Such changes in K, therefore, help explore how an equilibrium configuration calculated for static conditions may change during a seismic event. The range of c values used in the analysis was chosen to explore the behavior of the fractured rock mass when subjected to the near-zero confining pressures implied by the low K values. A fractured rock mass has no significant intrinsic cohesion. The strength-envelope for such a rock, however, is curved such that a straight-line fit to the strength envelope for relatively high confining-stress conditions would give a significant nonzero value for the c parameter. Such c values, however, are not appropriate for analyzing the behavior of the rock when subjected to low confining stress conditions, such as may occur during a seismic event as represented by the low K values in Figure 4-7. The behavior obtained using a rock-mass cohesion of 0.1 MPa [14.5 psi], therefore, represents the expected behavior of a fractured rock mass better than the relationships obtained using the higher cohesion values.

As Figure 4-7 shows, the drift degradation zone failure height obtained for static (i.e., K = 0.2) conditions using the limit-equilibrium analysis is smaller than the drift degradation zone failure height obtained from the mass-balance calculation. The limit-equilibrium analysis, however, gives an increasing drift degradation zone failure height as K decreases (using a small value of c appropriate for low K conditions) and predicts an ultimate equilibrium configuration with a degradation zone that is more extensive than the degradation zone calculated based on the mass-balance approach. The mass-balance approach indicates that the degradation zone would extend to a maximum height of 40 m [131.2 ft] for the smallest value of bulking factor used in this report, whereas the limit-equilibrium analysis predicts a maximum height of approximately 100 m [328 ft]. The limit-equilibrium approach may overestimate the drift degradation zone failure height because the self-equilibration mechanism provided by the bulking behavior of the rock is not accounted for in the analysis. This analysis indicates that the height obtained through the mass-balance approach is a reliable upper-bound estimate of the potential drift degradation zone failure height, dependent only on the value of bulking factor used for the analysis.

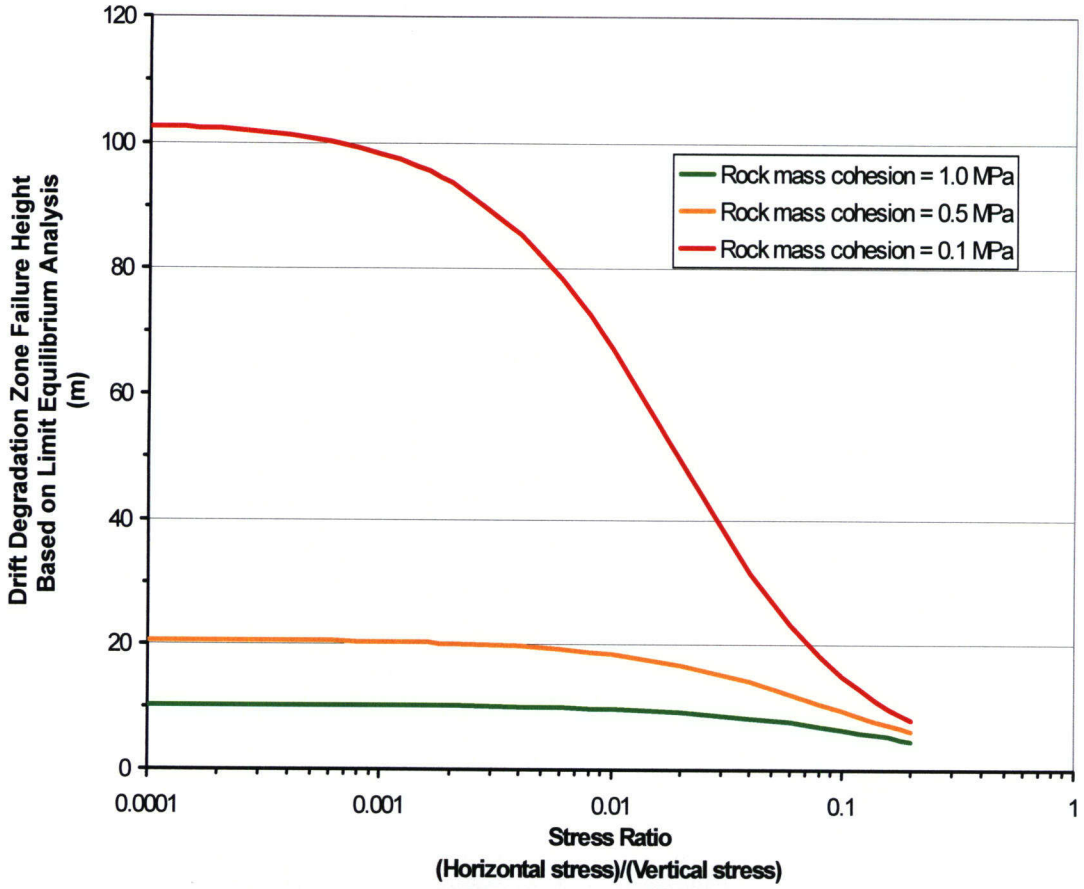

Figure 4-7. Variations of the Height of a Potential Drift Degradation Zone Based on a Limit-Equilibrium Analysis of Chimney Caving Above an Emplacement Drift

4.1.2 Accumulated Rockfall Static Load Abstraction

The following discussion describes the rationale and methodology used to account for drift degradation caused by thermal, mechanical, hydrological, and chemical processes in the Total-system Performance Assessment code.

As described in Chapter 2, the repository footprint is represented by 20 spatial grid elements, with two grid elements assigned to each of the 10 subareas used within the Total-system Performance Assessment code. One of the grid elements represents the percentage of the given subarea that is in the lower lithophysal rock unit and the other grid element represents the remaining percentage of the middle nonlithophysal rock unit. Each grid element is assigned a bulking factor from the range of possible bulking factors for that particular rock unit. A uniform distribution of the bulking factor is used for this purpose. After a bulking factor has been assigned to a given grid element, the maximum drift degradation zone failure height can, in turn, be calculated.

The rate at which the drifts will degrade from thermal, mechanical, hydrological, and chemical processes is difficult, if not impossible, to establish with any degree of accuracy or precision. The rate of drift degradation is dependent on the rates of several processes such as fracture growth, slip on existing fractures, and geochemical wall-rock alteration. These factors, in turn, are controlled by the time-dependent gradients of temperature, fluid pressure, rock stress, and chemical composition of the interacting fluids and mineral solids (e.g., see literature review in Mantuefel, et al., 1993; Ofoegbu, 1999, 2001). The lack of information on predicting the long-term degradation rate of underground openings (despite the long history of mining, transportation, and several other applications of underground excavations) is partly because of the complexity of modeling these coupled processes, but mainly because the engineering of underground space has hitherto focused on building stable openings. The characterization of the potential instability of underground openings is typically not undertaken. Available records on abandoned underground excavations, such as the several tunnels constructed at the Nevada Test Site as part of the weapons program (e.g., U.S. Geological Survey, 1982; Zimmerman, et al., 1990; Wong, et al., 1991), will be examined to evaluate the abstraction of the drift degradation rates.

As an interim approach, an abstraction of the long-term configurations of the emplacement drifts and the accumulated rockfall static loads has been developed based on the bulking behavior of rocks. To develop an abstraction of the drift degradation rate (i.e., the rate of change of the drift geometry from the initial to long-term configurations as illustrated in Figure 4-1), it is necessary to consider (i) the anticipated stand-up time for an unsupported opening in fractured rock typically varies from a few hours in poor-quality rocks to a few months in good-quality rocks (cf., Hoek and Brown, 1980), and (ii) the ground support system for the emplacement drifts will be monitored and maintained through the preclosure period but will be abandoned thereafter.

The stand-up time for an unsupported opening is the time period from the initial excavation to the onset of drift instability, which is manifested by new fracture generation, existing fracture propagation, and rockfall. As can be seen in Figure 4-8, the allowable unsupported span of an underground opening can be estimated using the rock mass quality index. This information is further augmented by the estimated ranges of stand-up time for different rock mass quality indices and unsupported span lengths (see Figure 4-9). The rock mass quality classification for the repository host rock is expected to lie in the range of fair rock through good rock. The expected stand-up time for unsupported openings in such rocks is on the order of days and months.

Based on this information, it is reasonable to expect that the drifts will begin to backfill themselves in a relatively short period of time after cessation of ground support maintenance activities. It is also reasonable to expect the ground support system to remain effective for a short time (maybe on the order of tens of years) following the cessation of maintenance. Therefore, a beta distribution based on the staff's best engineering judgment has been developed for assigning the time required for the drifts to backfill themselves completely to the maximum drift degradation zone failure height (see Figure 4-10). Each spatial grid element is assigned a unique self-backfilling time, ranging from a minimum of 250 years to a maximum of 1,000 years. An improvement of the abstraction can be expected based on a review of the available records on abandoned underground openings, but the maximum self-backfilling time is not expected to exceed 1,000 years.

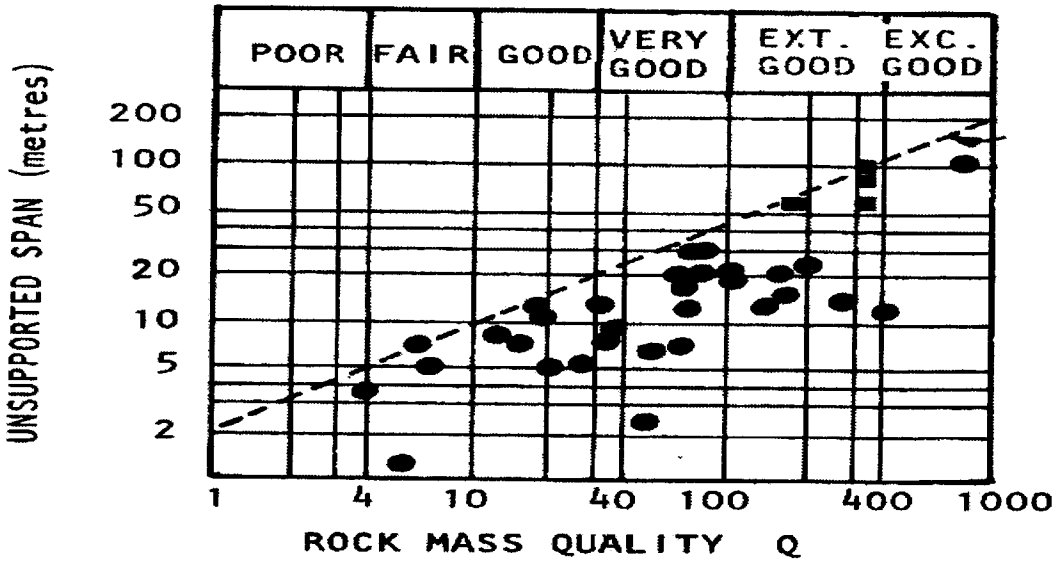

Figure 4-8. Allowable Unsupported Span as a Function of Rock Mass Quality (Hoek, and Brown, 1980)

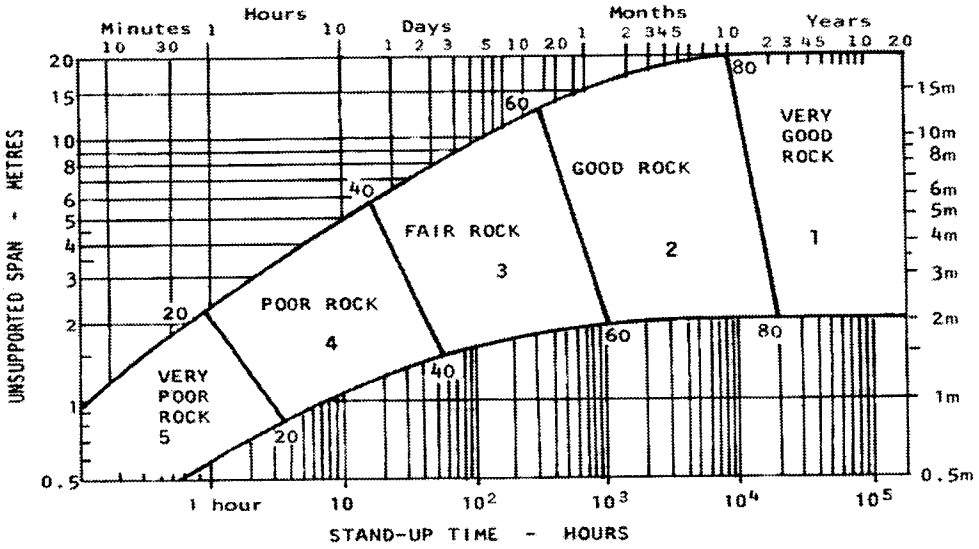

Figure 4-9. Estimated Ranges of Drift Standup Time for Different Rock Mass Quality Indices and Unsupported Span Lengths (Bieniawski, 1974)

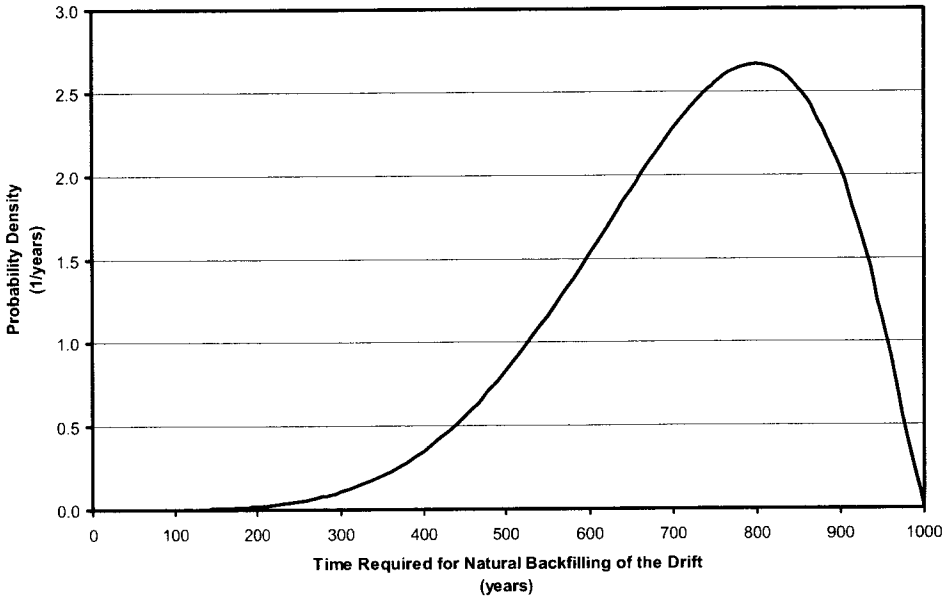

Figure 4-10. Beta Distribution Defining the Time Required for the Drifts to Backfill Themselves Completely

Given that the maximum drift degradation zone failure height and the time required to achieve this level of degradation has been defined for each spatial grid element, the rate of drift degradation can be calculated on a per-grid element basis. The rate of drift degradation within the MECHFAIL module is characterized by the rate of change of the major elliptical axis (i.e., drift degradation height) of the assumed elliptical drift degradation zone geometry with respect to time.

$$\frac{dh(x=0)}{dt} = \frac{H_{max}}{t_d} \tag{4-10}$$

where

dh/dt — drift degradation zone failure height rate (m/years)
H_{max} — maximum drift degradation zone failure height (m)
t_d — natural backfilling time (years)

The static rockfall load acting on the drip shield is calculated using both the drift degradation zone failure height rate and the volume of rockfall attributable to individual seismic events (see Section 4.2). The accumulated rockfall volume resulting from drift degradation is calculated on an incremental time basis. At the end of each time increment, the drift degradation height is updated using the following relationship

$$h_{i+1} = h_i + \frac{dh(x=0)}{dt}\Delta t_i \tag{4-11}$$

The additional volume of rockfall and its contribution to the static load can be readily calculated using basic elliptical geometry relationships, the updated drift degradation height defined in Eq. (4-11), and Eq. (4-8). The additional volume of rockfall attributable to a seismic event at the end of a time increment is added to the accumulated rockfall volume as well (see Section 4.2.3 for more details).

4.2 Characterization of Discrete Rock Block Impact Loads

Rockfall may be seismically induced or, as described in Section 4.1, caused by long-term degradation of a rock mass. In a fractured rock mass, the falling rocks may be blocks bounded by existing fractures or new rock blocks developed because of long-term degradation of existing blocks. The objective of this section is to describe the rationale, methodology, and basis for estimating the size distributions of the existing rock blocks in the Topopah Springs Welded Tuff Middle Nonlithophysal and Lower Lithophysal rock units and how this information is used to establish bounding rock block impact loads on the engineered barrier subsystem.

4.2.1 Discrete Rock Block Size Distribution

4.2.1.1 Joint Data Input

The fracture orientation, spacing, and length used in developing size distribution of existing rock blocks for the Topopah Spring Welded Tuff Middle Nonlithophysal and Lower Lithophysal units are given in Tables 4-2 and 4-3. The data presented in both tables were documented in a fracture geometry analysis report prepared by CRWMS M&O (2000c) and developed using the Exploratory Studies Facility fracture mapping data. These data include only the fractures with measured trace length larger than 1 m [3.28 ft].

The fracture bridge length and the gap between the edges of two adjacent coplanar fracture surfaces were assumed in this analysis because no data for these parameters are currently available. Fracture bridge length is normally a small value relative to the fracture trace length. It the fracture bridge length was assumed to be equal to zero, then a fracture could become persistent if variation in fracture spacing was not considered. Fracture bridge length somewhat controls the formation of blocks. Smaller values for bridge length improve the chance of a block forming.

4.2.1.2 Generation of Fracture Surfaces in Space

To generate fracture patterns in a three-dimensional space, a preprocessor for the Three-Dimensional Discontinuous Deformation Analysis computer code was used. A Monte Carlo technique was used so that variations associated with the fracture information could be considered. Note that each pattern generated is an equally likely realization of fractures that honors the information in Tables 4-2 and 4-3. In developing these realizations, the fracture spacing, length, and bridge length were assumed to be uniformly distributed and varied ±30 percent about the mean values of the respective parameters.

For each realization, a model of 20 × 20 × 20 m [65.6 × 65.6 × 65.6 ft] in dimension was used to generate fracture patterns for the Topopah Spring Welded Tuff Middle Nonlithophysal unit in a three-dimensional space while the model dimension was 40 × 40 × 40 m [131.2 × 131.2 ×

Table 4-2. Fracture Information for Topopah Spring Welded Tuff Middle Nonlithophysal Rock Unit					
Fracture Set Number	**Dip Angle, Degrees**	**Dip Direction, Degrees**	**Mean Trace Length, m [ft]**	**Mean Bridge Length, m [ft]**	**Mean Spacing, m [ft]**
1	84	221	2.54 [8.33]	0.1 [0.33]	0.60 [1.97]
2	83	299	2.71 [8.88]	0.1 [0.33]	1.92 [6.30]
3	9	59	3.23 [10.59]	0.1 [0.33]	0.56 [1.84]

Table 4-3. Fracture Information for Topopah Spring Welded Tuff Lower Lithophysal Rock Unit					
Fracture Set Number	**Dip Angle, Degrees**	**Dip Direction, Degrees**	**Mean Trace Length, m [ft]**	**Mean Bridge Length, m [ft]**	**Mean Spacing, m [ft]**
1	82	235	4.56 [14.96]	0.1 [0.33]	3.47 [11.38]
2	79	270	4.02 [13.19]	0.1 [0.33]	4.05 [13.28]
3	5	45	7.36 [24.14]	0.1 [0.33]	2.94 [9.64]

131.2 ft] for the Topopah Spring Welded Tuff Lower Lithophysal unit. The larger dimension was used for the latter because the associated fracture spacings were relatively larger than those for the Topopah Spring Welded Tuff Middle Nonlithophysal unit. The larger dimension was used to minimize the potential model-boundary effect.

The fracture geometry analysis report prepared by CRWMS M&O (2000c) shows that the fracture spacings and trace lengths for the four litho-stratigraphic subunits of the Topopah Spring Welded Tuff are mostly lognormally distributed and some are exponentially distributed. Consequently, depending on the lower and upper limits used to constrain sampling, the assumption of a uniform distribution in this analysis could potentially underestimate the maximum block size but overestimate the number of relatively large blocks available. No attempt was made to address the potential effects of the uniform distribution assumption used in this study. Variations in fracture dip angle and dip direction were not incorporated in the analyses presented in this report to avoid producing blocks with overly complicated geometries.

In this study, a fracture plane in the three-dimensional space was treated as a planar surface. Potential curved conditions were not considered because of complexity and lack of information. There are considerable uncertainties on what the representative shapes for fracture planes should be. The shape of a fracture plane may depend largely on the mechanism through which the fracture is formed. In this study, a fracture surface was assumed to be a square in shape with its length equal to the length of the corresponding fracture. The potential shape effects on rock block size distribution were not evaluated.

The fracture trace lengths listed in Tables 4-2 and 4-3 are mapped field data, which form a lower bound on actual dimensions of the fracture planes. To avoid under-representation of actual dimensions of fracture planes, three length dimensions representing a square fracture geometry were used in this study to assess the distribution of block sizes. These length dimensions were equal to two, three, and four times the corresponding fracture trace lengths.

4.2.1.3 Probability of Occurrence of Block Size

After a fracture pattern was fully developed for a realization, it was used to identify individual rock blocks. A rock block is defined as a rock fragment or piece that is isolated completely from the rest of the rock medium by the surrounding fracture surfaces. Five realizations for each fracture length dimension were performed. No attempt was made to determine the potential effect of number of realizations on block number and size distribution.

Figure 4-11 shows the percent distribution of rock block sizes developed using the three fracture plane dimensions for the Topopah Spring Welded Tuff Middle Nonlithophysal unit. The curves presented in Figure 4-11 were calculated based on isolated rock blocks identified for five realizations. Each data point shown in the figure represents a volume range. The largest volume in each volume range was used in the figure for convenience. For the cases where the fracture dimension was twice the corresponding trace length, the total volume of the isolated rock blocks formed ranged from 10 to 14 percent of the volume of the model, which was 20 × 20 × 20 m [65.6 × 65.6 × 65.6 ft] in dimension, for the five realizations performed. The range was from 43 to 54 percent for the cases where the fracture dimension was three times the corresponding trace length and varied from 62 to 64 percent for the cases where the fracture dimension was four times the corresponding trace length.

Understandably, it is less likely that smaller fracture planes intersect and consequently form isolated blocks. Even though the number of blocks formed using the three fracture plane dimensions were different, the size distributions for the blocks identified appeared to be similar, as demonstrated in Figure 4-11. Figure 4-12 presents the data shown in Figure 4-11 in a cumulative fashion. A majority of the blocks (more than 95 percent) were smaller than 4 m^3 [141 ft^3] with only a very small percentage of the rock blocks greater than 8 m^3 [282 ft^3].

No more than one isolated block was formed for each realization performed for the Topopah Spring Welded Tuff Lower Lithophysal unit when the fracture plane dimension used was either two or three times the mapped fracture trace length. Although some isolated rock blocks were identified for the five realizations where four times the corresponding trace length was used as the fracture dimension, the number of blocks for each realization ranged only from 6 to 16. The volume of these isolated rock blocks varied from 43 m^3 [1,520 ft^3] to 160 m^3 [5,650 ft^3], which was considerably larger than those for the Topopah Spring Welded Tuff Middle Nonlithophysal unit. The average total volume of the isolated rock blocks for the five realizations amounted to less than 0.2 percent of the total model volume. Recall that the model used for the Topopah Spring Welded Tuff Lower Lithophysal unit was 40 × 40 × 40 m [131.2 × 131.2 × 131.2 ft] in size. This finding suggests that the Topopah Spring Welded Tuff Lower Lithophysal unit can be considered a continuous medium if the representative fracture plane dimension is less than or equal to four times the mapped trace length.

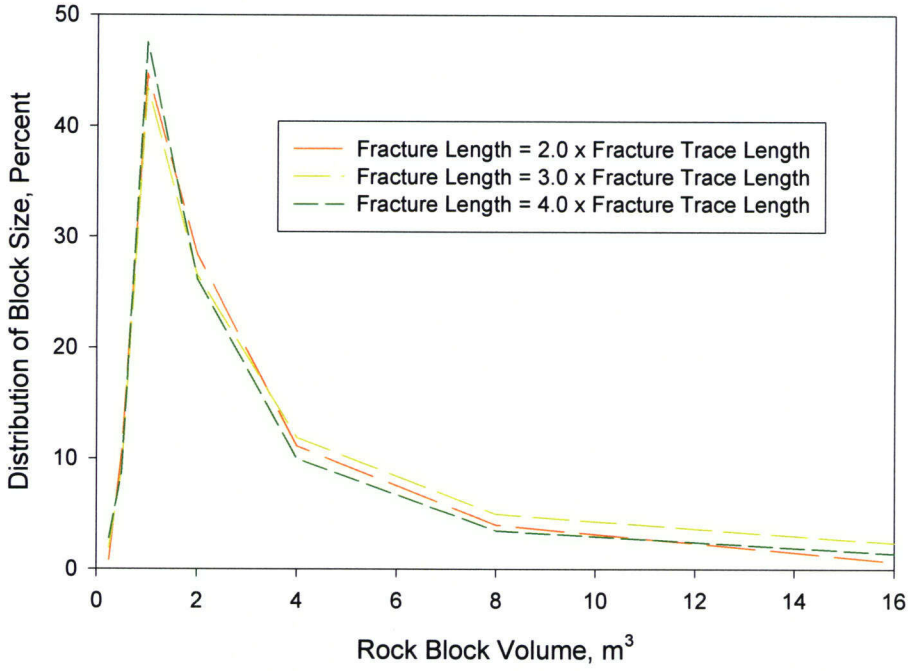

Figure 4-11. Normalized Histogram of Rock Block Size Distribution for the Topopah Spring Welded Tuff Middle Nonlithophysal Rock Unit

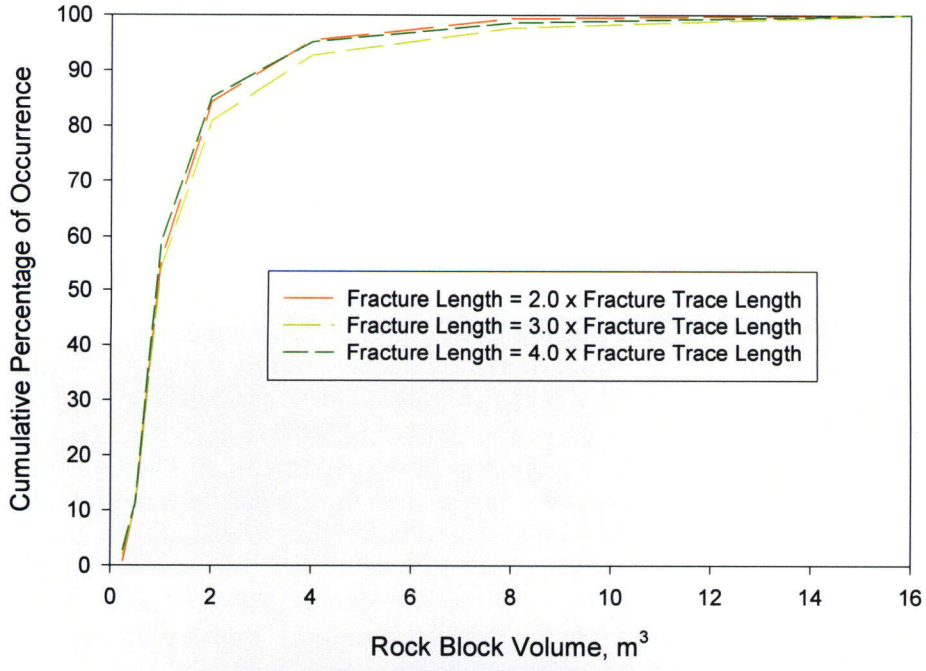

Figure 4-12. Cumulative Rock Block Size Distribution for the Topopah Spring Welded Tuff Middle Nonlithophysal Rock Unit

4.2.2 Discrete Rock Block Loads

Although rock blocks of sufficient size to cause appreciable damage to the drip shield can be expected to occur at any time as a result of the various rock mass degradation processes described earlier, a satisfactory basis for how many, and when, they will fall does not exist at this time. As a result, it is simply assumed for the development of the MECHFAIL Total-system Performance Assessment code module that discrete rock block impact loads on the drip shield will occur only when a seismic event of a sufficient magnitude occurs. Figure 4-13 (Owen and Scholl, 1981) indicates that observable minor damage to the drift can be expected for seismic events exhibiting peak ground accelerations calculated at the surface in the range of 0.2–0.5 g. Figure 4-13 also indicates that seismic events with peak ground accelerations calculated at the surface in the range of 0.5–0.8 g will cause damage to the drift. It is important to observe that the peak ground accelerations used to correlate the extent of damage to the drift are calculated at the ground surface. This observation is significant because the peak ground accelerations measured within a subsurface excavation are typically less than those measured at the ground surface. For the case of Yucca Mountain, however, recent information presented by DOE[2] indicates that they will be using the free surface ground motions for the subsurface repository horizon design basis ground motions. In general, a condition of no damage corresponds to no new cracks, spalls, or falls of ground being developed. Minor damage is defined to be observable new cracking and minor rockfalls, and major damage is correlated with severe cracking, major rockfalls, and closure.

Many researchers have proposed using particle velocities as an alternative to using peak ground accelerations at the ground surface to estimate the damage incurred by subsurface excavations (NRC, 1991). In summary, loose rock will begin to fall for particle velocities of 0.050 m/s [0.164 ft/s], 0.300 m/s [0.984 ft/s] for ground falls, and 0.600 m/s [1.969 ft/s] for severe damage. Because the Total-system Performance Assessment code limits its characterization of seismic ground motions to mean peak horizontal ground accelerations, it was decided that the amount of rockfall caused by a seismic event would be based on this parameter.

4.2.3 Discrete Rock Block Load Abstraction

Assuming that the damage to the drift can be represented by a change in the drift degradation zone failure height that is proportional to the magnitude of the seismic event peak ground acceleration, pga, the total volume of falling discrete rock blocks can be estimated. Referring to Figure 4-14, the increase in the drift degradation zone failure height for a given seismic event depends on the peak ground acceleration needed to cause minor damage, g_o, the peak ground acceleration needed to cause major damage (i.e., drift closure), g_{max}, and the maximum drift degradation zone failure height, H_{max}. The relationship shown graphically in Figure 4-14 is represented mathematically in the following equation.

[2]DOE and NRC Public Meeting. Las Vegas, Nevada. August 6–8, 2002.

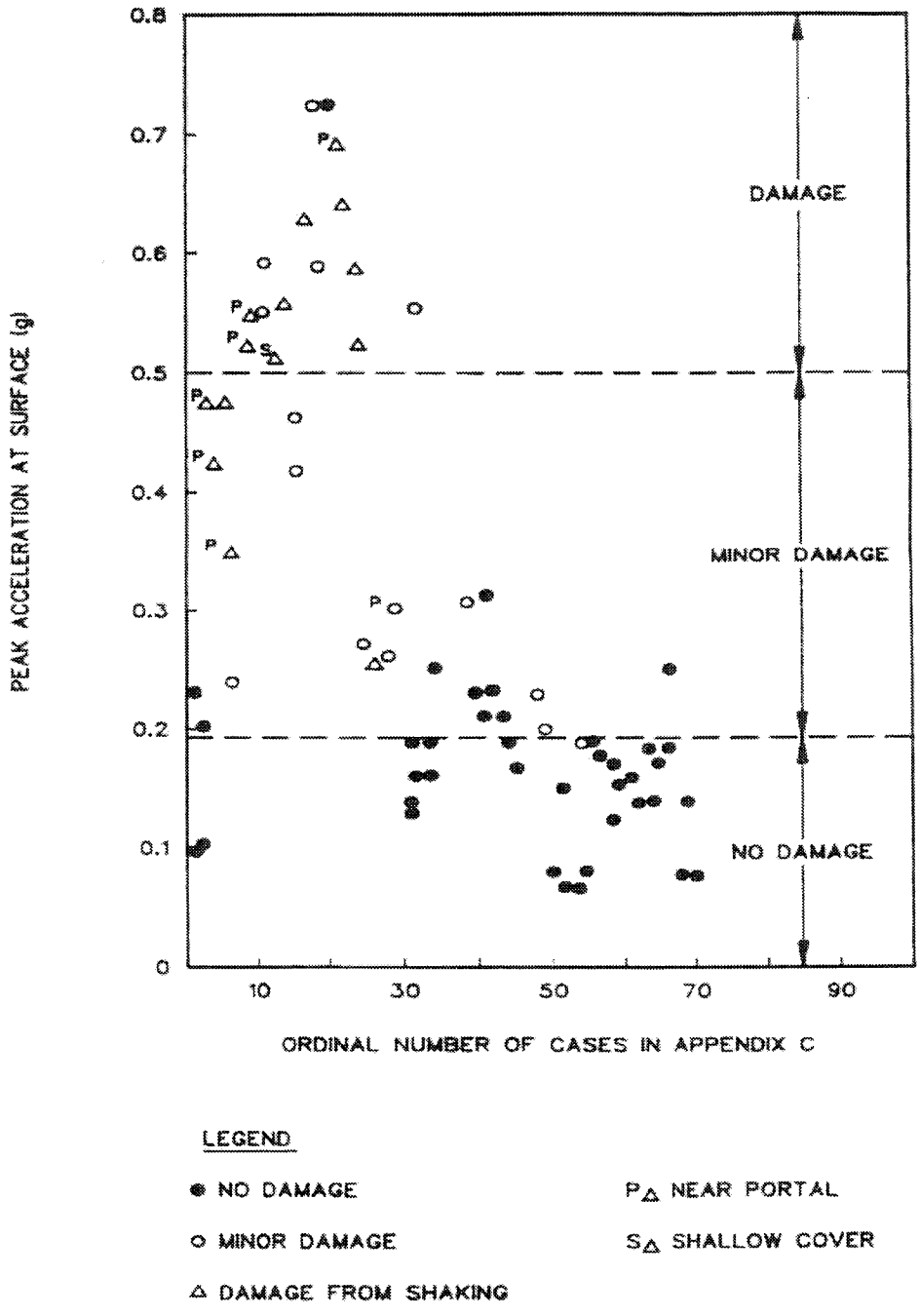

Figure 4-13. Characterization of Drift Damage as a Function of Ground Surface Peak Ground Accelerations (Owen and Scholl, 1981)

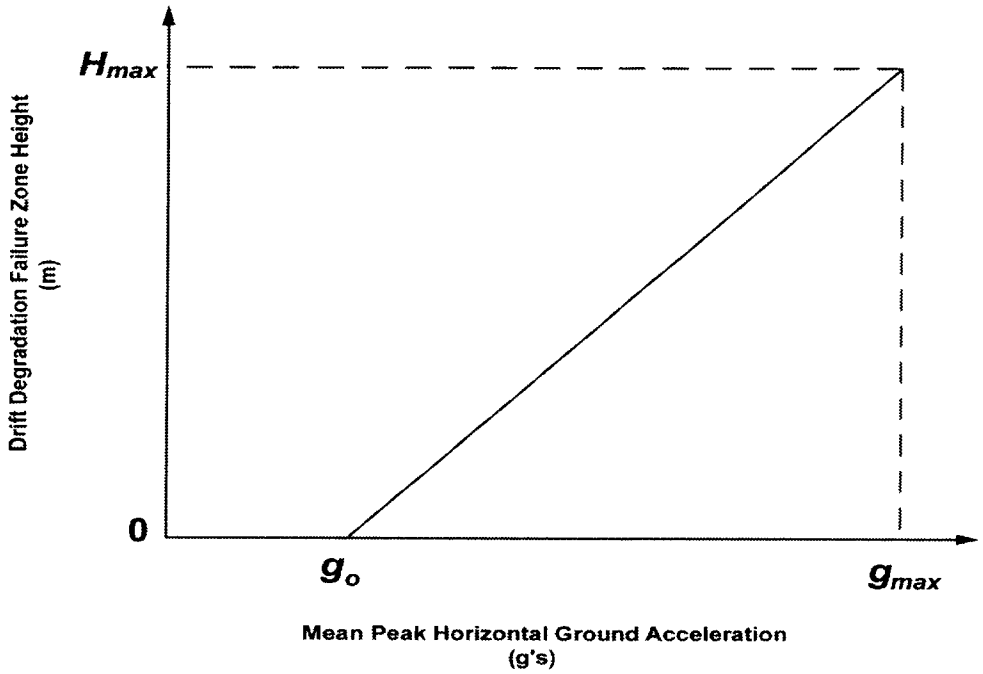

Figure 4-14. Change in the Drift Degradation Zone Failure Height as a Function of Mean Peak Horizontal Ground Acceleration

$$\Delta h = \frac{(H_{max} - h_{i+1})}{(g_{max} - g_o)}(\text{pga} - g_o) \qquad (4\text{-}12)$$

Note that the slope of the curve is updated as the drift degradation zone failure height changes. This change in slope is intended to account for the increased drift stability expected to occur as the drift degradation zone failure height increases. When implemented within the MECHFAIL module the drift degradation zone failure height is updated first using Eq. (4-11) to account for the rockfall associated with the coupled thermal, mechanical, hydrological, and chemical processes by way of the drift degradation rate over the timestep leading up to the additional rockfall from the seismic event. Furthermore, each spatial grid element is assigned a value of g_o and g_{max} using beta distributions. For g_o, the minimum mean peak horizontal ground acceleration required to cause minor damage is greater than 0.2 g, and no more than 20 percent of the spatial grid elements will be assigned a g_o greater than 0.24 g (see Figure 4-15). Similarly, for g_{max}, the minimum mean peak horizontal ground acceleration required to cause major damage is greater than 1.0 g, and no more than 20 percent of the spatial grid elements will be assigned a g_{max} greater than 1.20 g (see Figure 4-16). Recall that the magnitude of H_{max} is controlled by the bulking factor that was assigned to the spatial grid element (see Section 4.1). The fundamental precept of Eq. (4-12) is that there is a certain ground motion that corresponds to the onset of damage within the drift (i.e., g_o) and a ground motion (i.e., g_{max}) that will cause the drift to fail to the maximum extent allowed by the conservation of mass presented in Section 4.1. Lacking any other information, these two points have simply been connected using a straight line.

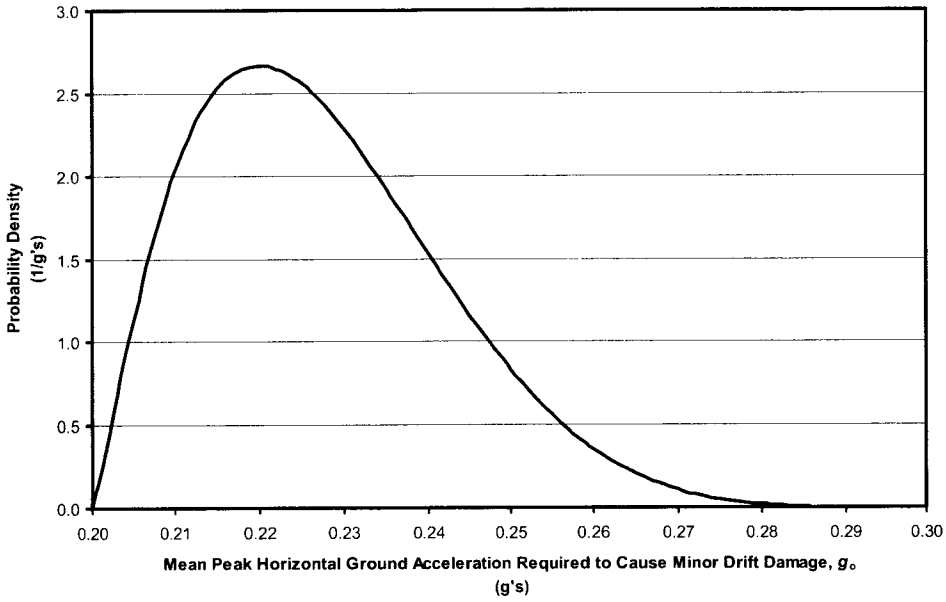

Figure 4-15. Beta Distribution Defining the Mean Peak Horizontal Ground Acceleration Required to Cause Minor Drift Damage

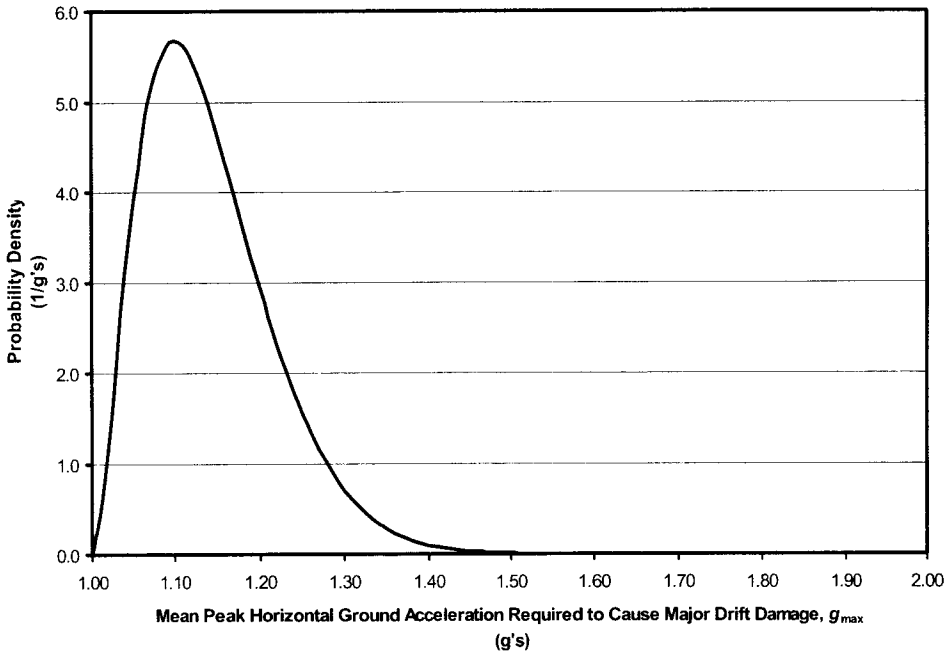

Figure 4-16. Beta Distribution Defining the Mean Peak Horizontal Ground Acceleration Required to Cause Major Drift Damage

After the change in the drift degradation failure zone height, Δh, defined in Eq. (4-12), has been calculated for its respective grid element, the volume of rockfall caused by the seismic event can be determined. The rock block size distribution curve is then sampled until the sum of the individual rock block volumes is greater than the total volume of rockfall calculated for the seismic event. The individual rock blocks are then sorted from largest to smallest until the sum of the individual rock block volumes is greater than the total volume of rockfall calculated for the seismic event. This sorting process is performed to ensure a large rock block is not thrown out of the sample simply because it was the last rock block retrieved from the rock block size distribution curve. These rock blocks are then assumed to impact the drip shield with a fall height equal to h_{i+1}. Lastly, once the accumulated amount of rockfall is sufficient to cover the drip shield crown under a 0.5 m [1.64 ft] depth of rock rubble, the effects of discrete rock blocks impacting the drip shield are no longer calculated. The rockfall caused by the occurrence of seismic events is still accounted for in the static rockfall loads after this threshold is met, however.

5 DRIP SHIELD AND ACCUMULATED ROCKFALL STATIC LOAD PERFORMANCE ANALYSES

It is expected that varying amounts of rock debris or rubble will accumulate around the drip shield during the 10,000-year regulatory period. An understanding of the response of the various components of the engineered barrier subsystem—including the drip shield, waste package, waste form, pallet, invert, and drift—to these static loads is needed. Furthermore, potential interactions between the components must be understood. This chapter documents the work accomplished thus far in understanding the effects of accumulated rockfall load on the drip shield. Sections 5.1 and 5.2 discuss the methodology used to simulate drip shield performance and the resultant stress and deflection data. Section 5.3 discusses how these data have been used to model the response of the drip shield to static rockfall loads in the MECHFAIL Total-system Performance Assessment code module.

5.1 Finite Element Model Description

This section documents the finite element analyses that were performed to assess the effects of accumulated static rockfall loads on the drip shield. The fundamental assumption employed in the construction of the finite element models used for this purpose was that the static rockfall loads acting on the drip shield are symmetrically distributed over the drip shield surface.

It was recognized early in the drip shield modeling process that the drip shield structural behavior will be affected by the rock rubble that has accumulated around its sides. It is not sufficient, however, to simply apply a static distribution of pressure down the side of the drip shield because this would allow large deflections of the drip shield side walls. The rock rubble accumulated on the sides of the drip shield and confined by the accumulated rock above will enhance the structural stability and stiffness of the drip shield. Therefore, the rock material interacting with the drip shield is modeled in two parts. The first part is the distributed pressure load acting over the drip shield crown surface (see Section 5.1.2). The second part is a solid model of the rock rubble that interacts with the side of the drip shield. The top surface of this rock rubble is subjected to a confining pressure created by the accumulated rubble above the modeled section (see Sections 5.1.1 and 5.1.2).

Several simulations were performed to assess the response of the drip shield for varying magnitudes of static rockfall loads and the effective Young's Modulus of the rock rubble accumulated on the sides of the drip shield.

5.1.1 Finite Element Model Geometry

The finite element model of the drip shield subjected to static rockfall loads consists of four major components. These components are the drip shield, the rockfall rubble, invert, and the drift wall. Figure 5-1 shows the layout of these components, while Figure 5-2 highlights the individual components that make up the drip shield. As can be seen from Figure 5-1, the finite element model takes advantage of the geometrical, loading, and kinematic symmetry conditions assumed to exist to prepare an efficient model for simulation. Geometrically, it is assumed that

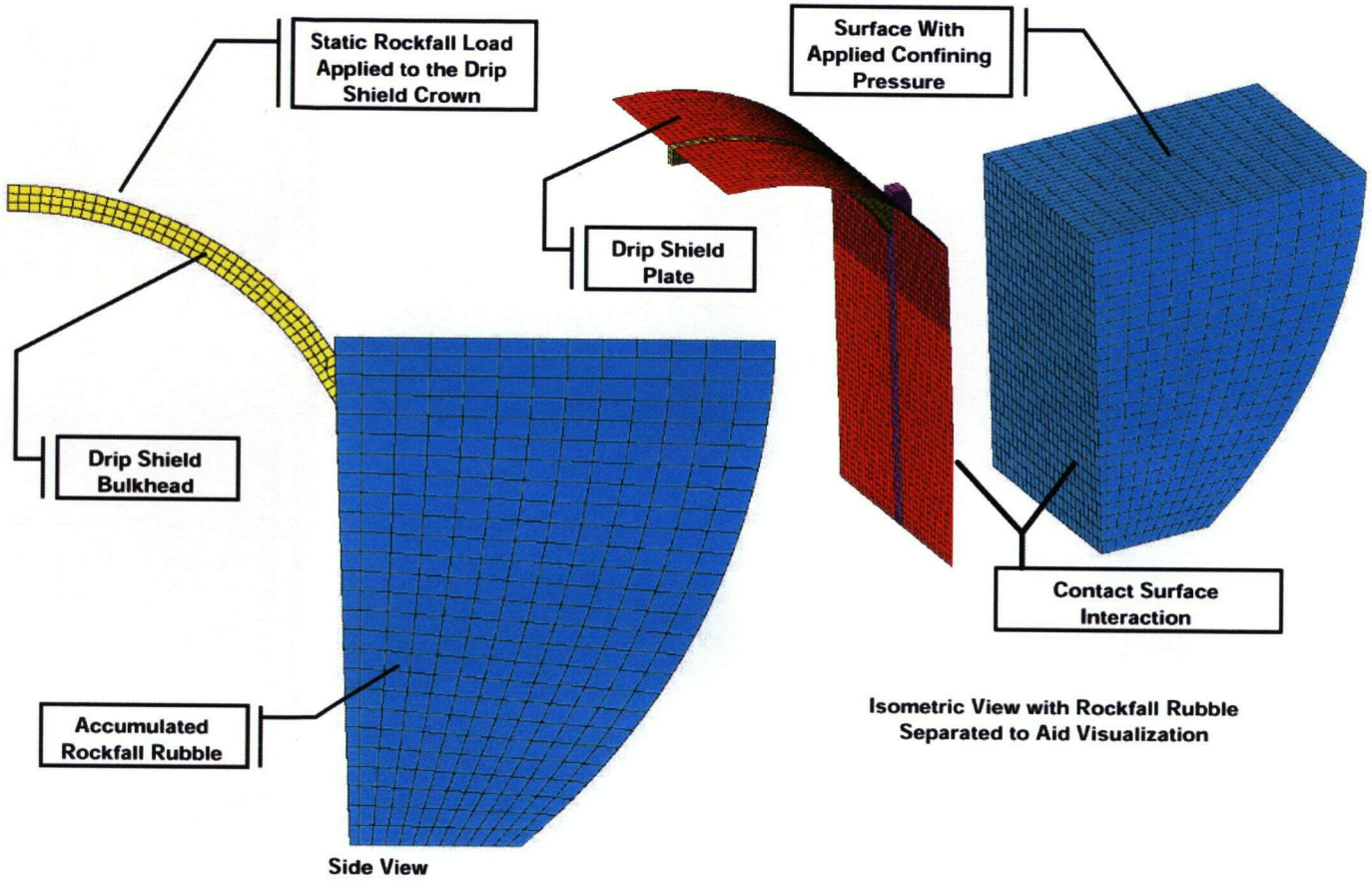

Figure 5-1. Drip Shield and Accumulated Rockfall Interaction Model

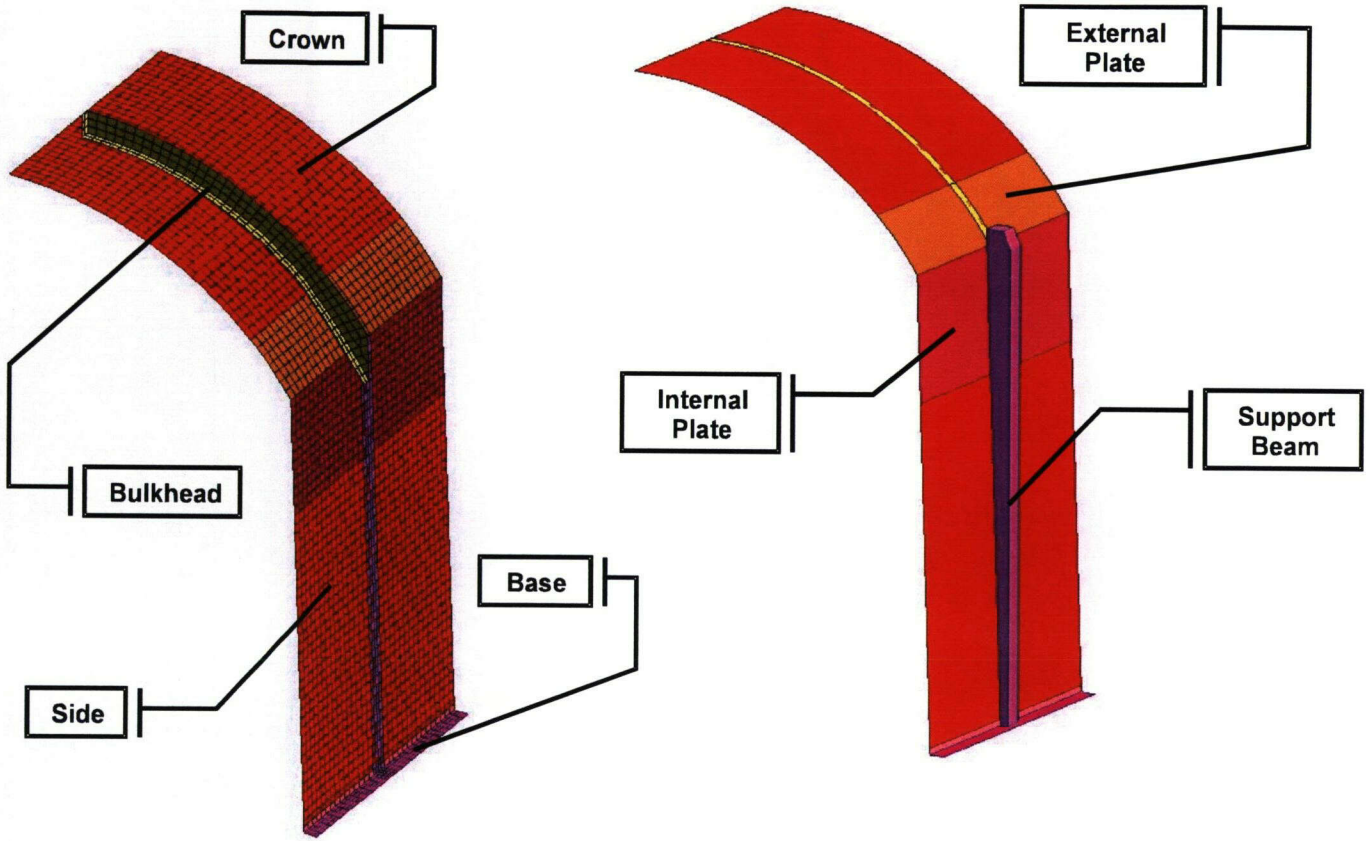

Figure 5-2. Drip Shield Components

the drip shield segments, defined by the uniform axial spacing of the support beam and bulkhead reinforcing members, repeat continuously in the axial direction. The resulting model is cut at the axial and lateral symmetry planes as shown in Figure 5-3.

The model was constructed using a mixture of plate and solid elements. Plate elements (three-dimensional quadrilaterals) are used for the Titanium Grade 7 panel sections, including the drip shield crown, side plating, and inner and outer stiffening plates. Plate elements were also used to represent the Alloy 22 base of the structure. Solid elements (three-dimensional hexahedrons) are used to represent the major structural support beam and bulkhead components (CRWMS M&O, 2000a, Reference Sketch Number SK–0148, Revision 05).

Linear material behavior and small strains were assumed for the drip shield models subjected to static rockfall loads. As a result, the use of plate elements to represent thin structural members, such as the Titanium Grade 7 plate regions, was justified. This approximation does not provide accurate results, however, if the drip shield undergoes large deformations that significantly change the geometry of the structure relative to its original configuration. Large deflection theory accounts for changes in load distribution created by the large deformations and uses a more robust mathematical formulation for calculating strains such that large rigid body rotations within the finite element model do not erroneously predict strains. The ability to use plate elements in the construction of the drip shield finite element model significantly reduces the memory requirements and computational times required to perform the analyses relative to a model comprised solely of solid elements.

5.1.2 Finite Element Model Boundary Conditions

5.1.2.1 Loads

Static pressure loads are applied to the drip shield crown and the top surface of the solid continuum elements representing the rockfall rubble that has accumulated on the sides of the drip shield. The distribution of the pressure load acting on the drip shield crown and on top of the rockfall rubble was derived from Eq. (4-4). Table 5-1 summarizes the static rockfall load history used in the model. The loads identified in Table 5-1 correspond to the maximum static rockfall loads for a given bulking factor.

5.1.2.2 Kinematic Constraints

The lateral symmetry condition constrains out-of-plane lateral translations and rotations. This particular constraint precludes the drip shield from leaning or sliding laterally into the waste package. Further analysis would be required to determine if a one-sided buildup of rockfall rubble constitutes a design risk for the drip shield or waste package.

The axial symmetry condition constrains translations and rotations out of the axial plane. This constraint is analogous to a two-dimensional plane strain assumption and implies that the static rockfall load is uniformly applied along the entire length of the drip shield.

The accumulated rubble interacting with the side of the drip shield was modeled using a contact definition that allowed the rubble to slide along the interface without separation. This type of contact definition allows the rockfall rubble to conform to the changing orientation of the drip

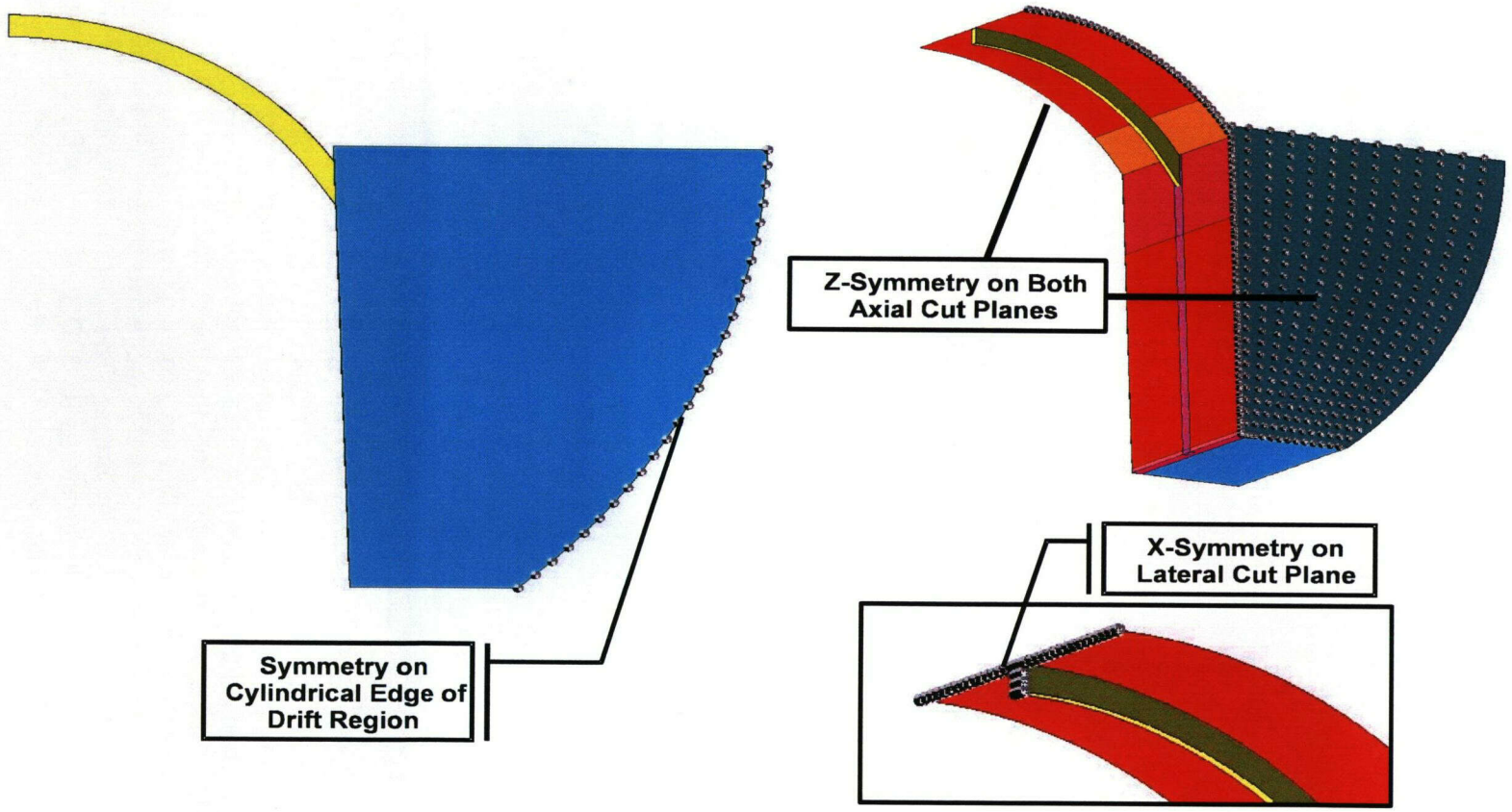

Figure 5-3. Drip Shield and Accumulated Rockfall Rubble Interaction Model Kinematic Boundary Conditions

Table 5-1. Maximum Static Rockfall Loads for a Given Bulking Factor				
Load Step	Bulking Factor	Maximum Crown Pressure, MPa [psi]	Average Rock Rubble Overburden Pressure, MPa [psi]	Total Vertical Load, tonne/m [lb/ft]
1	1.5	0.156 [22.6]	0.150 [21.8]	40.0 [26,890]
2	1.4	0.198 [28.7]	0.189 [27.4]	50.9 [34,210]
3	1.3	0.272 [39.4]	0.255 [37.0]	69.3 [46,580]
4	1.2	0.420 [60.9]	0.388 [56.3]	106.5 [71,590]
5	1.1	0.869 [126.0]	0.789 [114.4]	218.7 [147,010]

shield wall as it deforms during the analysis. The invert and drift wall are modeled as a single analytical rigid body such that the drip shield and rockfall rubble are properly supported and constrained within the confines of the drift.

5.1.3 Finite Element Model Material Properties

Derivation of the drip shield component material properties and constitutive models were presented in detail in a previous report (Gute, et al., 2001). For the sake of completeness, however, Table 5-2 provides a summary of the basic material data used in the drip shield finite element models presented in this report. Table 5-3 indicates which material is assigned to each component shown in Figure 5-2. The values for density and Poisson's ratio delineated in Table 5-2 correspond to room temperature values. Any potential differences in density and Poisson's ratio between the assumed temperature of 150 °C [302 °F] and room temperature are not expected to be significant with regard to the various drip shield analyses presented in this report. The Young's moduli for the different materials, on the other hand, have been adjusted to account for the effects of temperature. The Young's modulus for Titanium Grade 7 was obtained from Table TM–5 of the ASME International (2001) Boiler and Pressure Vessel Code. The Young's modulus for Alloy 22 was obtained from Table TM–3 of the ASME International (2001) Boiler and Pressure Vessel Code. Note that the Young's modulus for Alloy 22 was not explicitly provided in Table TM–3 of the ASME International (2001) Boiler and Pressure Vessel Code. The value for Young's modulus at 150 °C [302 °F] provided for nickel alloy Uniform National Standard number N06455 was used for Alloy 22 because of its similarity in alloy composition to Alloy 22. The temperature-dependent values for the Young's moduli of Titanium Grade 5 or Titanium Grade 24 are not provided in the ASME International (2001) Boiler and Pressure Vessel Code. Note that the composition of Titanium Grade 5 and Titanium Grade 24 are the same except that the Titanium Grade 24 contains 0.04 to 0.08 percent palladium. As a result, it is expected that these two grades will exhibit similar mechanical behavior (i.e., mechanical properties). The *Military Handbook: Metallic Materials and Elements for Aerospace Vehicle Structures* (U.S. Department of Defense, 1998) and *Material Properties Handbook: Titanium Alloys* (ASM International, 1994) provide extensive material data for Titanium Grade 5. The Young's modulus for Titanium Grade 5 corresponding

Table 5-2. Summary of Drip Shield Material Property Data			
Material Name	**Density, tonne/m³ [lb/in³]**	**Young's Modulus, GPa [psi]**	**Poisson's Ratio**
Titanium Grade 7	4.512 [0.163][*]	100.7 [14.6 × 10⁶][†]	0.32[‡]
Titanium Grade 24	4.512 [0.163][*]	107.2 [15.5 × 10⁶][§]	0.32[‡]
Alloy 22	8.691 [0.314][‖]	197.2 [28.6 × 10⁶][¶]	0.32[‖]

[*]ASME International. "ASME International Boiler and Pressure Vessel Code." New York City, New York: ASME International. Table NF–2, Typical Physical Properties of Nonferrous Materials (Unalloyed Titanium). 2001.
[†]ASME International. "ASME International Boiler and Pressure Vessel Code." New York City, New York: ASME International. Table TM–5, Moduli of Elasticity of Titanium and Zirconium for Given Temperatures. 2001.
[‡]ASME International. "ASME International Boiler and Pressure Vessel Code." New York City, New York: ASME International. Table NF–1, Typical Mechanical Properties of Materials (Unalloyed Titanium). 2001.
[§]U.S. Department of Defense. "Military Handbook: Metallic Materials and Elements for Aerospace Vehicle Structures." MIL–DBK–5H. Washington, DC: U.S. Department of Defense. Figure 5.4.1.1.4, Effect of Temperature on the Tensile and Compressive Moduli of Annealed Ti–6Al–4V Alloy Sheet and Bar. 1998.
ASTM International. "Standard Specification for Low-Carbon Nickel-Molybdenum-Chromium, Low-Carbon Nickel-Chromium-Molybdenum, Low-Carbon Nickel-Chromium-Molybdenum-Copper, Low-Carbon Nickel-Chromium-Molybdenum-Tantalum, and Low-Carbon Nickel-Chromium-Molybdenum-Tungsten Alloy Plate, Sheet, and Strip." New York City, New York: ASTM International. 1998.
[¶]ASME International. "ASME International Boiler and Pressure Vessel Code." New York City, New York: ASME International. Table TM–4, Moduli of Elasticity of High Nickel Alloys for Given Temperatures. 2001.

Table 5-3. Drip Shield Component Materials			
Drip Shield Component	**Titanium Grade 7**	**Titanium Grade 24**	**Alloy 22**
Crown	X		
Side Plating	X		
Inner Plate Stiffener	X		
Outer Plate Stiffener	X		
Bulkhead		X	
Support Beam		X	
Base			X

to a temperature of 150 °C [302 °F] was derived from graphical data provided in the *Military Handbook: Metallic Materials and Elements for Aerospace Vehicle Structures* (U.S. Department of Defense, 1998). As Table 5-2 indicates, the density and Poisson's ratio used in the analysis for the Titanium Grade 24 drip shield components were the same as those used for Titanium Grade 7. According to the *Military Handbook: Metallic Materials and Elements for Aerospace Vehicle Structures* (Table 5.4.1.0(b); U.S. Department of Defense, 1998), more appropriate room temperature values for density and Poisson's ratio would be 4,429.0 kg/m³ [0.160 lb/in³] and 0.31. These values do not appreciably vary from those used in the analyses and the

results presented in this report, therefore, are well within acceptable engineering tolerances. Nevertheless, the updated values for density and Poisson's ratio will be used in future analyses. Additional drip shield material properties of interest are tabulated in Table 5-4. These properties have been adjusted from their standard engineering stress and strain values to their corresponding Cauchy stress and logarithmic strain counterparts (Gute, et al., 2001). This adjustment was needed to satisfy the requirements of the ABAQUS finite element code used to perform the analyses presented in this report.

The rock rubble on the sides of the drip shield is modeled as a continuum. Therefore, the behavior of the rubble in this region must be captured by using an appropriate constitutive model with compatible material properties. Preferring to use a simple linear elastic constitutive model for the rock rubble, reasonable estimates for the rubble Young's modulus and Poisson's ratio are required. Documented data for the Young's modulus of various crushed aggregates or granular materials indicate that significant variability of this parameter should be expected [e.g., Marsal (1973)]. In fact, it was found that the Young's moduli for these materials can be several orders of magnitude smaller than the moduli for their intact condition. Moreover, the documented values of Young's moduli for these materials were found only for confining pressures that are well above those expected for the rock rubble interacting with the drip shield. The effective Young's moduli for rock rubble increases as the confining pressure increases. Because of this large variability, it was decided to evaluate the potential significance of Young's moduli of the rock rubble over the range identified in Table 5-5 to determine its relevance on the structural behavior of the drip shield under static rockfall load conditions. Note that the values used in Table 5-5 for the Young's moduli were derived from data provided by Marsal (1973) under what can be considered to be high confinement pressures relative to what is expected to be the case for the conditions being modeled here. For the expected confining pressure experienced by the rock rubble, staff estimate that the effective Young's moduli should lie within the range of 10 to 100 kPa [1.45 to 14.5 psi].

The lateral pressure exerted on the walls of the drip shield by the rockfall rubble can be approximated using the ratio of horizontal (or lateral) to vertical (or confining) pressure at rest, (i.e., K_o). According to Lambe and Whitman (1969, Figure 13.7), K_o = 0.2 for the condition of no horizontal strain, which is assumed to be the case here because of the plane strain conditions applicable in the axial direction and the presence of the drip shield and drift wall restricting or limiting lateral strain. In other words, only vertical, uniaxial strain is expected to result from the confining pressure acting on the top surface of the continuum elements representing the rock rubble that has accumulated on the sides of the drip shield. For these conditions, the ratio of horizontal to vertical pressure (or stress) can be shown to be

$$K_o = \frac{\sigma_H}{\sigma_V} = \frac{\nu}{(1-\nu)} \qquad (5\text{-}1)$$

where

ν — poisson's ratio
σ_H — horizontal stress
σ_V — vertical stress.

Table 5-4. Drip Shield Material Data for Modeling Post-Yield Behavior			
Material Name	**Yield Stress,* MPa [psi]**	**Ultimate Tensile Strength,* MPa [psi]**	**Log Normal Failure Strain, Percent**
Titanium Grade 7	174.1 [2.53 × 10^4]	299.5 [4.34 × 10^4]	17.93
Titanium Grade 24	658.1 [9.54 × 10^4]	827.0 [1.20 × 10^5]	8.76
Alloy 22	254.7 [3.69 × 10^4]	984.7 [1.43 × 10^5]	36.7
*Cauchy Stress			

Table 5-5. Case Numbers for the Assumed Rock Rubble Young's Moduli Evaluated	
Case	**Young's Modulus MPa [psi]**
1	no rock
2	3.0 [4.35 × 10^2]
3	6.0 [8.70 × 10^2]
4	10.0 [1.45 × 10^3]
5	30.0 [4.36 × 10^3]

For the assumption that K_o = 0.2, Eq.(5-1) can be used to calculate the corresponding value of Poisson's ratio (i.e., ν = 0.17).

5.2 Summary of Analysis Results

The various simulations of the drip shield subjected to static rockfall loads were run until the full load was applied or until the drip shield structure became unstable (i.e., the onset of buckling was determined). The unstable condition is characterized by large deflections of the drip shield crown and yielding of the bulkhead and plate components. The deflections and stresses experienced by the drip shield under static rockfall load conditions for the different rockfall rubble material property cases were similar up to the occurrence of buckling (i.e., locations of maximum stress). Therefore, unless noted otherwise, the figures that illustrate drip shield performance under static rockfall load conditions in the remainder of this section correspond to Case 4 (see Table 5-5).

5.2.1 Drip Shield Deflection

Figure 5-4 summarizes static rockfall load versus drip shield deflection for each of the rock rubble material property variations that were simulated. Figure 5-4 illustrates that the drip shield buckling load is reduced as the Young's modulus of the rockfall rubble accumulated on

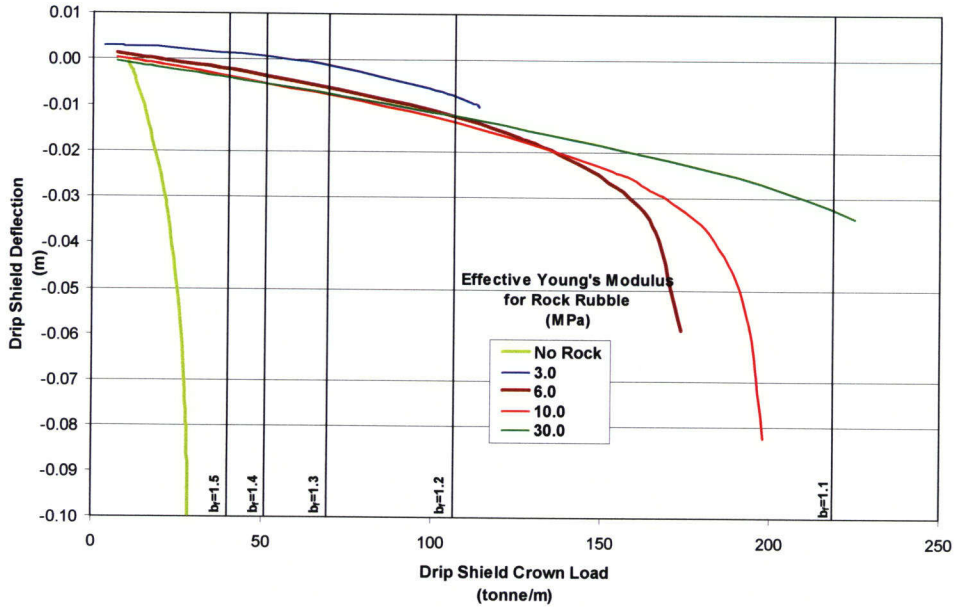

Figure 5-4. Drip Shield Deflection Versus Static Rockfall Load for Varying Rock Rubble Youngs' Moduli

its sides is reduced. This result was to be expected because a stiffer material will provide more support for buttressing the drip shield.

Figure 5-5 illustrates the drip shield deforming and interacting with the accumulated rockfall material. In general, the drip shield side wall will be pushed into contact with the rockfall rubble as the initial, smaller magnitude static rockfall loads are first applied to the drip shield. After contact is established, the side wall and support beam become column loaded. The bulkhead arch begins to flatten and push the side wall harder into the rockfall rubble. As the static rockfall load increases on the drip shield crown, the interaction load between the drip shield side wall and rock rubble intensifies until the drip shield structure buckles. Buckling primarily occurs in the support beam, which is generally column loaded.

For the extreme condition where there is no rock rubble interaction at the drip shield side wall (i.e., Case 1), the drip shield buckles under just a 23-tonne/m [15,460-lb/ft] static rockfall load. This result illustrates the importance of modeling the interaction of the drip shield side wall and the accumulated rockfall rubble. This particular analysis also demonstrates that the drip shield, as it is currently designed, is unable to protect the waste package from static rockfall loads without taking some credit for the extra structural support provided by the rockfall rubble. In addition, the maximum drip shield load capacity as predicted by the analyses presented here is considered to be overestimated because buckling of the drip shield is predicted under ideal load and symmetry assumptions (i.e., no load eccentricities and an artificially high drip shield structural stiffness created by the assumed planes of symmetry). This conclusion is further substantiated by the recognition that these analyses did not include the effects of prior damage to the drip shield caused by dynamic rock block impacts or material creep over the long service life of the structure.

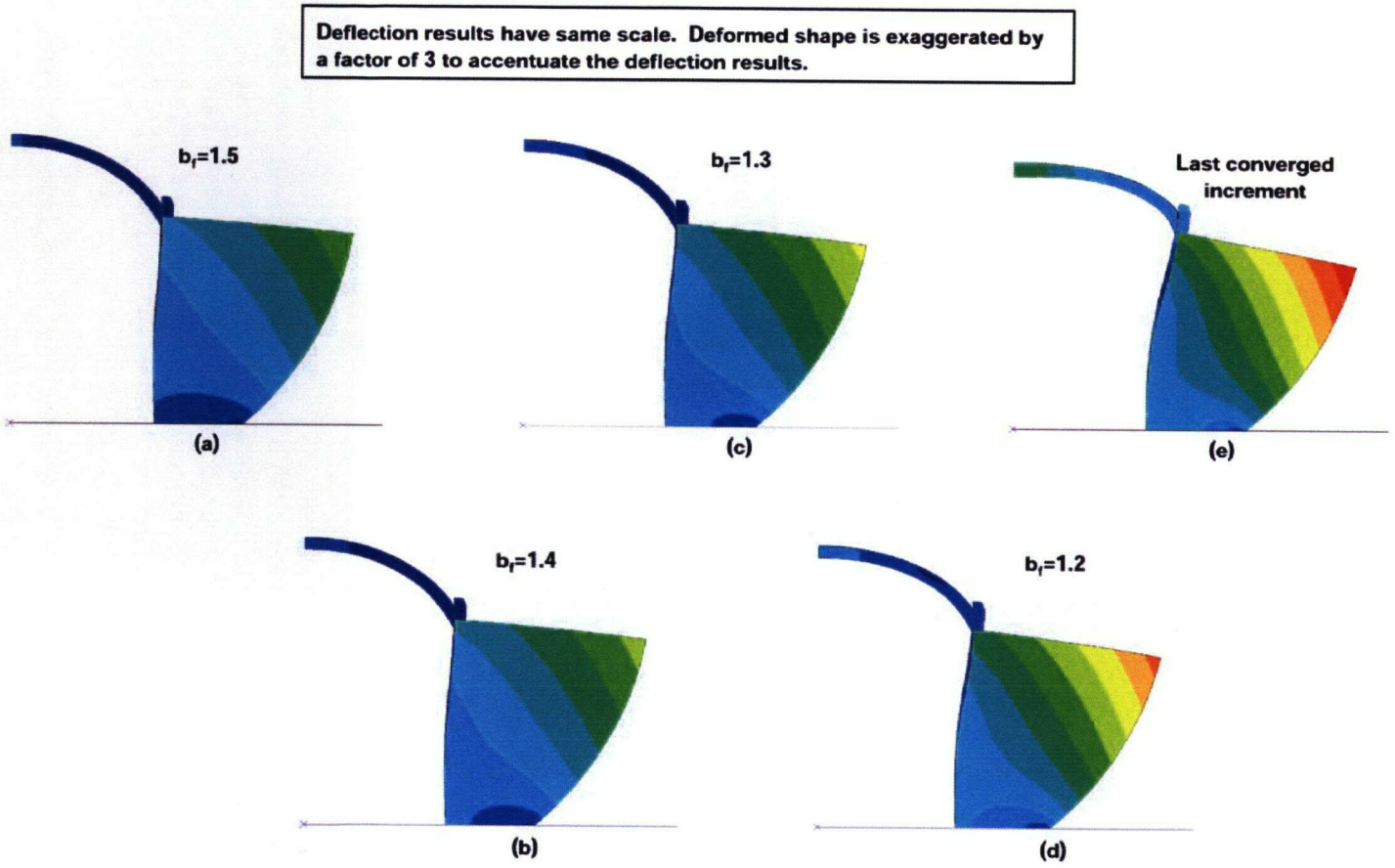

Figure 5-5. Drip Shield Deformation Under Static Rockfall Loads

5.2.2 Drip Shield Component Stresses

Bending moments are the primary source of stress in the drip shield components under static rockfall loads. The distributed pressure acting on the drip shield crown is transferred from the plate to the bulkhead which, in turn, transfers the load to the support beam. The bulkhead is loaded along its length (i.e., along the periphery of the drip shield crown) with a distributed pressure load and concentrated bending moments at its ends that are needed to satisfy static equilibrium requirements. The vertically oriented support beams ultimately carry the entire vertical rockfall load acting on the drip shield crown. The compressive load carried by the support beam, in conjunction with the concentrated bending moment acting at its top, ultimately leads to the buckling of the drip shield structure. Note that the concentrated bending moment acting at the top of the support beam is created by its connection with the bulkhead. As the static rockfall load is increased (Figures 5-6a through 5-6e), the bulkhead deflection pushes the side wall of the drip shield outward, by way of the bending moment acting at the top of the support beam, so that it comes into contact with the rockfall rubble. This interaction, in turn, will affect the magnitude and orientation of the bending moment between the bulkhead and the support beam. As illustrated in Figure 5-7, the deformation of the drip shield without accumulated rockfall interaction results in the side wall spreading out. The presence of the rockfall rubble prevents this spreading from occurring. The action and reaction cause the bending moment at the intersection of the bulkhead and support beam to change orientation.

Stresses in the drip shield plates and bulkhead quickly reach magnitudes at or above the stress threshold for the initiation of creep. According to Neuberger, et al. (2002), Titanium Grades 7 and 24 can be expected to creep at stresses above 60 percent of their yield stress. Figures 5-8 through 5-12 show the maximum von Mises stress versus accumulated rockfall load for the drip shield bulkhead components for the five different rockfall rubble cases that were evaluated. These figures show that the rise in the maximum von Mises stress value is nearly linear versus rockfall load until the yield stress is reached. The slope of the maximum von Mises stress versus rockfall load changes with the Young's modulus of the rockfall rubble. Table 5-6 conveys the vertical rockfall load acting on the drip shield crown that will result in the initiation of creep in the drip shield plate and bulkhead. Creep in both the plate and bulkhead will occur earlier with softer Young's modulus assumptions for the rockfall rubble. Stress levels within the support beam do not approach the threshold stress needed to initiate creep until after buckling has occurred.

A post-buckling analysis of the drip shield was not performed. The post-buckled drip shield structure will exhibit extremely high plastic strains in the bulkhead to support beam transition region, and a breach of the drip shield in this area should be assumed to have occurred. Figures 5-8 through 5-12 support this conclusion. Figures 5-10 and 5-11 best illustrate the fact that as the drip shield approaches its buckling load, the maximum stresses and plastic strains begin to rise dramatically. Post-buckling behavior is reasonably expected to continue this trend until the drip shield plate, bulkhead, or weld filler material fails.

In summary, the drip shield structure is not self supporting under static rockfall loads. The drip shield structure will buckle under accumulated rockfall loads of approximately 25 tonne/m [16,800 lb/ft] unless assumptions are made about the drip shield side wall interaction with the rockfall rubble. As Figure 5-13 illustrates, the drip shield buckling load is reduced significantly as the effective Young's modulus for the rock rubble approaches values that are expected to lie

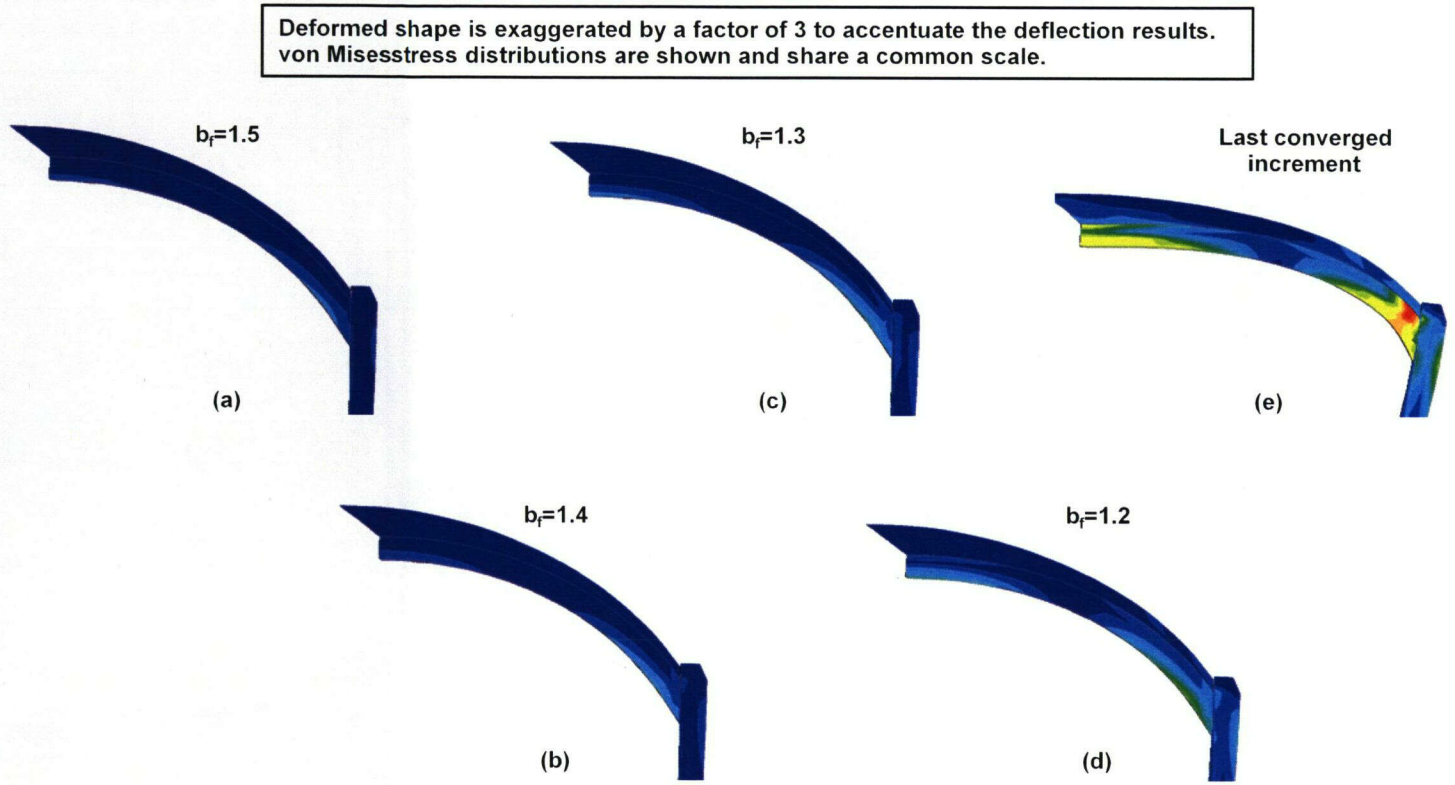

Figure 5-6. Bulkhead von Mises Stress Distribution and Deformation Corresponding to Maximum Static Rockfall Loads for Different Bulking Factors

36/72

Deformed shape is exaggerated by a factor of 3 to accentuate the deflection results.
Von Mises stress distributions are shown and do not share a common scale.

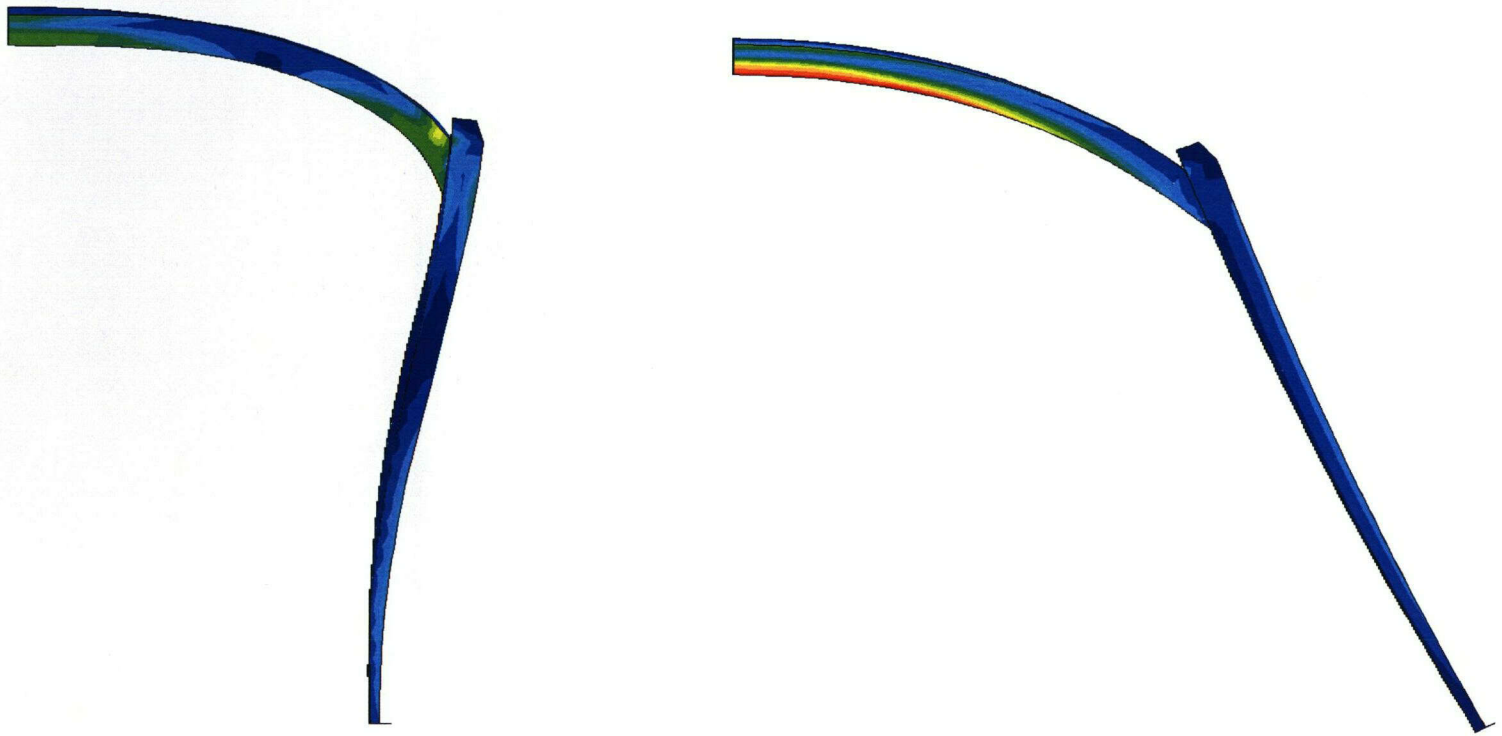

Drip Shield with Rockfall Rubble Interaction

(a)

Drip Shield without Rockfall Rubble Interaction

(b)

Figure 5-7. Comparison of Drip Shield Buckling Geometries With and Without Rock Rubble Lateral Support

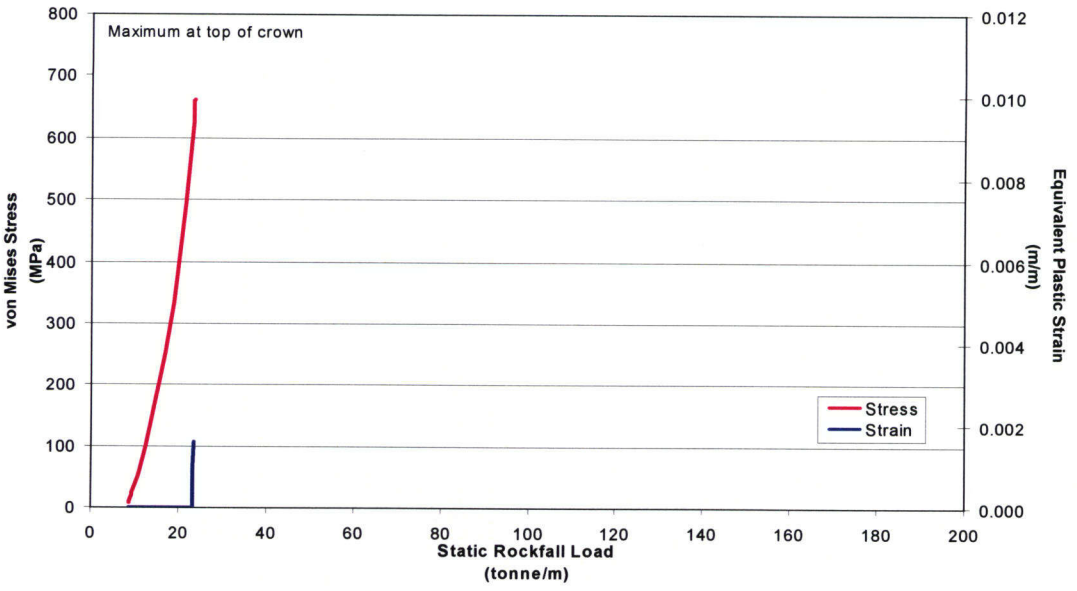

Figure 5-8. Maximum Bulkhead von Mises Stress and Equivalent Plastic Strain Versus Static Rockfall Load With No Accumulated Rockfall Rubble Lateral Support

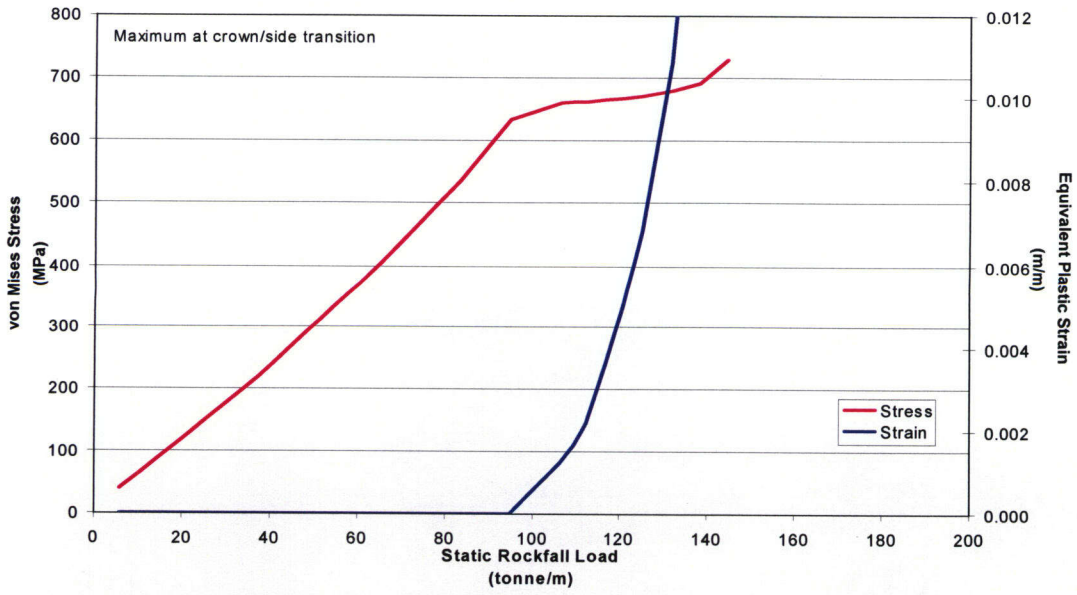

Figure 5-9. Maximum Bulkhead von Mises Stress and Equivalent Plastic Strain Versus Static Rockfall Load With Accumulated Rockfall Rubble Lateral Support {Effective Young's Modulus = 3 MPa [4.35 × 10^2 psi]}

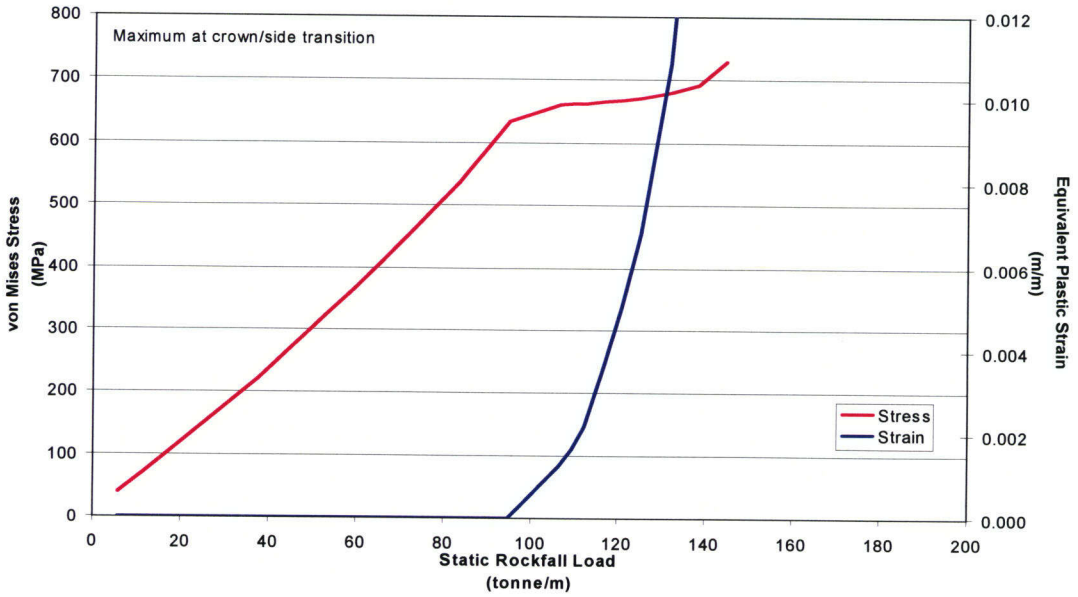

Figure 5-10. Maximum Bulkhead von Mises Stress and Equivalent Plastic Strain Versus Static Rockfall Load With Accumulated Rockfall Rubble Lateral Support {Effective Young's Modulus = 6 MPa [8.70 × 10^2 psi]}

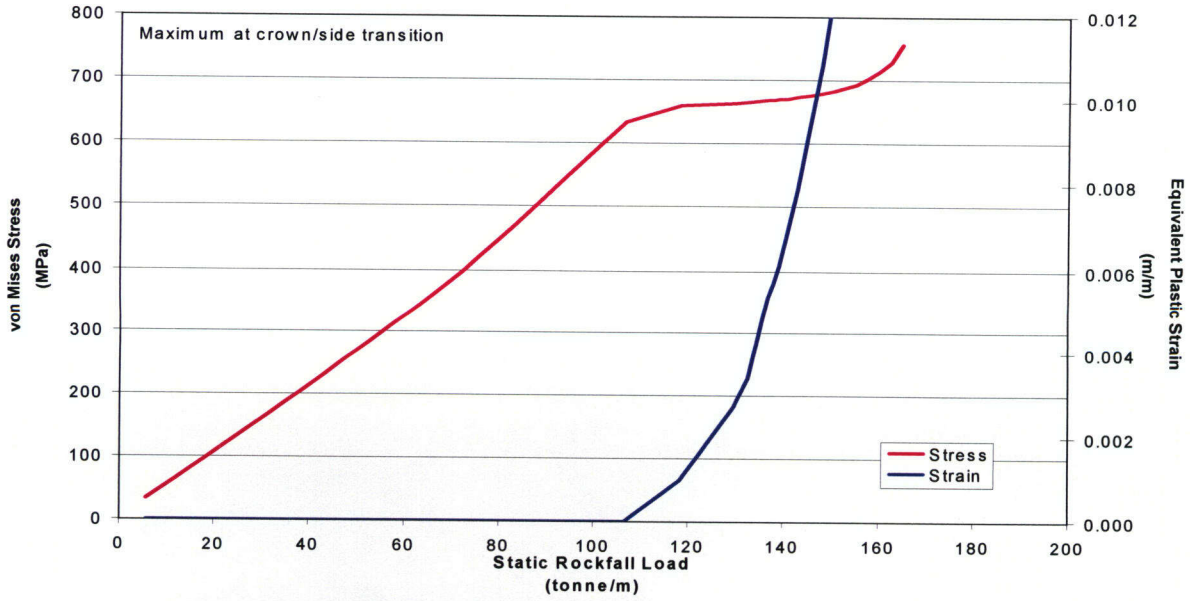

Figure 5-11. Maximum Bulkhead von Mises Stress and Equivalent Plastic Strain Versus Static Rockfall Load With Accumulated Rockfall Rubble Lateral Support {Effective Young's Modulus = 10 MPa [1.45 × 10^3 psi]}

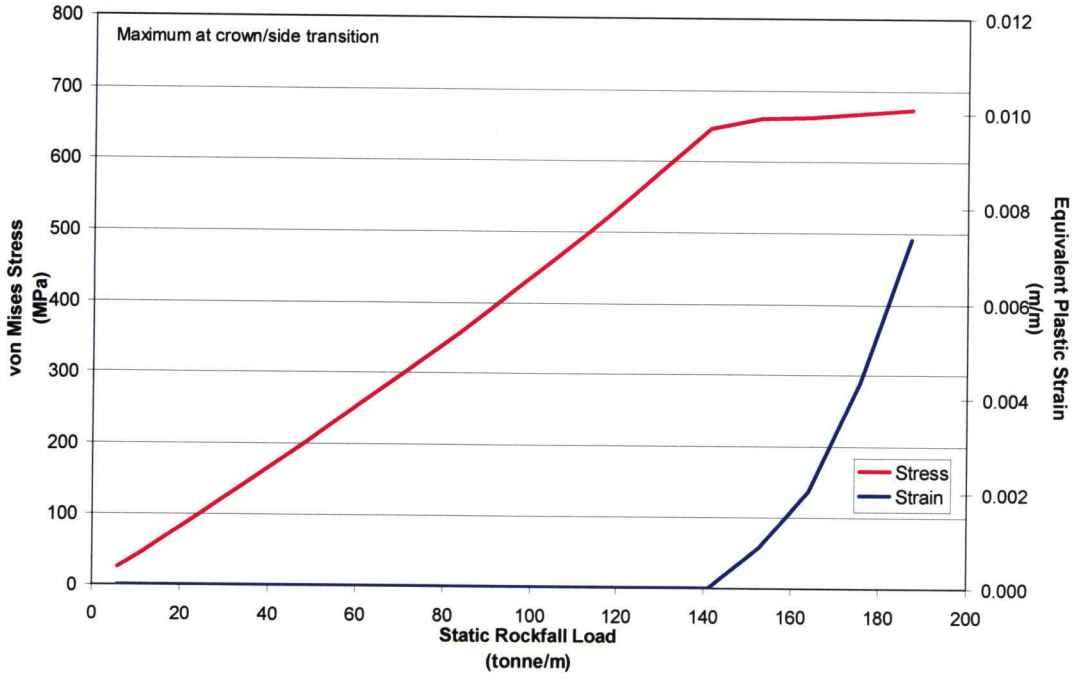

Figure 5-12. Maximum Bulkhead von Mises Stress and Equivalent Plastic Strain Versus Static Rockfall Load With Accumulated Rockfall Rubble Lateral Support {Effective Young's Modulus = 30 MPa [4.36 × 10^3 psi]}

Table 5-6. Total Static Rockfall Load Needed to Initiate Creep for Varying Rock Rubble Young's Moduli

Simulation	Rock Rubble Young's Modulus, MPa [psi]	Load at 60 percent Plate Yield, tonne/m [lb/ft]	Load at 60 percent Bulkhead Yield, tonne/m [lb/ft]	Drip Shield Buckling Load, tonne/m [lb/ft]
1	no rock	15 [10,080]	20 [13,440]	23 [15,460]
2	3.0 [4.35 × 10^2]	48 [32,270]	54 [36,300]	95 [63,860]
3	6.0 [8.70 × 10^2]	51 [34,280]	64 [43,020]	138 [92,760]
4	10.0 [1.45 × 10^3]	54 [36,300]	72 [48,400]	157 [105,540]
5	30.0 [4.36 × 10^3]	64 [43,020]	92 [61,840]	187 [125,700]

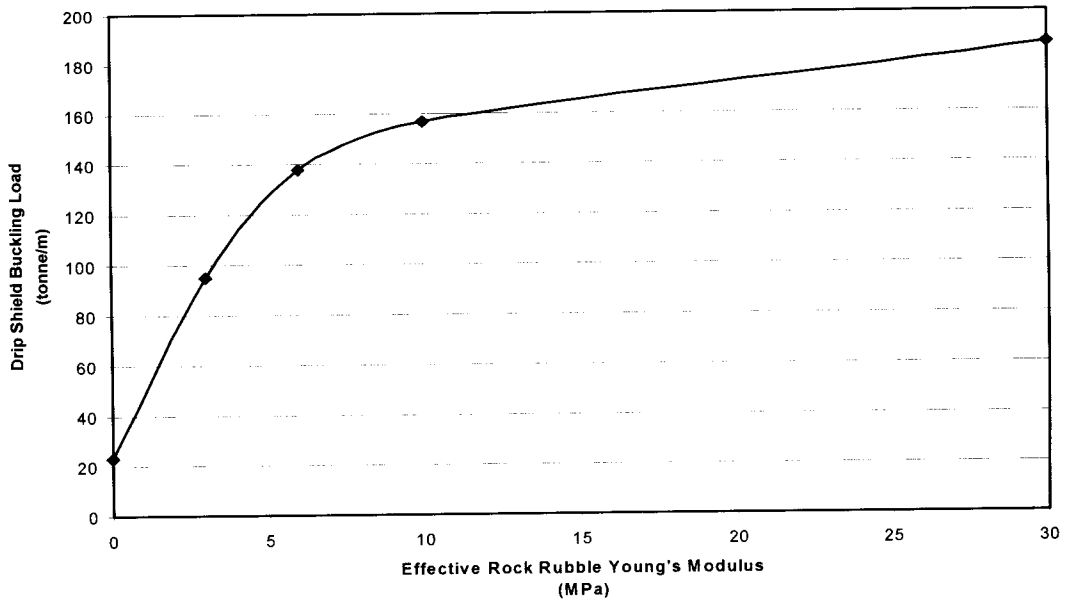

Figure 5-13. Drip Shield Buckling Load Versus Effective Rock Rubble Young's Modulus

in the range of 10 to 100 kPa [1.45 to 14.5 psi]. The drip shield may not buckle if there are no static rockfall load eccentricities and the rock rubble behaves in a very stiff manner. The physical properties of the rockfall rubble are not known with a high degree of certainty, however, and taking excessive credit for its contribution to the structural stability of the drip shield would be premature at this time. Moreover, even if the drip shield does not buckle outright from supporting the potential static rockfall loads, the drip shield plate and bulkhead are still susceptible to creep failure.

5.3 Data Abstractions for MECHFAIL

5.3.1 Drip Shield Buckling Abstraction

Because of the uncertainty associated with the behavior of the rock rubble that will accumulate around the periphery of the drip shield and its contribution to the structural stability of the drip shield, a beta function defining the drip shield buckling load has been generated (see Figure 5-14). This curve was created assuming that the drip shield will not buckle under static rockfall loads less than 25 tonne/m [16,800 lb/ft] and no more than 20 percent of the drip shields will have a buckling load threshold greater than 60 tonne/m [40,330 lb/ft]. As noted in Section 5.2.2, the staff estimate that the effective Young's moduli for the rock rubble should be within the range of 10 to 100 kPa [1.45 to 14.5 psi]. For this range of rock rubble effective Young's Moduli, Figure 5-13 indicates that the assumed drip shield buckling load distribution illustrated in Figure 5-14 is reasonable.

The drip shield buckling load distribution curve is used during the initialization phase of the MECHFAIL module to assign a drip shield buckling load to each spatial grid element. It also needs to be emphasized that the effects of a seismic event on the effective static rockfall load

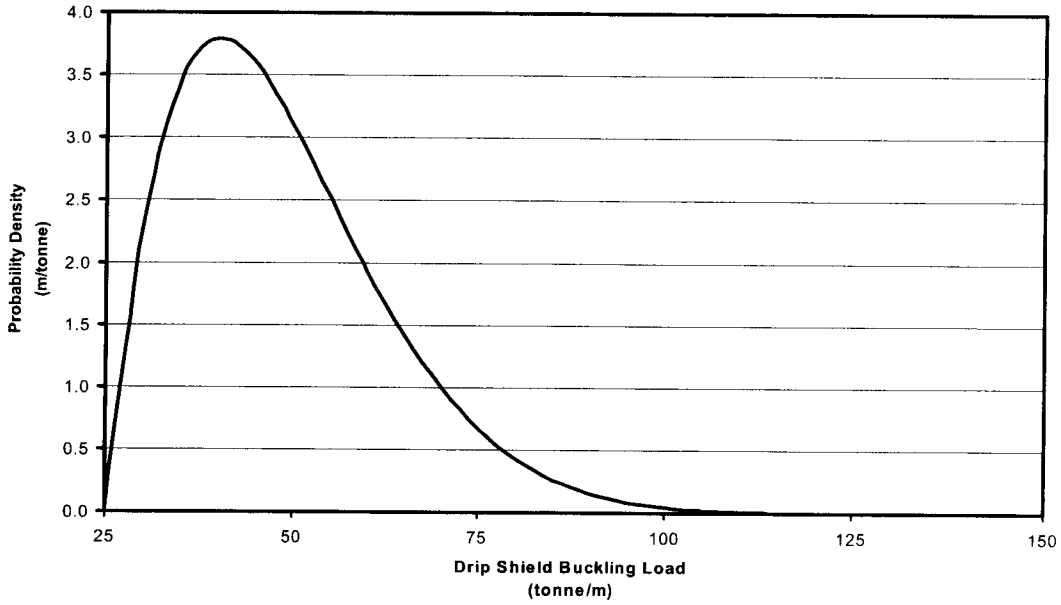

Figure 5-14. Beta Distribution Defining the Drip Shield Buckling Load

acting on the drip shield is accounted for by Eq. (5-2). This adjustment to the static rockfall load enables an accounting of those drip shields that will buckle during a seismic event.

$$L_{adj.static} = (1 + pga)\, L_{static} \qquad (5\text{-}2)$$

where

$L_{adj.\ static}$	—	static rockfall load adjusted to account for the effects of a seismic event (tonne/m)
L_{static}	—	static rockfall load (tonne/m)
pga	—	mean peak horizontal ground acceleration (g's).

At the present time, the Total-system Performance Assessment code characterizes the magnitude of a seismic event only in terms of the peak horizontal ground acceleration, which is used in Eq. (5-2) to adjust the static rockfall load. It would be more appropriate, however, to use the peak vertical ground acceleration for this purpose.

5.3.2 Drip Shield Component Stress Abstraction

The following discussion conveys the approach taken to create the functions relating static rockfall load to the maximum von Mises stress magnitude for the drip shield plate and bulkhead. These stresses are then used to calculate the magnitude of plastic strain in these components attributable to creep using the results of Neuberger, et al. (2002). Recall that the stress levels within the support beams are not sufficient to initiate creep.

Table 5-6 clearly shows that the maximum von Mises stress generated within the drip shield plate and bulkhead is strongly dependent on the Young's modulus assumed for the rock rubble. In addition, Table 5-6 also suggests a correlation between the drip shield buckling load and the maximum von Mises stress within the drip shield plate and bulkhead components. Because the drip shield buckling load is assigned to each spatial grid element using a beta distribution curve as described in Section 5.3.1, the static rockfall load required to generate stresses within the drip shield plate and bulkheads that satisfy the initiation of creep stress threshold is abstracted in terms of the assigned drip shield buckling load. Specifically,

$$L_{plate} + \left[4.903 \times 10^{0}\right] + \left[5.120 \times 10^{-1}\right] L_{buckling} - \left[1.130 \times 10^{-3}\right] L^{2}_{buckling} \quad (5\text{-}3)$$

$$L_{bulkhead} = \left[1.277 \times 10^{1}\right] + \left[3.572 \times 10^{-1}\right] L_{buckling} + \left[2.703 \times 10^{-4}\right] L^{2}_{buckling} \quad (5\text{-}4)$$

where

L_{plate} — static rockfall load (tonne/m) needed to initiate creep in the drip shield plate

$L_{bulkhead}$ — static rockfall load (tonne/m) needed to initiate creep in the drip shield bulkhead

$L_{buckling}$ — drip shield buckling load (tonne/m)

The normalized error for Eqs. (5-3) and (5-4) were calculated using the following relationship

$$L^{err} = \frac{\sum_{i}\left[L_i - L\left(L_{buckling,i}\right)\right]^2}{\sum_{i}\left[L_i\right]^2} \quad (5\text{-}5)$$

Using Eq. (5-5), the normalized error for Eqs. (5-3) and (5-4) were determined to be

$$L^{err}_{plate} = 4.29 \times 10^{-3} \quad (5\text{-}6)$$

and

$$L^{err}_{bulkhead} = 2.68 \times 10^{-3} \quad (5\text{-}7)$$

6 DRIP SHIELD AND WASTE PACKAGE INTERACTION CAUSED BY ACCUMULATED ROCKFALL STATIC LOADS PERFORMANCE ANALYSES

The analysis results presented in Chapter 5 demonstrated the propensity of the drip shield to buckle when subjected to accumulated static rockfall loads. As a result of this buckling, the static rockfall loads acting on the exterior of the drip shield will be transmitted to the waste package by way of the drip shield bulkheads. Because of the relatively small contact area between the waste package and drip shield bulkheads, at least initially, and the magnitudes of the static rockfall loads, the waste package outer barrier is expected to experience very large plastic strains. The rationale for this expectation is provided in the following discussion.

The planned thickness of the drip shield bulkhead is 0.038 m [0.125 ft] (CRWMS M&O, 2000a, Reference Sketch Number SK–0148, Revision 05). Assuming the arc length of the bulkhead initially in contact with the waste package outer barrier is 0.020 m [0.066 ft], the contact area between the bulkhead and waste package is 7.6×10^{-4} m^2 [8.2×10^{-3} ft^2]. Recalling the accumulated static rockfall load acting on the drip shield will lie somewhere in the range of 40 to 160 tonne/m [26,890 to 107,550 lb/ft] (see Figure 4-5) and recognizing that the spacing between adjacent drip shield bulkheads is approximately 1 m [3.28 ft], the resultant load transmitted to the waste package by each bulkhead will be at least 40 tonne/m [26,890 lb/ft] and no more than 160 tonne/m [107,550 lb/ft]. The average stress acting over the assumed contact area between the waste package and bulkhead will exceed the ultimate tensile strength of Alloy 22 {984.7 MPa [1.43×10^5 psi]}, the waste package outer barrier material, for a 76.3-tonne/m [51,290-lb/ft] static rockfall load. In the context of the material failure criterion defined in ASME International (2001) for Service Level D conditions, which is 90 percent of the material ultimate tensile strength, the static rockfall load that can be considered to breach the waste package outer barrier is reduced to 68.7 tonne/m [46,180 lb/ft]. The static rockfall load needed to yield {i.e., exceed the 254.7 MPa [3.69×10^4 psi] Alloy 22 yield stress} the waste package outer barrier is 19.8 tonne/m [13,310 lb/ft].

In addition to the concern pertaining to the contact stress created between the waste package and drip shield bulkhead is the contact stress between the waste package and its supporting pallet. The interaction between the waste package and pallet is more likely to generate localized contact stresses that will exceed the allowable material limits of Alloy 22 than those associated with the waste package, and drip shield bulkhead interaction. The reason for this conclusion is the recognition that there will be at least five bulkheads transmitting static rockfall loads to the waste package, and there are only four contact points between the waste package and pallet. Moreover, the effective contact area between the waste package and pallet is expected to be quite small because the waste package will tend to deflect in a manner consistent with a simply supported beam with pivot points located on the v-notched edge of the pallet support nearest the midspan of the waste package.

There are two important factors that have not been adequately considered in the foregoing simplified waste package and drip shield interaction analysis. First, as has been demonstrated, the initial contact stresses between the waste package and drip shield bulkheads and waste package and pallet are clearly sufficient to generate large plastic deformations of Alloy 22. As a result, the initial contact area that has been assumed here can be expected to increase significantly as the outer barrier deforms under the applied load. This increase in contact area will, in turn, reduce the average contact stress acting on the waste package outer barrier and,

at some point, the deformed system will reach an equilibrium point. The critical question that needs to be answered is how much plastic strain must be incurred by the waste package outer barrier before this equilibrium point is reached. Alloy 22 is a relatively unique material because its minimum allowable elongation at failure, as defined by ASTM International (1998), is 45 percent. Most metals used for structural applications do not exhibit this much material ductility prior to failure. The log normal failure strain equivalent for Alloy 22 is 36.7 percent (Gute, et al., 2001).

Even though the high ductility of Alloy 22 may reduce the potential for a waste package breach because of interactions with the drip shield and pallet under static rockfall loads, the second important factor that has not been accounted for in the simplified analysis presented earlier is the contribution of bending moments to the stress state of the Alloy 22 in the various contact regions. These bending moments can be attributed to the overall structural response of the waste package consistent with classic engineering beam theory and localized bending moments created by localized deformations in the immediate areas of the various contact interactions. The localized bending moments will become more significant as the radial gap between the inner and outer barriers of the waste package increases as the waste package temperature decreases.

Recall that the effects of a seismic event on the effective static rockfall load acting on the drip shield is accounted for in Eq. (5-2). This adjustment to the static rockfall load enables a proper accounting of those drip shields that will buckle during a seismic event. After the drip shield has buckled, however, the same increase in the effective load must be considered when assessing the potential damage to the waste package. Assuming a static rockfall load of 76.3 tonne/m [51,290 lb/ft] is sufficient to breach the waste package by way of a buckled drip shield (as derived earlier), a peak ground acceleration of 0.91 g would increase a 40-tonne/m [26,890-lb/ft] static rockfall load to a magnitude capable of breaching the drip shield. As was pointed out in Section 5.3.1, the Total-system Performance Assessment code characterizes the magnitude of a seismic event only in terms of the peak horizontal ground acceleration, which is used in Eq. (5-2) to adjust the static rockfall load. It would be more appropriate, however, to use the peak vertical ground acceleration for this purpose. Furthermore, it was shown in Chapter 4 that 40 tonne/m [26,890 lb/ft] is the minimum static rockfall load that the drip shield is anticipated to have to support, and these loads will have fully manifested themselves within 1,000 years after cessation of maintenance of the ground support system.

Additional observations regarding the potential interaction between the waste package and drip shield include the following. First, it is not certain the base of the bulkhead or the waste package itself will be oriented consistent with the assumption the contact stress will be uniformly distributed over the bulkhead surface. The contact between the waste package and bulkhead may occur primarily along the edge of the bulkhead more consistent with a line load than a distributed load. Second, even though the Young's modulus for the Alloy 22 waste package outer barrier is approximately twice that of the Titanium Grade 24 bulkhead (see Table 5-2), the yield stress of the bulkhead {658.1 MPa [9.54×10^4 psi]} is substantially greater than the yield stress of the Alloy 22 waste package outer barrier {254.7 MPa [3.69×10^4 psi]}. As a result, the waste package outer barrier will yield much earlier than the drip shield bulkhead. After yielding, the stiffness of Alloy 22 is governed by its tangent modulus that, assuming a bilinear stress-strain curve, is approximately 2 GPa [2.9×10^5 psi], which is significantly smaller than the 107.2 GPa [15.5×10^6 psi] Young's modulus of Titanium Grade 24 that is still responding to the load in a linear elastic

manner. Therefore, the bulkhead can be considered to be a rigid body from the perspective of the waste package outer barrier. Third, the outer barrier is not attached to the inner barrier in any way. Consequently, the inner barrier acts as an anvil that the outer barrier can be cold worked against. The inner barrier protects the spent nuclear fuel or high-level waste within its confines from the effects of rockfall loads, both static and dynamic. Once the outer barrier is breached, however, the protection of the waste package contents provided by the inner barrier will degrade very quickly, relative to the repository time scale, because of its relatively high corrosion rates.

To investigate the foregoing concerns, a finite element model of the waste package and drip shield interaction under static rockfall loads is under development. This model will also include the waste package pallet support. Although this model has yet to be completed, Section 6.1 presents a brief description of the assumptions being employed in the construction of this model.

6.1 Finite Element Model Description

Sections 6.1.1 through 6.1.3 convey the rationale and technical bases for the various assumptions and boundary conditions implemented in the construction of the finite element model used to approximate the waste package and drip shield interaction under static rockfall loads.

6.1.1 Finite Element Model Geometry

The finite element model of the waste package and drip shield interaction under static rockfall loads consists of six distinct components: the fuel assemblies, basket, inner barrier, outer barrier, waste package pallet, and drip shield bulkhead. Figure 6-1 shows the layout of these components described in detail in the following discussion. The entire assembly is assumed to be under a vertical load from the drip shield bulkheads. The model geometry has been simplified by assuming symmetry conditions for both the load and geometry about the vertical plane that intersects the waste package centerline (as shown in Figure 6-1). All features and dimensions are based on documented engineering drawings (CRWMS M&O, 2000a, Reference Sketch Numbers SK–0175, Revision 02; and SK–0191, Revision 00). The model is being constructed using a mixture of plate and solid elements. Plate elements (three-dimensional quadrilaterals) are used for the basket structure. Solid elements (three-dimensional hexahedrons) are used to represent all other structural members (see Figures 6-2 through 6-5).

An effort has been made to minimize the number of nodes and elements used to discretize the model, but the level of modeling detail required to capture the contributions of geometric stress concentration factors in critical areas (e.g., the closure lid weld region) cannot be avoided if reliable results in these regions are desired. The fuel assemblies and basket are simplified to a relatively coarse mesh that provides a good representation of the mass and stiffness of these structures. The inner and outer barriers are similarly simplified only in regions away from areas of concern. Much of the cylindrical sections of the inner and outer barriers are modeled with one element through the thickness. These elements use an incompatible mode formulation that makes them accurate in modeling bending where a standard solid element would not be accurate unless three or more well-shaped elements were used through the thickness. The

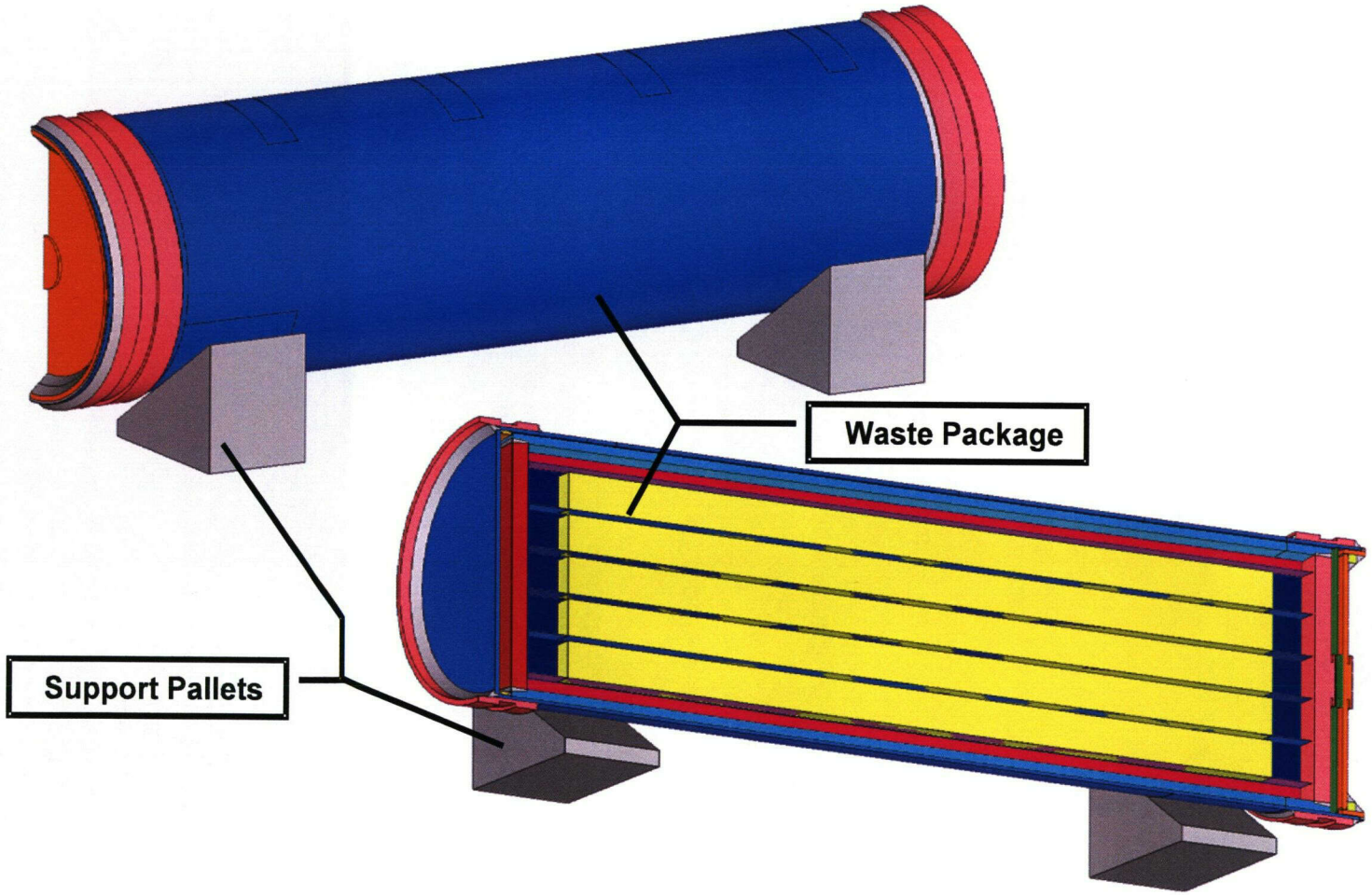

Figure 6-1. Waste Package and Drip Shield Static Rockfall Load Interaction Model

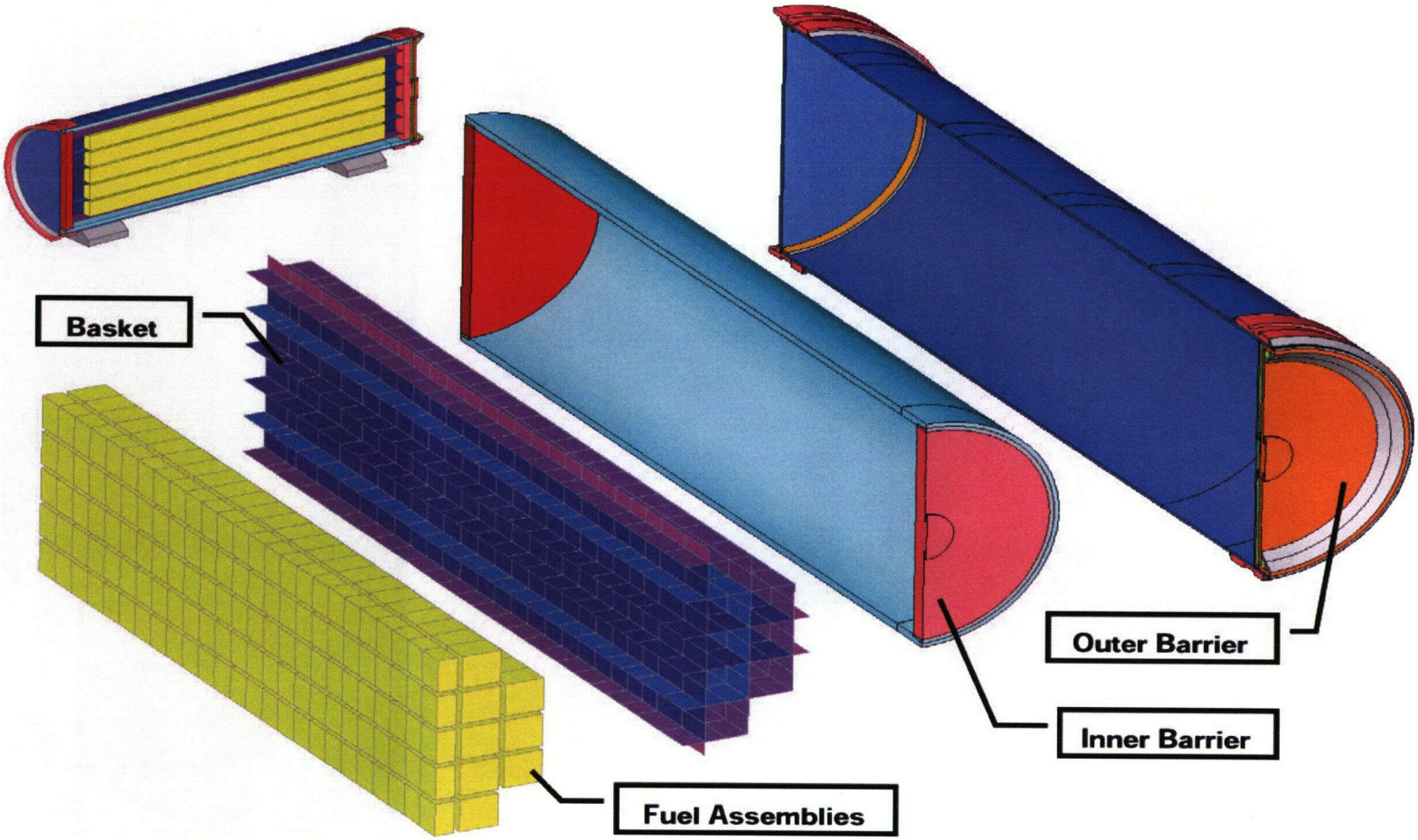

Figure 6-2. Waste Package Model Components

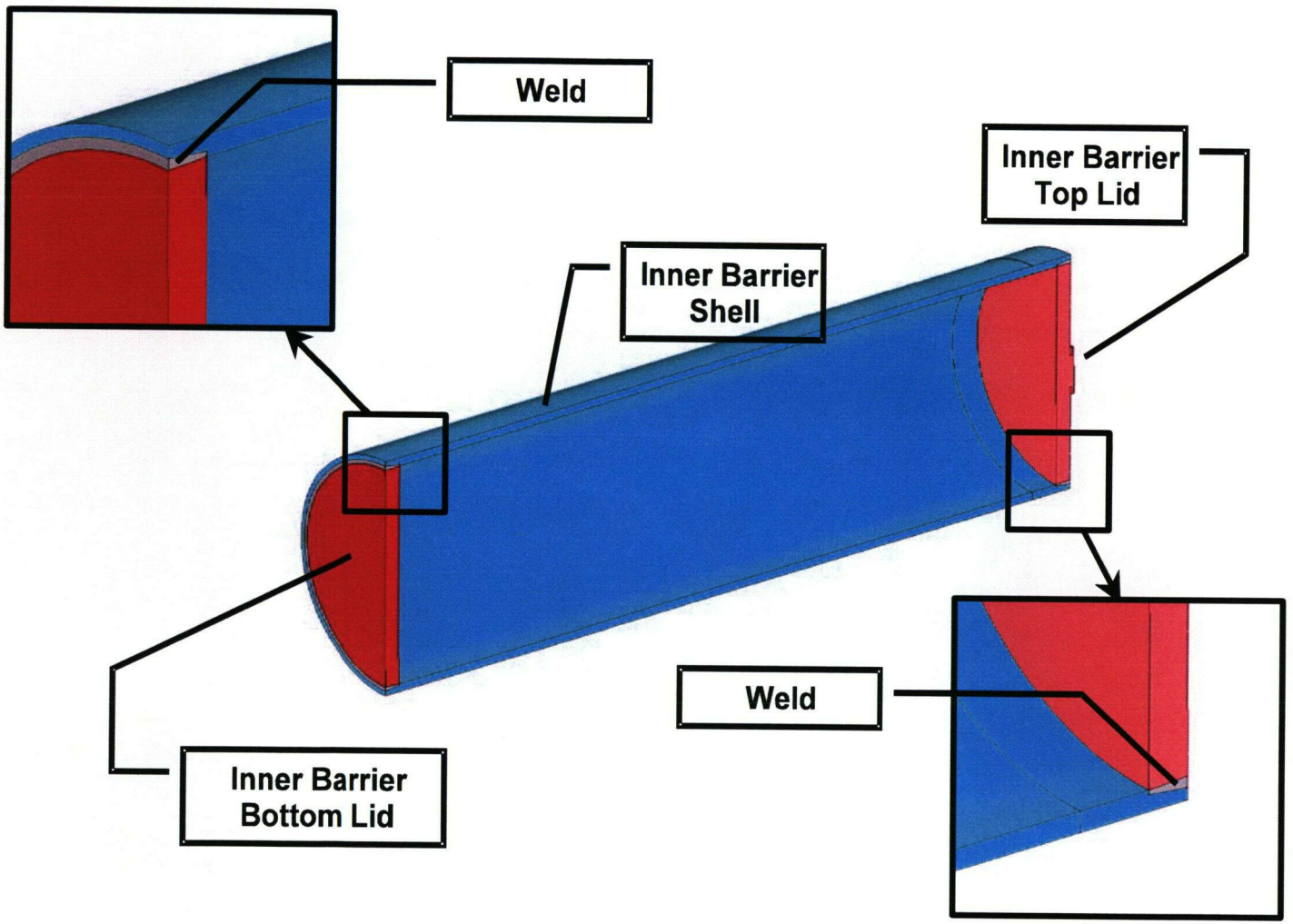

Figure 6-3. Waste Package Inner Barrier Components

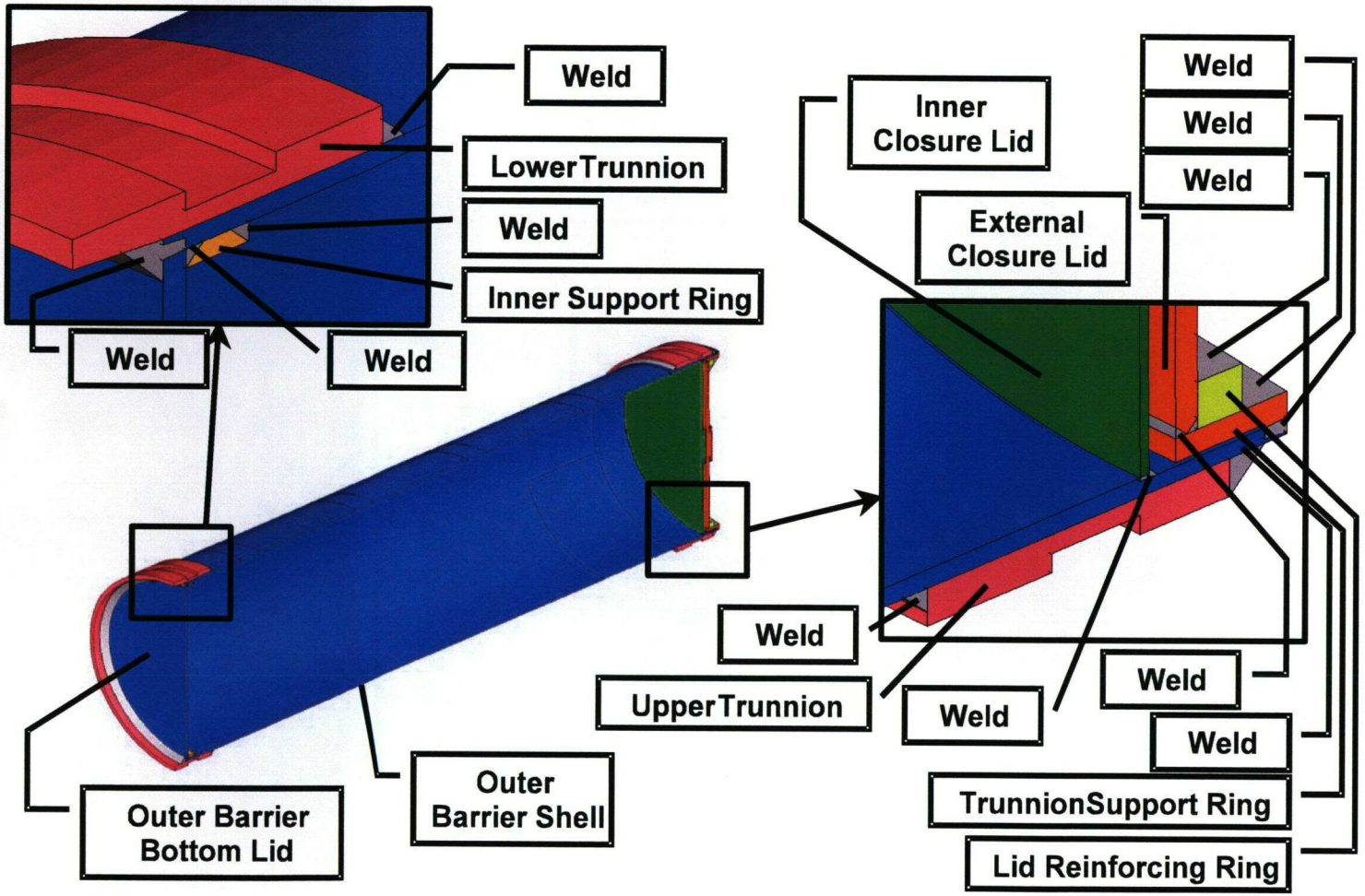

Figure 6-4. Waste Package Outer Barrier Components

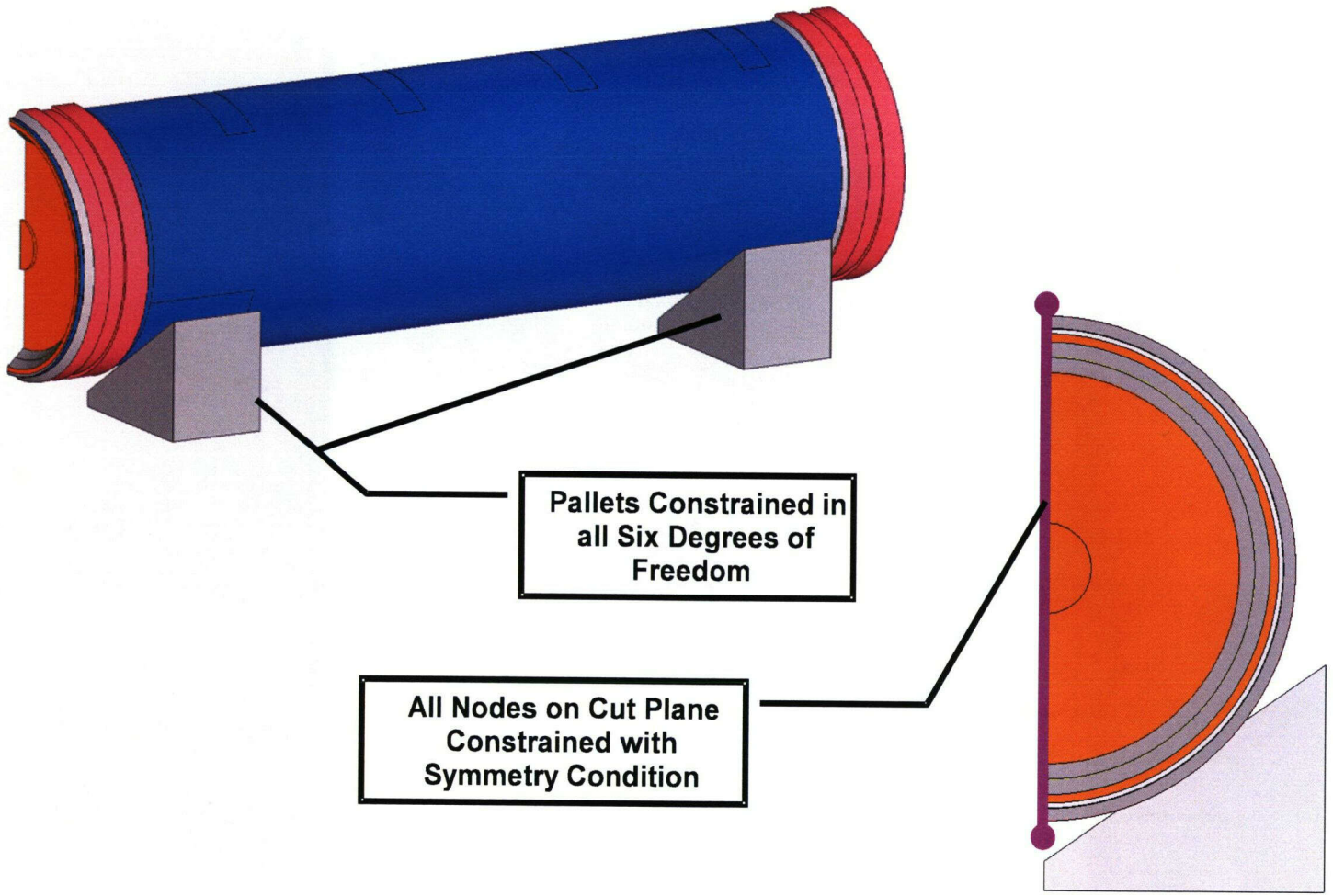

Figure 6-5. Waste Package and Drip Shield Interaction Model Boundary Conditions

cylindrical sections with the incompatible mode elements are effectively glued to the fine meshed regions of the barrier end caps using a tied contact surface interaction. The outer barrier regions in contact with the pallets and bulkhead are also finely meshed to provide good contact and stress results.

6.1.2 Finite Element Model Boundary Conditions

6.1.2.1 Loads

The only loads acting on the waste package are gravity and the static rockfall loads transferred through the drip shield bulkheads. The vertically oriented static rockfall loads are applied to the reference nodes of the rigid surfaces that represent the five drip shield bulkheads in contact with the waste package.

6.1.2.2 Kinematic Constraints

Each of the six waste package and drip shield interaction model components are free to translate and interact in reaction to the simulated load conditions. A single plane of symmetry is the only major simplifying assumption. Each component of the model interacts with its neighbor through contact surface interaction definitions. The various types of contacts are described in the following discussion.

The outer barrier rests on the two pallets with contact defined locally for each contact pair. These contact pairs define the pallet surfaces as rigid surfaces while the outer barrier surface is deformable. This assumption has been made to get a bounding estimate of the potential stresses that are generated at this interface and to reduce overall model size.

The model includes five bulkheads in contact with the waste package, each evenly spaced approximately 1 m [3.28 ft] apart along the length of the waste package. As with the pallets, the bulkhead surfaces are assumed to be rigid. As was pointed out earlier, the yield stress of the Titanium Grade 24 bulkhead is substantially greater than the yield stress of Alloy 22, and the basic cross section of the bulkhead has a relatively high area moment of inertia (i.e., the bulkhead has a relatively high geometric bending stiffness). Although a post-buckling analysis of the drip shield under accumulated static rockfall conditions was not performed, the bulkhead is not expected to sustain significant distortions of its basic shape (recall that buckling of the drip shield is controlled primarily by the column loading of the support beam). Therefore, the bulkhead has been assumed to have the same geometric dimensions that it had before it was subjected to any loads.

The inner diameter of the outer barrier can interact with the outer diameter of the inner barrier along the entire length of the waste package. These surfaces are modeled using standard contact definitions for two deformable bodies.

The basket is spot welded to the inner diameter of the inner barrier. The finite element model simply ties the coarse basket mesh to the inner barrier elements by equivalencing the nodes of the two components that are collocated (see Figure 6-2).

Each of the fuel assemblies has three contact interaction definitions with the basket (i.e., the bottom and sides of each basket cell). These surface interactions are modeled using standard contact definitions for two deformable bodies.

Finally, tied contacts are used at several locations to provide a transition between regions of coarse and fine mesh discretizations.

6.2 Summary of Analysis Results

This work has yet to be completed.

6.3 Data Abstraction for MECHFAIL

This work has yet to be completed.

7 DRIP SHIELD AND DYNAMIC ROCK BLOCK IMPACT PERFORMANCE ANALYSES

The U.S. Department of Energy (DOE) is designing the drip shield so it will protect the waste package from direct rock block impacts. This chapter conveys the results obtained from a parametric study that assesses the effects of rock block size and fall height on the ability of the drip shield to mitigate damage to the waste package. The results of this parametric study have been used to develop the abstractions implemented within the MECHFAIL Total-system Performance Assessment Version 5.0 beta code module. Specific abstractions developed include the maximum displacement of the drip shield and the plastic strain incurred by the different drip shield components for a given dynamic rock block impact scenario (i.e., rock block size and fall height). In addition, an abstraction that can be used to approximate the drip shield velocity as a function of displacement for a given rock block impact scenario has also been derived. The drip shield velocity-displacement relationship is needed to estimate the potential impact velocity of the drip shield with different waste package sizes in the event the rock block impact scenario is sufficient to cause this type of interaction.

7.1 Finite Element Model Description

The finite element models used to assess the effects of dynamic rock block impacts on the drip shield are consistent with those described in detail in Gute, et al. (2001). As a result, only a brief overview of the finite element models will be presented here.

7.1.1 Drip Shield Finite Element Model

The drip shield and rock block impact finite element model was constructed using two planes of symmetry and plane strain boundary conditions (see Figure 7-1). Note that these boundary conditions are consistent with those used to model the drip shield subjected to static rockfall loads (see Chapter 5) except for the presence of rock rubble along the sides of the drip shield. Rock rubble was not included in the drip shield and rock block impact model because the primary focus of the parametric study was to evaluate the effects of varying rock block sizes and rock block impact velocities (i.e., fall heights) on drip shield performance. If it is determined that dynamic rock block impacts with the drip shield are risk significant, additional analyses can be performed to study the potential beneficial and adverse effects associated with the presence of rock rubble buttressing the drip shield. It is expected that including the presence of rock rubble will reduce the deflection of the drip shield while increasing the likelihood of the Titanium Grade 7 plate being breached for a given rock block impact.

The potential interactions between the drip shield and waste package created by a rock block impact have yet to be evaluated. This study was limited to establishing the possibility of such an occurrence before spending the significant effort that will be required to develop a model that can simulate the event.

Unlike the drip shield and static rockfall load models, the drip shield and dynamic rock block impact models were constructed using eight-noded hexahedral solid elements exclusively. This was necessitated by the use of an explicit, as opposed to an implicit, method of numerical solution to perform the analyses. As a result, reduced integration and hourglassing issues uniquely associated with the explicit numerical technique needed to be taken into consideration.

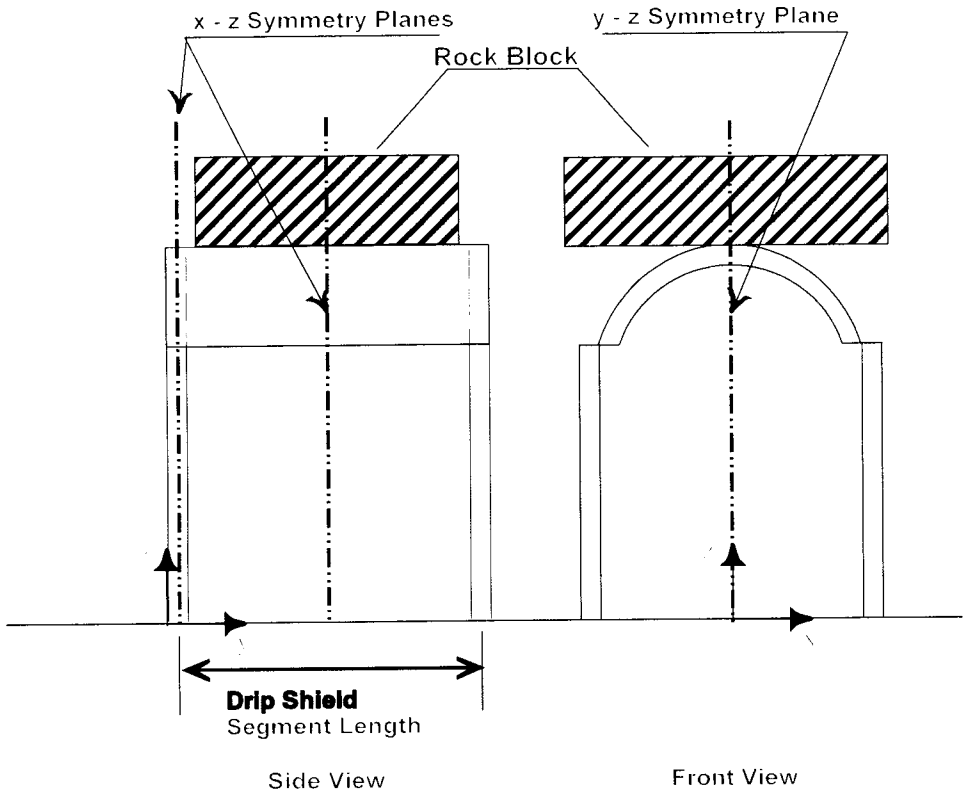

Figure 7-1. Schematic Illustrating the Planes of Symmetry Used to Simplify the Drip Shield and Rock Block Impact Model

Hourglassing occurs because reduced-integration elements consider only the linearly varying part of the incremental displacement field in the element for the calculation of the increment of physical strain. The remaining part of the nodal incremental displacement field is the hourglass field and can be expressed as hourglass modes. Excitation of these modes may lead to severe mesh distortion, with no stresses resisting the deformation. Hourglassing can be avoided by using an adequate mesh density within the model or by introducing artificial numerical damping to suppress the hourglass modes. Because the inappropriate implementation of artificial numerical damping may result in an excessively stiff response by the structure, it was decided that the problem of hourglassing would be addressed by using an adequately refined mesh.

7.1.2 Finite Element Model of the Rock Block

It is generally accepted that the rock block will dissipate some of the energy associated with the impact with the drip shield by localized crushing or fracturing. The amount of energy dissipated through this mechanism is uncertain. Predominant factors that affect the quantity of energy dissipated in this fashion are the magnitude and distribution of stress within the rock block,

which are directly dependent on the geometry of the rock block and the ability of the rock block material to support these stresses without failing (i.e., crushing or fracturing). As presented in earlier progress reports (Gute, et al., 2000, 2001), the rock block has been assumed to have cubic, spherical, or tetrahedron geometries. Moreover, the previous constitutive models for the rock block were either based on the classical metal plasticity model with a von Mises yield surface and perfectly plastic flow rule or the Mohr-Coulomb model cast in terms of the Drucker-Prager yield surface formulation. It is not clear at this time, however, if the development of a rock block finite element model that can reasonably approximate the energy dissipated by crushing or fracturing during the impact event is wholly necessary. Maintaining a constant rock block mass with an infinite material strength during the impact event will, conceptually, provide conservative results because the energy dissipated by crushing or fracturing will not be accounted for. The structural stiffness of the drip shield bulkheads and support beams is, however, likely to be sufficient to cause localized failure of the rock block. This localized failure of the rock block was explicitly accounted for in the construction of the finite element model so the localized shearing of the drip shield plate near the bulkhead would not be underestimated. To accomplish this task, the plane strain boundary conditions were not applied to the face of the rock block whose outward normal is in the negative y-direction (see Figures 7-2a and 7-2b). No other provisions for rock block material or structural failure were taken into consideration within the model (i.e., a simple linear elastic constitutive model was used to represent the mechanical behavior of the rock block mass).

Moreover, the finite element model of the rock block was constructed using the following simplifying assumptions: (i) the rock block is a parallel-piped shape; (ii) the rock block impacts the apex of the drip shield crown with only a vertical component of velocity, and (iii) the rock block is sufficiently long to assume plane strain conditions. Assumption (iii) implies the rock block size should be interpreted as a mass-per-drip-shield segment length. For this study, the drip shield segment length was defined as the distance between two planes bisecting consecutive bulkhead and support beam structural stiffener pairs. The actual drip shield segment length is approximately 1.15 m [3.77 ft].

7.1.3 Finite Element Model Boundary Conditions

7.1.3.1 Loads

A comprehensive discussion of the derivation of the dynamic rock block impact load conditions can be found in Gute, et al. (2001). Table 7-1 summarizes the rock block sizes and impact velocities that were simulated in the parametric study. The combinations of rock block sizes and impact velocities were chosen in the hope of developing simple relationships between the drip shield response and the kinetic energy of the impacting rock block. As the results presented in Sections 7.2 and 7.3 indicate, however, these relationships could not be based on kinetic energy alone. Note that different impact velocities are analogous to different rock block fall heights and are related in Eq. (7-1).

$$v_{rock} = \sqrt{2\,g\,h_{i+1}} \tag{7-1}$$

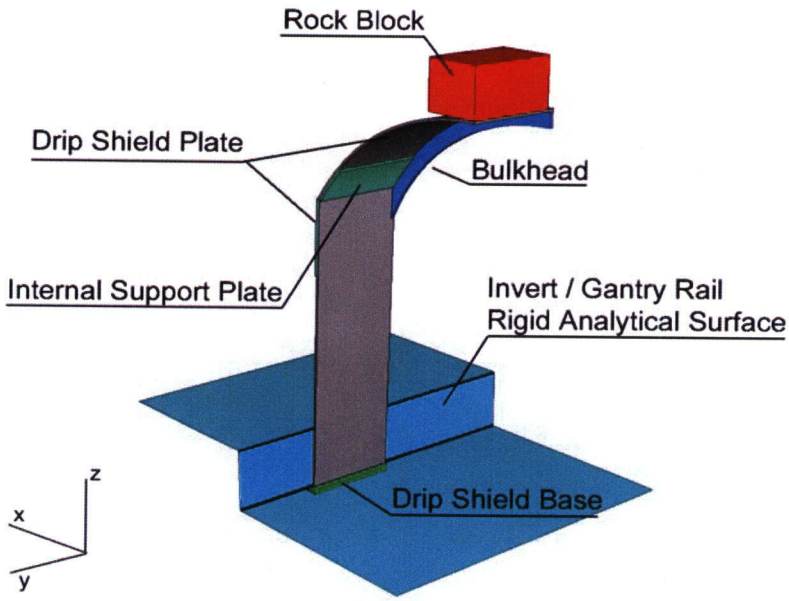

Figure 7-2(a). Drip Shield and Rock Block Impact Finite Element Model

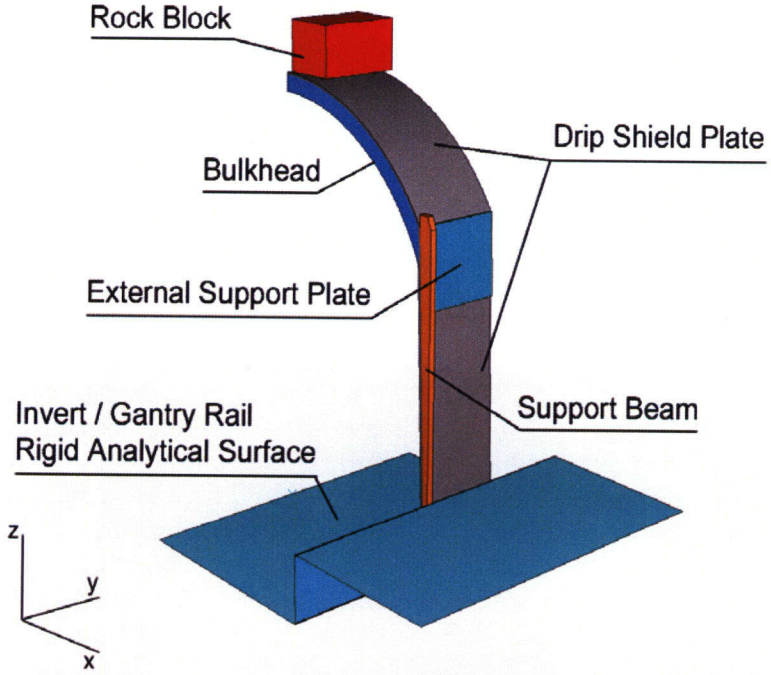

Figure 7-2(b). Drip Shield and Rock Block Impact Finite Element Model

Table 7-1. Drip Shield and Rock Block Impact Scenarios Included in the Parametric Study			
Case	Initial Rock Block Impact Velocity, m/s [ft/s]	Rock Block Mass, tonne/m [lb/ft]	Rock Block Impact Kinetic Energy, Joules/m [(ft-lb)/ft]
1	7.0 [23.0]	0.5 [336]	12,250 [2,754]
2	9.9 [32.5]	0.5 [336]	24,500 [5,508]
3	14.0 [45.9]	0.5 [336]	49,000 [11,016]
4	7.0 [23.0]	1.0 [672]	24,500 [5,508]
5	9.9 [32.5]	1.0 [672]	49,000 [11,016]
6	14.0 [45.9]	1.0 [672]	98,000 [22,031]
7	7.0 [23.0]	2.0 [1,344]	49,000 [11,016]
8	9.9 [32.5]	2.0 [1,344]	98,000 [22,031]
9	14.0 [45.9]	2.0 [1,344]	196,000 [44,062]
10	7.0 [23.0]	4.0 [2,689]	98,000 [22,031]
11	9.9 [32.5]	4.0 [2,689]	196,000 [44,062]
12	2.475 [8.12]	4.0 [2,689]	12,250 [2,754]
13	7.0 [23.0]	8.0 [5,378]	196,000 [44,062]
14	1.750 [5.74]	8.0 [5,378]	12,250 [2,754]
15	2.475 [8.12]	8.0 [5,378]	24,500 [5,508]

where

v_{rock} — impact velocity of the rock block (m/s)

g — acceleration due to gravity (m/s^2)

h_{i+1} — rock block fall height (m) (corresponds to the drift degradation zone failure height at the time the seismic event occurs).

To account for the ground motion associated with the seismic event assumed to be occurring at the same time as the dynamic rock block impact with the drip shield, the drip shield and invert were assumed to be moving at a constant upward velocity of 1 m/s [3.28 ft/s] at the time the impact was initiated. After impact, the invert foundation continued to move upward with a 1-m/s [3.28-ft/s] velocity throughout the duration of the analysis while the drip shield was free to respond to the rock block impact load.

7.1.3.2 Kinematic Constraints

Kinematic constraints are discussed in detail in Gute, et al. (2001) and are illustrated in Figure 7-1. To summarize, the drip shield rock block impact model is simplified by cutting the model by three symmetry planes [see Figures 7-2(a), (b)]. The first two planes are normal to the length axis (y-direction) and cut through the middle of the bulkhead and between the bulkheads. The second plane is normal to the lateral axis (x-direction) and cuts through the center of the drip shield. Nodes that lie on the respective symmetry planes are constrained to those planes. The resultant model represents a continuous drip shield that experiences the rock block impact along its entire length.

Recall from the rock block model discussion in Section 7.1.2 that the rock block was assumed to be fractured at the bulkhead. This assumption will create the shearing condition between the drip shield bulkhead and the drip shield crown plate that was expected to occur after the rock block was crushed or fractured above the bulkhead. The shear stress calculated in the model should bound any potential shear stress that the drip shield may experience as the result of a rock block impact.

Three different contact interactions were explicitly accounted for in the drip shield and rock block impact model. These were the interactions between the drip shield and the (i) rock block, (ii) supporting invert, and (iii) adjacent gantry rail. A master-slave concept was used within the finite element program to model these interactions. Specifically, the nodes associated with the slave surface cannot penetrate into or through the master surface mesh. The master surface nodes, however, can penetrate through the slave surface. As a consequence, the slave surface mesh should be much more refined than the master surface. Another option was to redundantly define the master-slave relationship—the contact surface pair is defined twice with the surfaces interchanging the master-slave relationship. A redundant master-slave relationship does not allow any nodes from either surface to penetrate through the counterpart surface. Moreover, a redundant master-slave contact definition is only appropriate when the master and slave surfaces have similar mesh densities. Even though the effects of friction can be included as part of the interaction between the two surfaces, the duration and magnitude of the impact load are such that these effects are negligible.

For the case of the drip shield and rock block interaction, the coarsely meshed rock block was used to define the master surface, and the drip shield was the corresponding slave surface. No redundancy was used.

The finite element model also represented the drip shield as a free-standing structure on the invert. In particular, the model employed a friction-free sliding contact boundary condition between the drip shield and the rigid analytical surface to represent the invert and gantry rails (see Figure 7-2). Note that the gantry rail (i.e., the vertical side of the rigid analytical surface) limited the horizontal (x-direction) deflections of the drip shield and provided a potential pivot point to cause the drip shield to fold up underneath itself (i.e., buckle) if the deformations became sufficiently large.

7.1.4 Finite Element Model Material Properties

See Section 5.1.3 for a summary of the material properties used to develop the constitutive models for the various drip shield components. Gute, et al. (2001) discusses in detail the construction of the bilinear stress-strain curves used to define the elastic-plastic material behavior of the drip shield materials. The specific elastic rock mass material properties used in the drip shield and rock block impact finite element analyses are provided in Table 7-2 (NRC, 2000).

Table 7-2. Elastic Material Properties Used for the Rock Block Mass

Young's Modulus,* GPa [psi]	Poisson's Ratio*	Density,* tonne/m^3 [lb/in^3]
32.6 [4.73 × 10^6]	0.21	2.7 [0.098]

*NRC. "Input to Repository Design and Thermal-Mechanical Effects Issue Resolution Status Report." Revision 3. Washington, DC: NRC. 2000.

7.2 Summary of Analysis Results

A comprehensive discussion of the general stress and deflection results obtained from the finite element models of the drip shield and rock block impacts can be found in Gute, et al. (2001). That discussion is not repeated here except where it relates directly to the data abstractions presented in Section 7.3.

7.2.1 Drip Shield Deflection

Knowledge of the maximum deflection of the drip shield was required to determine if the drip shield would sufficiently deform under the rock block impact load to strike the waste package. Drip shield deflection was measured by the relative change in gap between the bottom surface of the bulkhead at the apex of the drip shield crown and the top of the waste package. Figures 7-3 through 7-7 show the drip shield deflection history for each load case from Table 7-1.

7.2.2 Drip Shield Component Stresses and Strains

The magnitudes of stress and strain incurred by the drip shield components under dynamic rock block impact loads are required to establish the extent of the damage incurred by the drip shield as a result of this type of event. Figure 7-8 illustrates the regions where maximum stresses and strains occurred within the drip shield plate and bulkhead as the result of dynamic rock block impacts. Table 7-3 provides a summary of the maximum drip shield deflection, drip shield plate and bulkhead von Mises stresses, and drip shield plate and bulkhead equivalent plastic strains and the maximum deflections that were calculated for each load case.

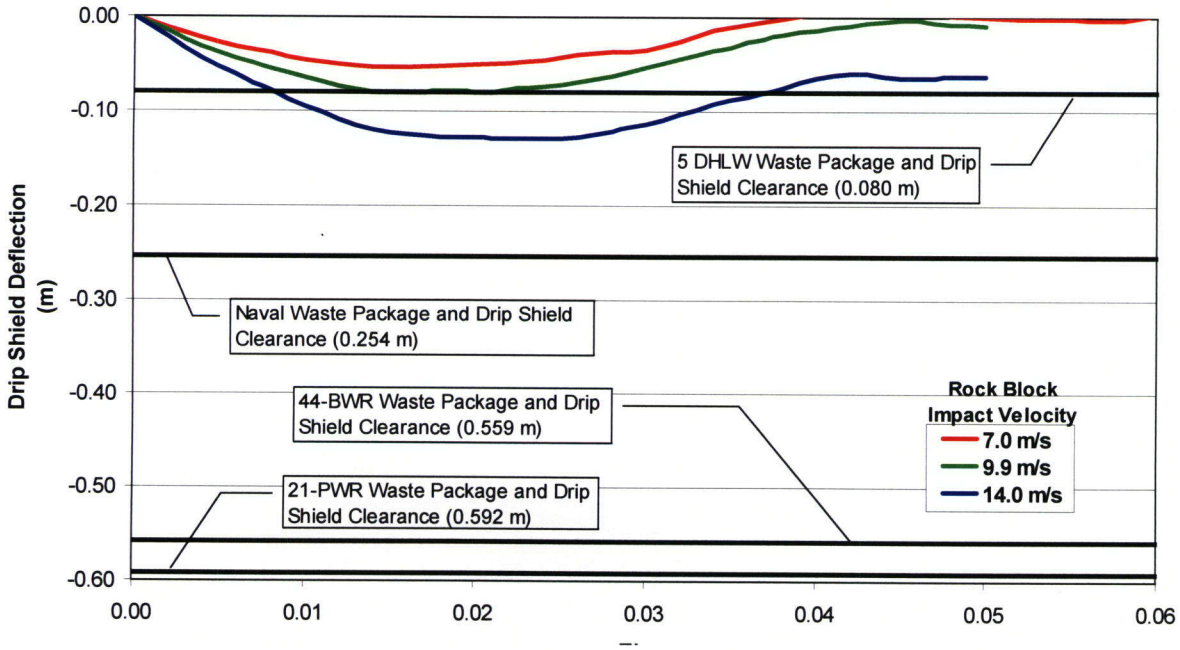

Figure 7-3. Drip Shield Deflection Versus Time for 0.5 tonne/m [336 lb/ft] Rock Block Impacts

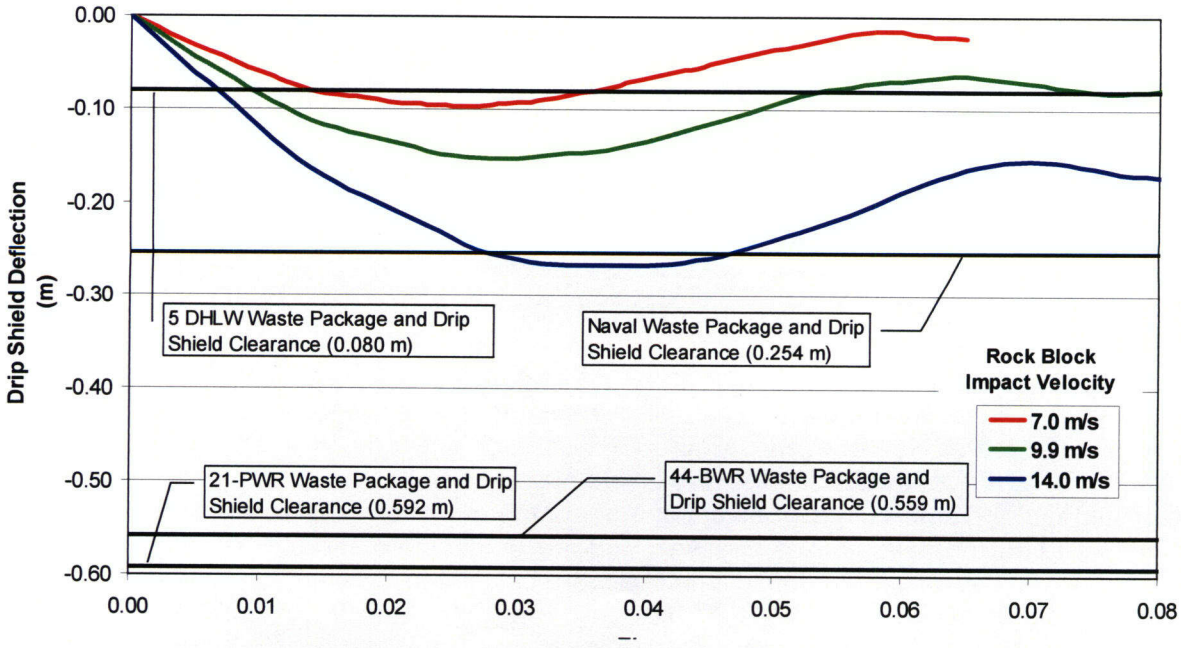

Figure 7-4. Drip Shield Deflection Versus Time for Varying 1.0 tonne/m [672 lb/ft] Rock Block Impacts

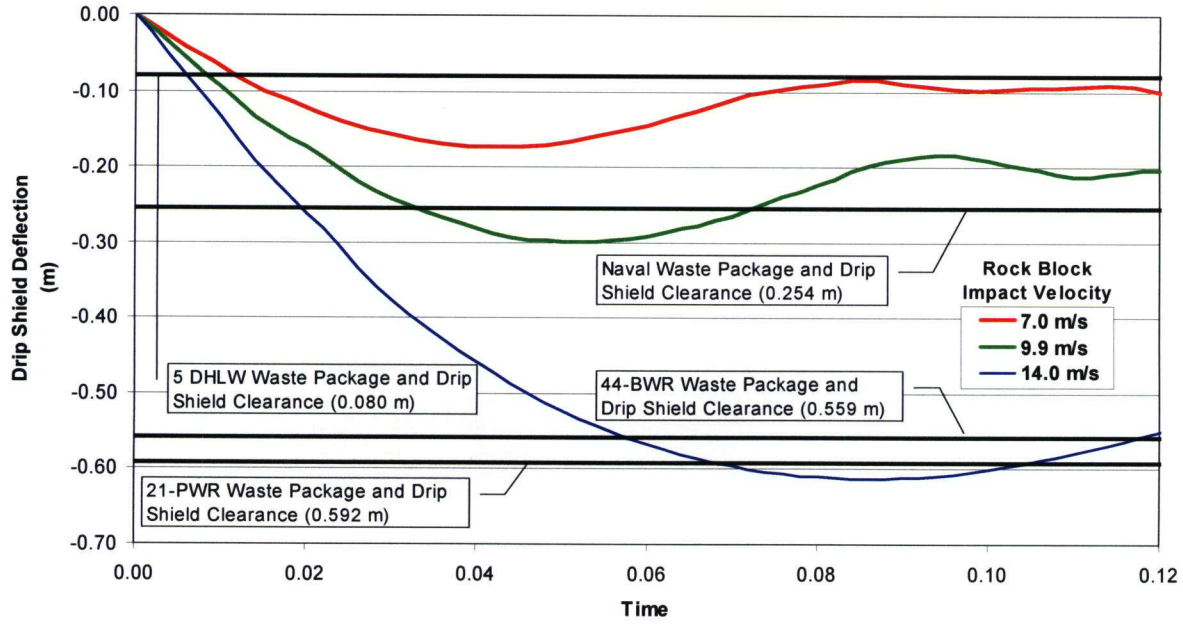

Figure 7-5. Drip Shield Deflection Versus Time for Varying 2.0 tonne/m [1,344 lb/ft] Rock Block Impacts

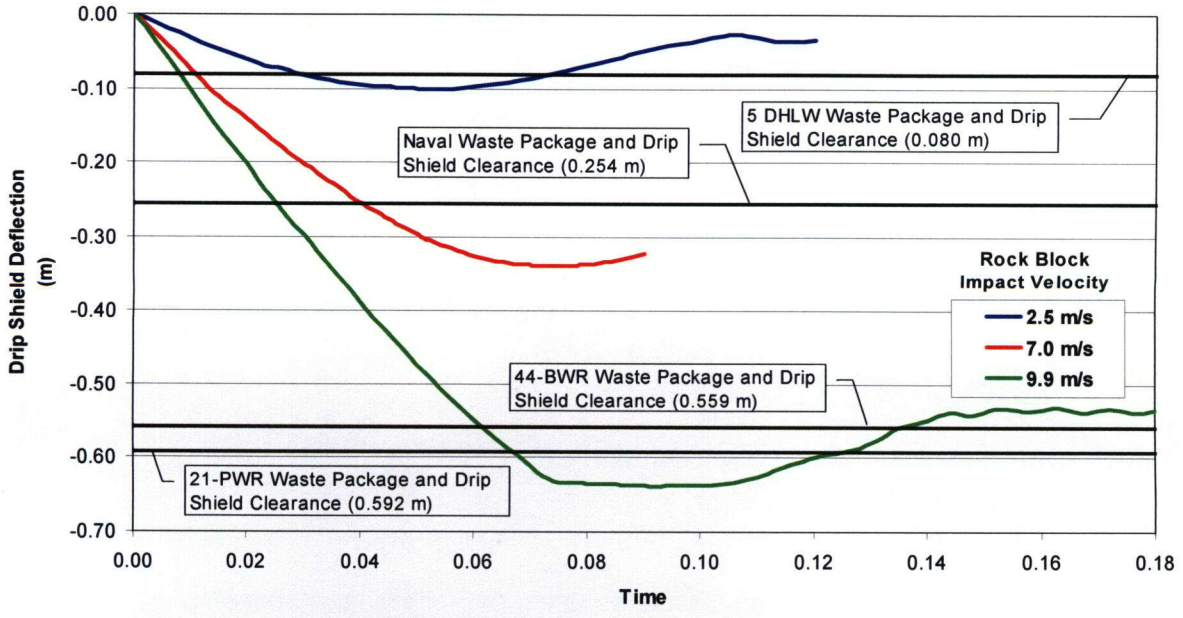

Figure 7-6. Drip Shield Deflection Versus Time for Varying Velocity 4.0 tonne/m [2,689 lb/ft] Rock Block Impacts

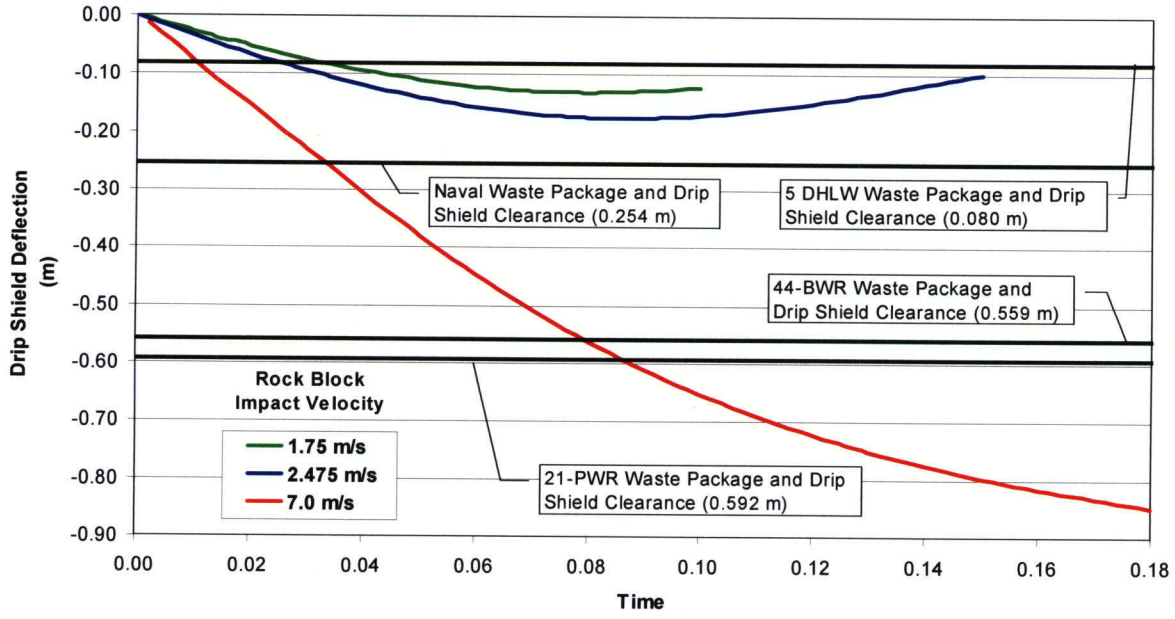

Figure 7-7. Drip Shield Deflection Versus Time for Varying Velocity 8.0 tonne/m [5,378 lb/ft] Rock Block Impacts

7.3 Data Abstractions for MECHFAIL

7.3.1 Drip Shield Maximum Deflection Abstraction

The maximum deflection of the drip shield caused by a given rock block impact scenario was assumed to be a function of the rock mass as well as the momentum and kinetic energy of the rock block [see Eq. (7-2)]. The coefficients for Eq. (7-2) were determined using the data obtained from the finite element analyses and the method of Least Squares curve fitting,

$$\delta_{max} \cong \left[7.720 \times 10^{-3}\right] M + \left[3.402 \times 10^{-3}\right] M^2 - \left[3.544 \times 10^{-4}\right] M^3 + \left[1.041 \times 10^{-4}\right] M\, v_{rock} + \left[1.443 \times 10^{-3}\right] M\, v_{rock}^2 \quad (7\text{-}2)$$

where

δ_{max} — maximum drip shield displacement (m)
M — rock block mass (tonne/m)
v_{rock} — rock block impact velocity (m/s)

The normalized error for Eq. (7-2) was calculated using the following relationship

$$\delta_{max}^{err} = \frac{\sum\left[\delta_{max,i} - \delta_{max}\left(M_i, v_{rock,i}\right)\right]^2}{\sum\left[\delta_{max,i}\right]^2} \quad (7\text{-}3)$$

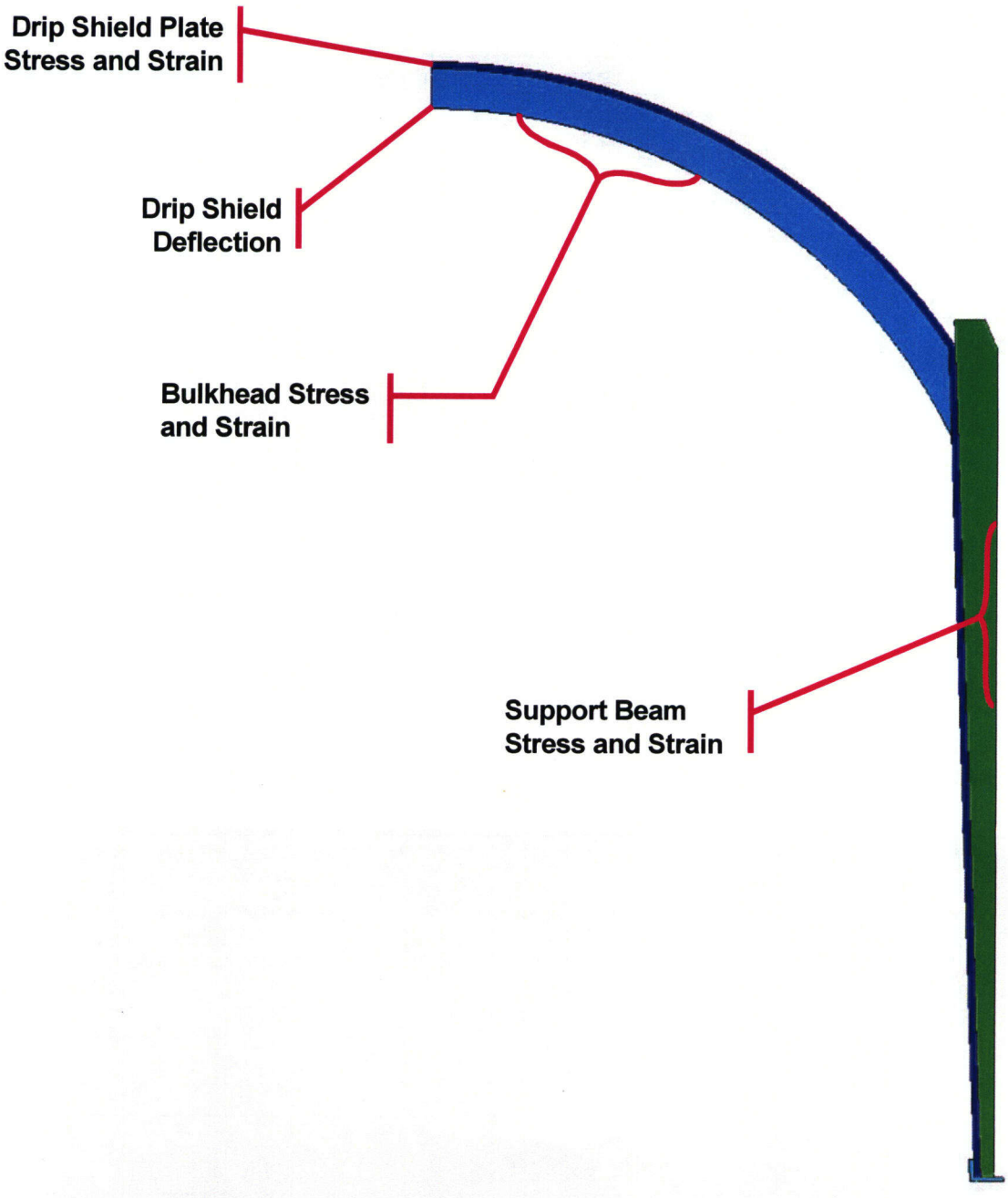

Figure 7-8. General Locations of the Maximum Drip Shield von Mises Stress and Equivalent Plastic Strains

Table 7-3. Maximum Drip Shield Plate and Bulkhead Stress and Strain Results					
		Drip Shield Plate		Drip Shield Bulkhead	
Case	Maximum Drip Shield Deflection, m [ft]	Maximum von Mises Stress, MPa [psi]	Maximum Equivalent Plastic Strain	Maximum von Mises Stress, MPa [psi]	Maximum Equivalent Plastic Strain
1	0.054 [0.177]	176.7 [2.563×10^4]	0.004	668.2 [9.691×10^4]	0.006
2	0.080 [0.262]	178.1 [2.583×10^4]	0.007	685.4 [9.941×10^4]	0.015
3	0.130 [0.426]	182.2 [2.643×10^4]	0.012	724.6 [1.051×10^5]	0.035
4	0.097 [0.318]	212.3 [3.079×10^4]	0.054	705.8 [1.024×10^5]	0.025
5	0.153 [0.502]	238.0 [3.452×10^4]	0.093	737.9 [1.070×10^5]	0.047
6	0.268 [0.879]	287.4 [4.168×10^4]	0.162	811.9 [1.178×10^5]	0.082
7	0.174 [0.571]	260.1 [3.772×10^4]	0.124	763.2 [1.107×10^5]	0.057
8	0.298 [0.977]	*	*	*	*
9	0.613 [2.011]	*	*	*	*
10	0.338 [1.109]	*	*	*	*
11	0.638 [2,093]	*	*	*	*
12	0.101 [0.331]	207.0 [3.002×10^4]	0.047	720.6 [1.045×10^5]	0.034
13	*	*	*	*	0
14	0.130 [0.426]	227.4 [3.298×10^4]	0.076	741.2 [1.075×10^5]	0.044
15	0.175 [0.574]	270.8 [3.928×10^4]	0.138	772.6 [1.121×10^5]	0.059

*Denotes results that exceeded the material failure criterion and, as a result, were not used to calculate the coefficients of the abstraction formulas.

Using Eq. (7-3), the normalized error for Eq. (7-2) was determined to be

$$\delta_{max}^{err} = 1.77 \times 10^{-3} \tag{7-4}$$

Eq. (7-2) provides a reasonable approximation of the drip shield maximum deflection, δ_{max}, for a limited range of masses, 0.5 [336] $\leq M \leq$ 8.0 tonne/m [5,378 lb/ft], and impact velocities, 1.75 [5.74] $\leq v_{rock} \leq$ 14.0 m/s [45.92 ft/s] (see Figure 7-9). Case 13 from Table 7-1 was not included in the calculation of the coefficients for Eq. (7-2) because no maximum deflection was reached in the finite element analysis. Figure 7-7 clearly shows the drip shield was far from reaching its maximum deflection when the simulation was terminated for this case. In fact, the drip shield appears to be buckling for this particular rock block impact scenario. Figure 7-9 also indicates the drip shield deflection required to cause impacts with some of the different waste package types. A comparison between the abstraction calculation and the finite element data shows that the greatest percentage error occurs in the regime of what can be characterized as low-energy impacts. The magnitude of absolute error, however, shows an excellent correlation to the analysis data. It needs to be emphasized that Eq. (7-2) is only valid within the prescribed data ranges for the rock block mass and impact velocity. This restriction is required because many abstractions use higher order polynomial terms, which will tend to dominate the expression when applied outside the given range.

7.3.2 Drip Shield Displacement and Velocity Relationship Abstraction

The drip shield velocity-displacement relationship was needed to estimate the impact velocity of the drip shield with different waste package sizes in the event the rock block impact scenario was sufficient to cause this type of interaction. The results of Gute, et al. (2001) showed the regions of plastic strain in the drip shield were relatively small, which indicated a limited amount of rock block energy was absorbed by permanent deformation of the drip shield components. This behavior was true for all cases except Case 13, which did not achieve maximum deflection and appears to be buckling. The remaining cases indicated that at maximum drip shield deflection (where velocity of the rock block was zero) the drip shield absorbed the rock block's kinetic and potential energy primarily through elastic deformation. Figures 7-3 through 7-7 support this observation because drip shield deflection versus time follows a generally sinusoidal shape, which is analogous to a simple linear spring and mass system response under similar loading conditions. Therefore, it is assumed that the drip shield and rock block interaction is linear elastic through the point of maximum deflection.

The velocity of the rock block and drip shield crown when it impacts the waste package can be approximated using Eq. (7-5). The data points in Figure 7-10 are normalized for each scenario such that velocity and deflection have a range of zero to one. Equation (7-5) is also normalized and plotted for comparison. This data abstraction provides a bounding solution to the simulation data.

$$v = (v_{rock} = 1)\left[1 - \left(\frac{C}{d_{max}}\right)^2\right]^{1/2} \tag{7-5}$$

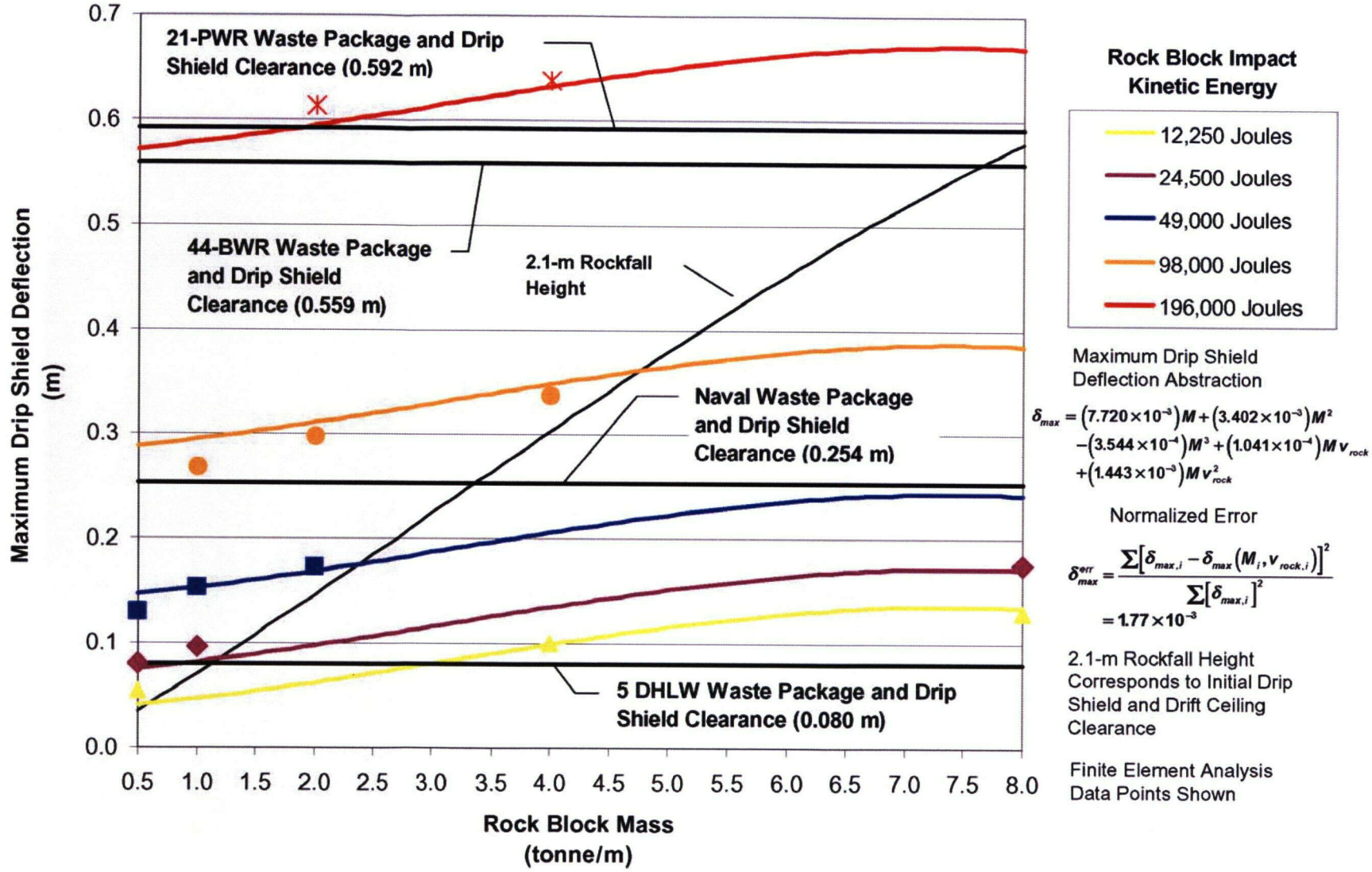

Figure 7-9. Maximum Drip Shield Deflection Abstraction for Rock Block Impacts

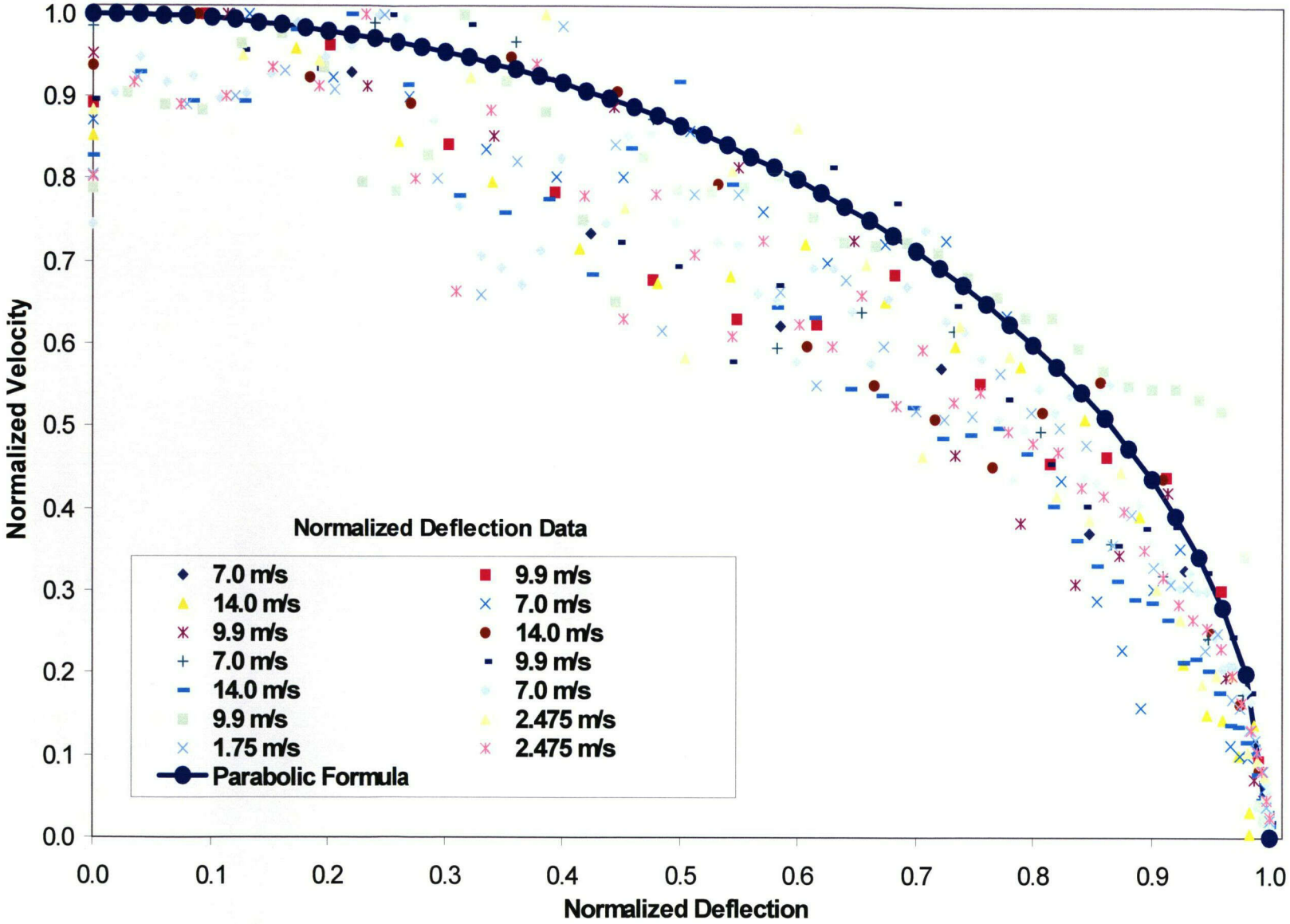

Figure 7-10. Drip Shield Velocity as a Function of Displacement Caused by Rock Block Impacts

where

v — drip shield velocity when impacting the waste package (m/s)
v_{rock} — initial rock block impact velocity (m/s)
C — clearance between the drip shield and waste package prior to the impact event (m), $C < \delta_{max}$
δ_{max} — maximum deflection of the drip shield if allowed to deform freely (m).

7.3.3 Drip Shield Component Stress and Plastic Strain Abstractions

The abstractions for the maximum stresses and plastic strains for the drip shield plate and bulkhead under dynamic rock block impact conditions were derived using the data summarized in Table 7-3. No abstractions were developed for the support beam because its response to the rock block impact loads was predominantly linear (i.e., the calculated stresses were well below the yield stress threshold). This observation was not valid for Case 13, however, where the dynamic rock block load was sufficient to cause buckling of the drip shield. This result demonstrates that rock blocks of 8 tonne/m [5,378 lb/ft] are sufficient to drive the drip shield into the waste package regardless of the initial clearance between them. The 7-m/s [23.0-ft/s] rock block impact velocity corresponds to a rockfall of 2.1 m [6.89 ft], which is the clearance between the drip shield crown and drift ceiling before any drift degradation occurs. Equations (7-6) through (7-9) are the abstractions that can be used to estimate the maximum stresses and plastic strains for the drip shield plate and bulkhead components in terms of the rock block mass and impact velocity.

It is important to recognize, however, that these abstractions are only valid if the drip shield does not interact with the waste package.

$$\sigma_{plate} = \left(1.371 \times 10^{2}\right) - \left(5.889 \times 10^{0}\right) M + \left(9.255 \times 10^{0}\right) M v_{rock} + \left(8.683 \times 10^{-2}\right) M v_{rock}^{2} \quad (7\text{-}6)$$

$$\sigma_{bulkhead} = \left(6.419 \times 10^{2}\right) + \left(3.052 \times 10^{0}\right) M + \left(4.366 \times 10^{0}\right) M v_{rock} + \left(5.306 \times 10^{-1}\right) M v_{rock}^{2} \quad (7\text{-}7)$$

$$\varepsilon_{plate} = -\left(5.229 \times 10^{-2}\right) - \left(8.765 \times 10^{-3}\right) M + \left(1.338 \times 10^{-2}\right) M v_{rock} + \left(1.156 \times 10^{-4}\right) M v_{rock}^{2} \quad (7\text{-}8)$$

$$\varepsilon_{bulkhead} = -\left(7.877 \times 10^{-3}\right) + \left(1.195 \times 10^{-3}\right) M + \left(2.447 \times 10^{-3}\right) M v_{rock} + \left(2.766 \times 10^{-4}\right) M v_{rock}^{2} \quad (7\text{-}9)$$

where

σ_{plate} — maximum von Mises stress for the drip shield plate (MPa)
$\sigma_{bulkhead}$ — maximum von Mises stress for the drip shield bulkhead (MPa)
ε_{plate} — maximum equivalent plastic strain for the drip shield plate (m/m)
$\varepsilon_{bulkhead}$ — maximum equivalent plastic strain for the drip shield bulkhead (m/m)

Using the normalized error relationship defined in Eq. (7-3), the normalized error for the drip shield component von Mises stress and equivalent plastic strain abstractions were determined to be

$$\sigma_{plate}^{err} = 2.15 \times 10^{-3}$$

$$\sigma_{bulkhead}^{err} = 4.10 \times 10^{-5}$$

$$\varepsilon_{plate}^{err} = 2.74 \times 10^{-2}$$

$$\varepsilon_{bulkhead}^{err} = 3.78 \times 10^{-3}$$

The results from Cases 8, 9, 10, 11, and 13 were not included in the derivation of Eqs. (7-6) through (7-9). These cases were excluded because the maximum von Mises stress exceeded the failure stress (i.e., ultimate tensile strength) for these particular scenarios. Once the failure stress of a material exceeded, the material behaves as an elastic-perfectly plastic material (i.e., the material loses the ability to carry any additional stress while accumulating additional plastic strain). This change in material behavior introduced a severe discontinuity in the calculated stress and strain values. The accuracy of the abstractions for those loading conditions that did not cause the drip shield component materials to exceed the failure criteria would be adversely affected if the results from Cases 8, 9, 10, 11, and 13 were included in the derivation of Eqs. (7-6) through (7-9). Furthermore, attempting to capture post-failure stress and strain behavior of the drip shield component materials does not serve any practical engineering purpose.

Figures 7-11 through 7-14 illustrate how well the drip shield plate and bulkhead abstractions for the maximum von Mises stress and plastic strain correlate with the results obtained from the finite element models. These figures also convey the relationship of the abstracted results with the component material yield stress and ultimate tensile strength.

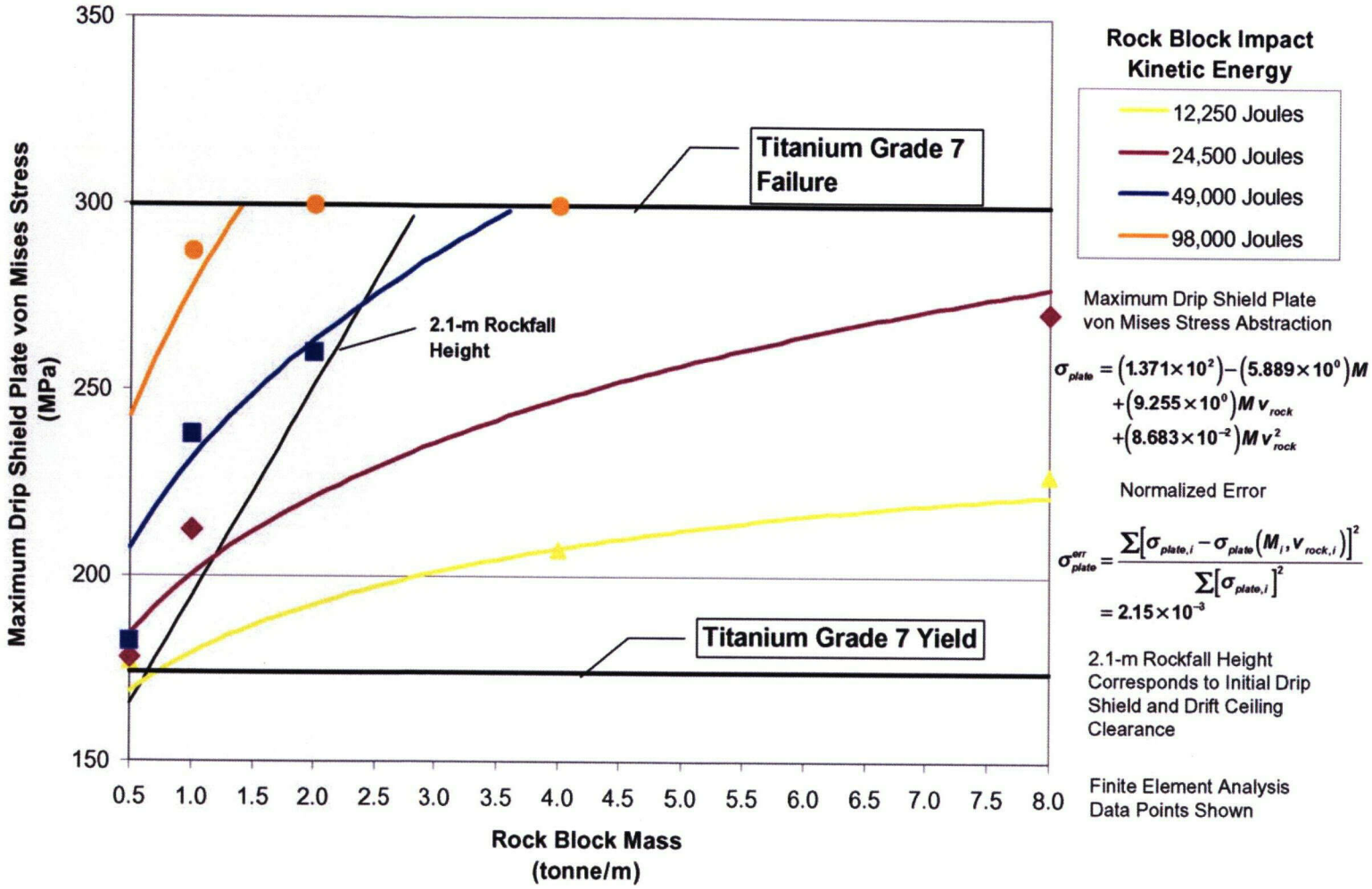

Figure 7-11. Maximum Drip Shield Plate von Mises Stress Abstraction for Rock Block Impacts

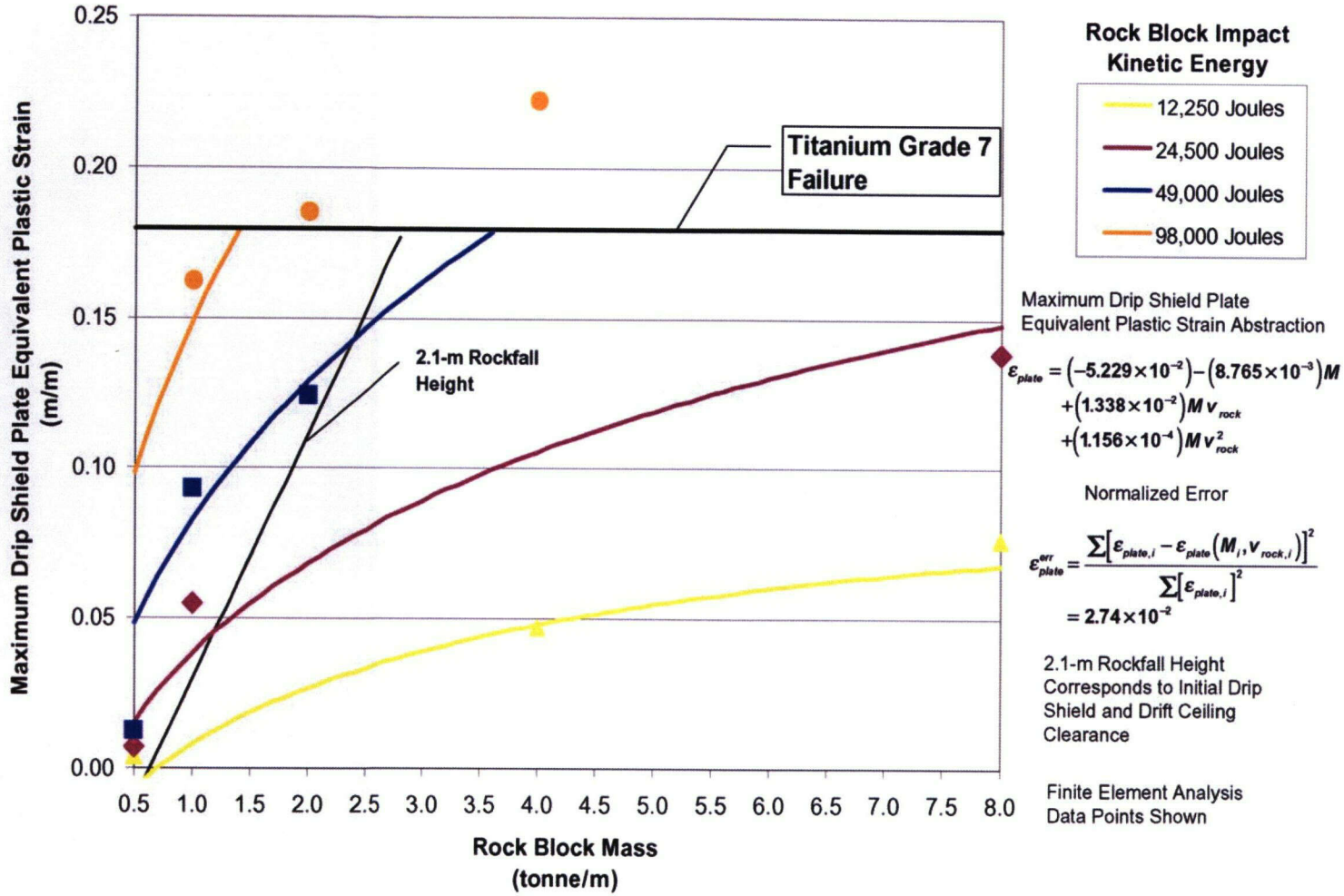

Figure 7-12. Maximum Drip Shield Plate Equivalent Plastic Strain Abstraction for Rock Block Impacts

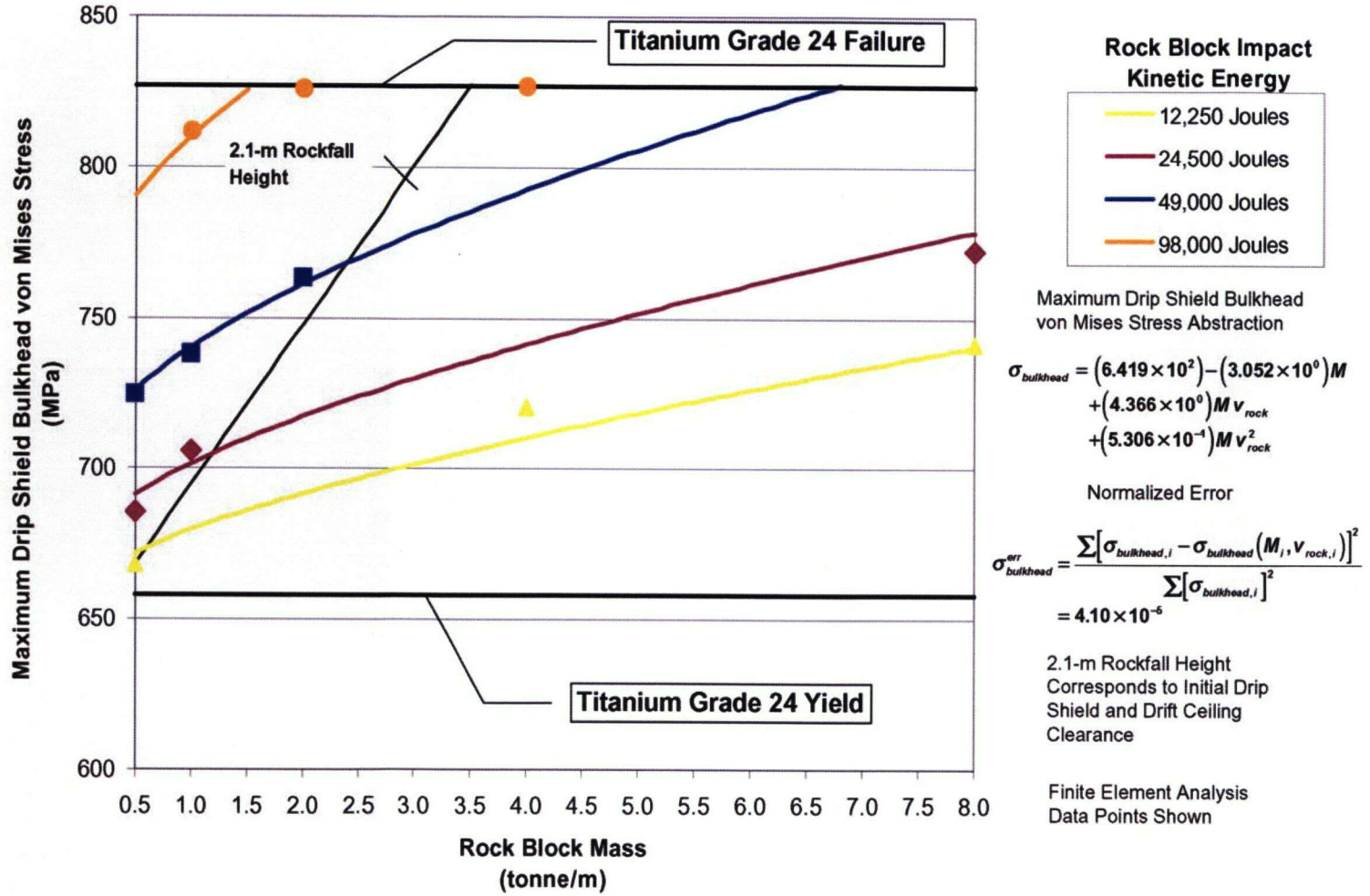

Figure 7-13. Maximum Drip Shield Bulkhead von Mises Stress Abstraction for Rock Block Impacts

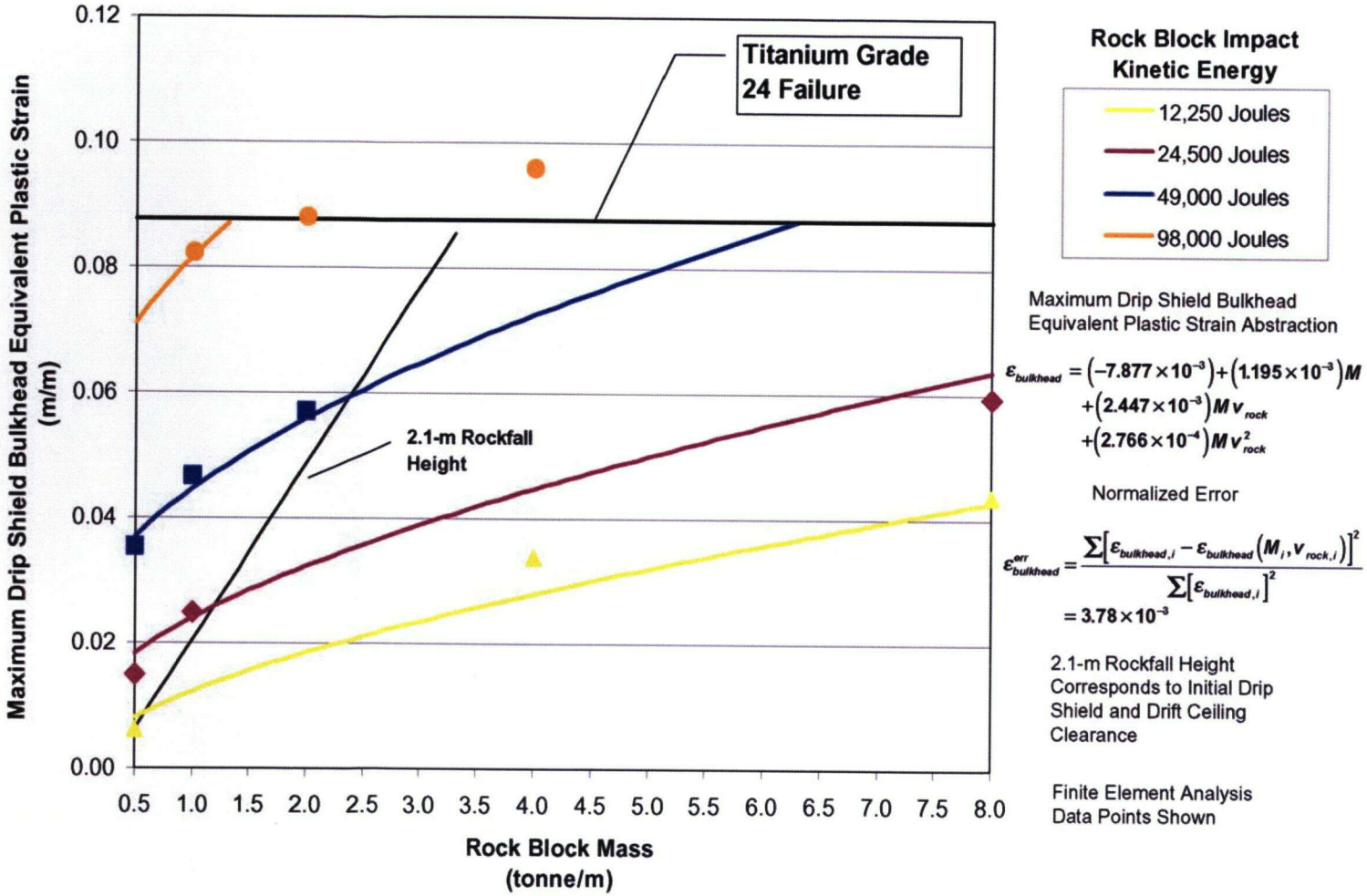

Figure 7-14. Maximum Drip Shield Bulkhead Equivalent Plastic Strain Abstraction for Rock Block Impacts

8 SEISMIC PERFORMANCE ANALYSES

It is expected that the proposed Yucca Mountain geologic repository will be subjected to earthquakes of varying magnitudes throughout the entire 10,000-year regulatory period. As a result, an understanding of the response of the various components of the engineered barrier subsystem components—including the drip shield, waste package, waste form, pallet, invert, and drift—to these earthquake loads, as well as potential interactions between them, need to be understood. This chapter documents the work accomplished thus far in achieving this goal. Specifically, the methodology used to approximate the natural frequencies and mode shapes of the drip shield are provided in Section 8.1.

Natural frequencies and mode shapes of a structure provide insight as to how the structure will behave when subjected to time-varying loading conditions. Although the discussion in this chapter focuses on seismic ground motions, time varying impact loads are also of interest [e.g., dynamic rock block impacts (see Chapter 7)]. Theoretically, impact loads will excite all the natural frequencies of the impacted structure. In practice, however, the magnitude, orientation, and duration of the impact load plays a significant role in determining which of the natural frequencies of the structure will govern its response. In the case of seismically generated ground motions, only those natural frequencies below 33 Hz are generally excited during an earthquake. The 33-Hz threshold was established by analyzing seismic ground motion measurements of actual earthquakes from around the world over several decades. These analyses demonstrated that earthquakes do not have any appreciable energy content at frequencies above 33 Hz.

8.1 Approximation of Drip Shield Natural Frequencies

The undamped natural frequencies and mode shapes of the drip shield are of interest for various kinematic constraint conditions. Accumulated rockfall rubble on the top and sides of the drip shield and its effects on the natural frequencies and mode shapes of the drip shield are also scenarios that needed to be investigated. The scope of the discussion presented here, however, is limited to how the drip shield natural frequencies and mode shapes were approximated using the finite element method without the effects of accumulated rockfall.

8.1.1 Drip Shield Finite Element Model Description

Sections 8.1.1.1 through 8.1.1.3 convey the rationale and technical bases for the various assumptions and boundary conditions implemented in the construction of the finite element model used to approximate the drip shield natural frequencies and mode shapes. Section 8.1.1.4 presents a summary of the results obtained from the drip shield natural frequency and mode shape analyses.

8.1.1.1 Drip Shield Finite Element Model Geometry

Figure 8-1 represents the finite element model geometry used to approximate the drip shield natural frequencies and mode shapes. The model was constructed using a mixture of plate

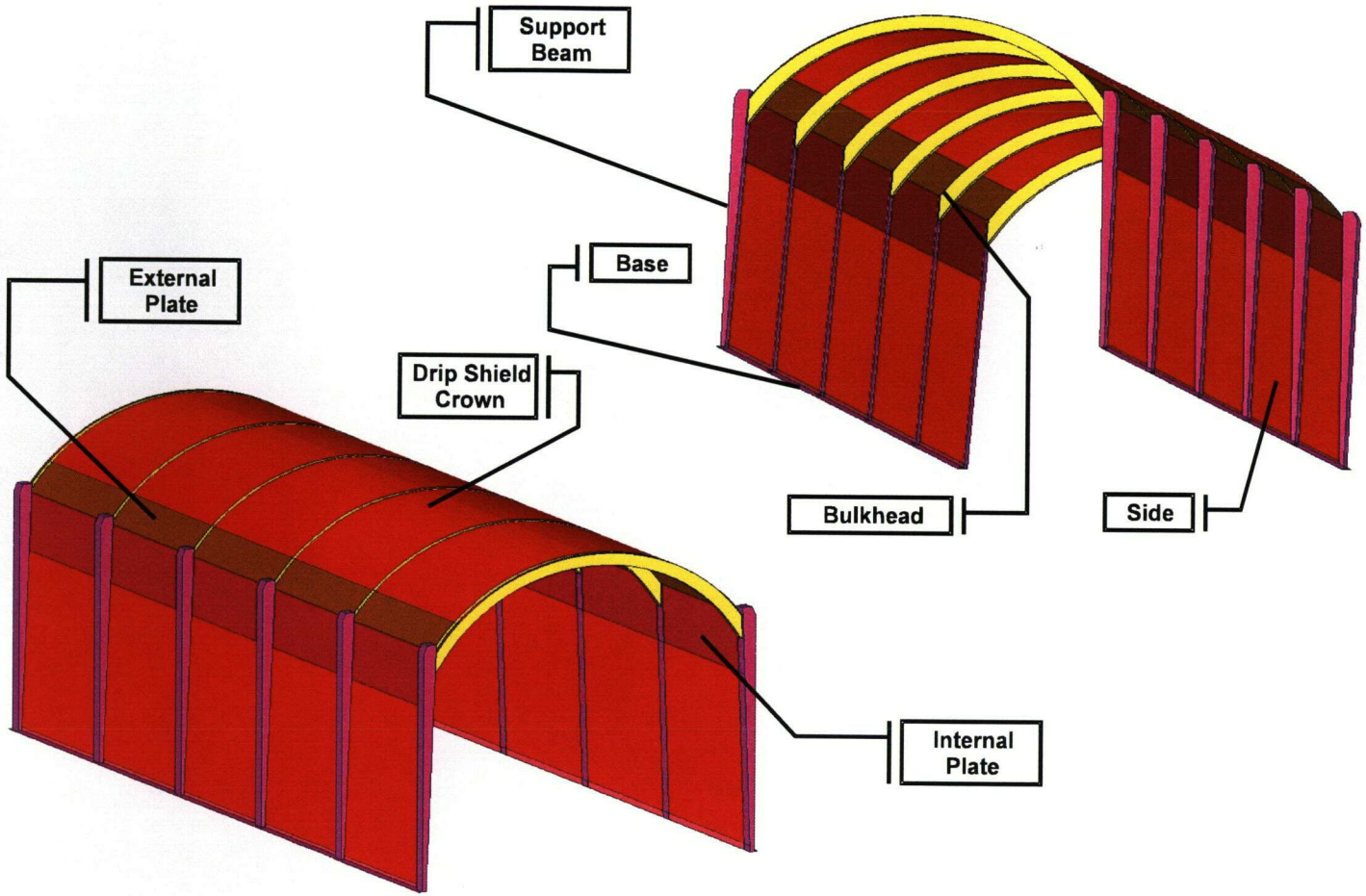

Figure 8-1. Model Used to Approximate the Drip Shield Natural Frequencies and Mode Shapes

and solid elements. Plate elements were used for the Titanium Grade 7 panel sections; including the drip shield crown, side plating, and inner and outer stiffening plates. Plate elements were also used to represent the Alloy 22 base of the structure. Solid hexahedron elements were used to represent the major structural support beam and bulkhead components. The total geometry approximated a complete drip shield structure (CRWMS M&O, 2000a, Reference Sketch Number SK-0148, Revision 05). To adequately approximate potential lateral and twisting mode shapes and their concomitant natural frequencies, geometric symmetry was not used to reduce the overall size of the drip shield finite element model. In addition, the effects of nonsymmetric boundary conditions could be investigated when using a full-scale model.

Linear material behavior and small strains and displacements are assumed when approximating the natural frequencies and mode shapes of a given structure. As a result, the use of plate elements to represent thin structural members, such as the Titanium Grade 7 plate regions, was justified. The ability to use plate elements in the construction of the drip shield finite element model significantly reduced the memory requirements and computational times required to perform the analyses relative to a model composed solely of solid elements.

All of the drip shield natural frequencies less than 50 Hz and their concomitant mode shapes were calculated using the finite element method of approximation.

8.1.1.2 Drip Shield Finite Element Model Boundary Conditions

8.1.1.2.1 Loads

No external loads, including gravity loads, were applied to the drip shield because it is a free-standing structure. The potential effects on the drip shield structural stiffness created by gravity loads have minimal influence on the approximated natural frequencies and mode shapes of the structure. Future analyses may be performed to assess the potential effects of accumulated rockfall rubble on the drip shield natural frequencies and mode shapes. Accumulated rockfall may affect both the effective mass and stiffness of the drip shield.

8.1.1.2.2 Kinematic Constraints

Three types of constraints were applied to the base of the drip shield structure to assess their effects on the natural frequencies and mode shapes of the structure. These constraints were referred to as free, lateral, and cantilever constraint conditions. The free constraint refers to the condition where the drip shield is allowed to translate and rotate freely in all directions. This condition provides insight into the combined effects of structural stiffness and mass distribution on the dynamic behavior of the drip shield structure. The free constraint condition represents the conditions that will exist in the drift after the gantry crane rails have corroded to a state where they no longer laterally constrain the transverse motion of the drip shield.

The lateral constraint limits translation at the base of the drip shield to axial and vertical motion only. In other words, the two sides of the drip shield base are not allowed to translate side-to-side, neither closer together nor further apart, but are only free to translate within parallel planes. Moreover, no rotational restrictions are applied at the base of the drip shield for the lateral constraint condition. The lateral constraint condition physically represents the restricted

motion of the drip shield base created by the presence of the gantry crane rails on the exterior of the drip shield and the waste package on its interior. The lateral constraint condition best represents the current engineered barrier subsystem and subsurface facility design. Figure 8-2 shows the base of the drip shield was constrained in the lateral x-direction.

The cantilevered constraint condition represents a completely constrained drip shield base. This constraint is similar to a base bolted or clamped to the floor. Figure 8-3 shows the bottom edges of the drip shield are constrained in all six degrees of freedom (i.e., the three translational and three rotational degrees of freedom). The cantilevered constraint was included in the investigation to address the possibility of the U.S. Department of Energy anchoring the drip shield to the invert.

Because each drip shield unit is loosely connected to the next by way of a post and slot configuration (CRWMS M&O, 2000a), the two ends of the drip shield did not have any constraints applied to them.

8.1.1.3 Drip Shield Finite Element Model Material Properties

The material properties used for the different drip shield components are documented in Section 5.1.3.

8.1.1.4 Summary of Drip Shield Natural Frequencies and Mode Shapes

Tables 8-1 through 8-3 summarize the drip shield natural frequencies and their corresponding mode shapes and modal participation factors for each of the three kinematic constraint conditions described earlier (i.e., free, lateral, and cantilevered). The Mode number indicates the order sorted by frequency. The data, however, are sorted by shape to facilitate the comparison of similar modes between the different constraint conditions.

Modal participation factors Px, Py, and Pz provide a relative measure of the directional response of a structure that is subjected to an excitation which has a frequency at, or near, the natural frequency of the corresponding mode. For example, a large Py, relative to Px and Pz for the given mode, indicates that an excitation with a frequency near the mode's natural frequency oriented in the y-direction will likely cause significant deformations of the structure. Conversely, the same excitation oriented in the x- or z-direction will cause structural deformations that are much smaller than those created in the y-direction. Modal participation factors can also be compared between different mode shapes because modal participation factors are related to the amount of structural mass participating in the motion. The ease with which two different modes can be excited is generally proportional to the magnitude of each mode's directional participation factor. This way Px can be compared for one mode shape with Pz in another. As an example, an excitation of the same energy (i.e., a hammer strike) would more easily excite the x-direction of Lateral Wall Zero (Px) with a lateral constraint than the z-direction of Lateral Wall One (Pz) with a cantilever constraint. Note that the participation factors presented in Tables 8-1 through 8-3 are not normalized to unity.

Figures 8-4 through 8-7 illustrate the various mode shapes listed in Tables 8-1 through 8-3. There are no mode shapes associated with rigid body modes. The free rigid body modes, as the name implies, are motions along unconstrained directions. Therefore, the free

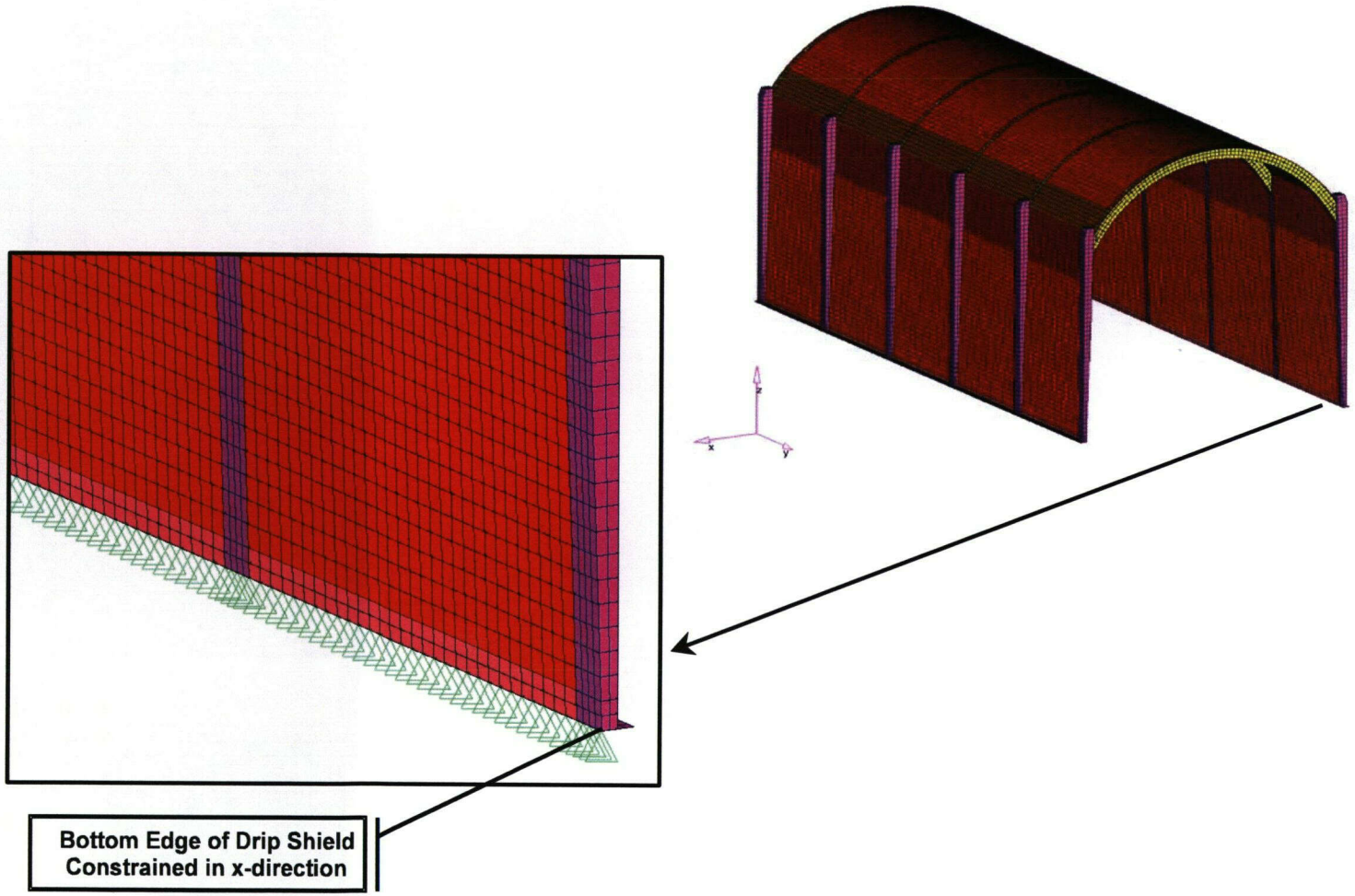

Figure 8-2. Illustration of the Drip Shield Lateral Constraint Condition

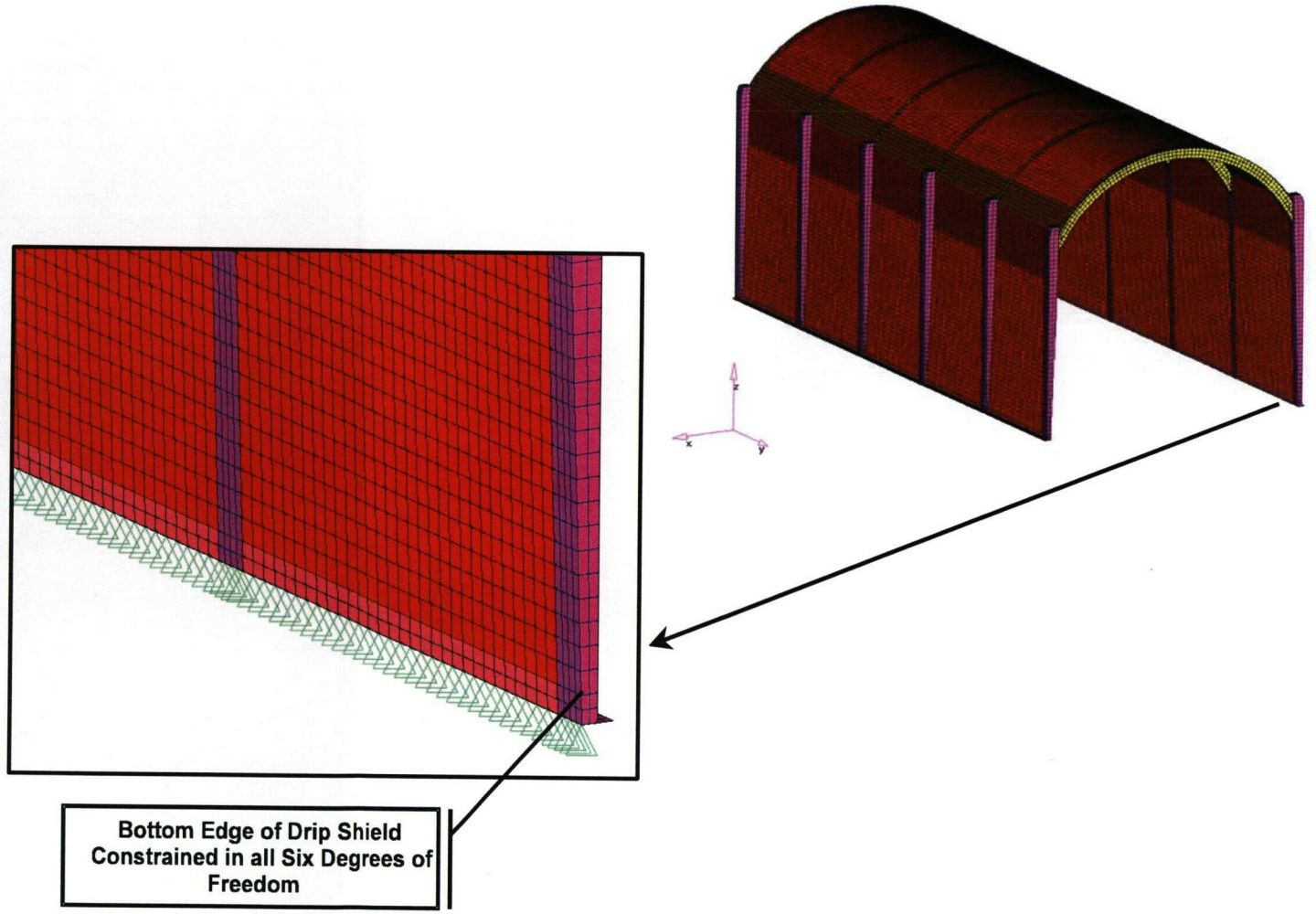

Figure 8-3. Illustration of the Drip Shield Cantilevered Constraint Condition

Table 8-1. Mode Shapes, Natural Frequencies, and Modal Participation Factors of the Drip Shield for Free Constraint Conditions

Mode Shape Designation	Mode Number	Frequency, Hz	Modal Participation Factors		
			Px	Py	Pz
Free Rigid Body Modes	1–6	0			
Walking	7	2.5	4.7×10^{-10}	8.4×10^{-12}	3.3×10^{-10}
Walk with Twist One	—	—	—	—	—
Vertical Up/Down	—	—	—	—	—
Flapping Zero	8	5.9	-1.6×10^{-9}	4.7×10^{-12}	-4.5×10^{-11}
Flapping One	9	7.2	-1.3×10^{-12}	6.2×10^{-11}	5.8×10^{-12}
Flapping Two	10	15.4	-1.7×10^{-10}	8.9×10^{-12}	-2.9×10^{-11}
Flapping Three	14	23.1	-1.9×10^{-11}	1.7×10^{-12}	4.0×10^{-13}
Flapping Four	18	34.5	-2.0×10^{-11}	-1.2×10^{-12}	3.0×10^{-12}
Lateral Wall Zero	—	—	—	—	—
Lateral Wall One	—	—	—	—	—
Lateral Wall Two—Mid	11	14.6	-1.4×10^{-10}	5.7×10^{-12}	7.0×10^{-13}
Lateral Wall Two—Mid	12	16.2	-2.3×10^{-10}	3.7×10^{-12}	-2.3×10^{-11}
Lateral Wall Two—End	13	16.6	3.6×10^{-11}	-4.3×10^{-12}	-3.5×10^{-12}
Lateral Wall Three	15	23.5	5.6×10^{-12}	4.1×10^{-12}	1.2×10^{-12}
Lateral Wall Four—Mid	17	33.9	5.1×10^{-12}	6.6×10^{-13}	-4.3×10^{-13}
Lateral Wall Five—Mid	20	45.1	-1.6×10^{-12}	3.5×10^{-14}	5.3×10^{-13}
Pinch Crown Zero	16	31.6	-6.4×10^{-11}	-1.9×10^{-12}	5.7×10^{-12}
Pinch Crown One	19	34.8	9.3×10^{-12}	3.9×10^{-12}	1.7×10^{-12}

Table 8-2. Mode Shapes, Natural Frequencies, and Modal Participation Factors of the Drip Shield for Lateral Constraint Conditions					
Mode Shape Designation	Mode Number	Frequency, Hz	Modal Participation Factors		
			Px	Py	Pz
Free Rigid Body Modes	1–4	0			
Walking	5	1.5	7.7×10^{-10}	-9.1×10^{-10}	6.8×10^{-10}
Walk with Twist One	7	9.1	1.3×10^{-10}	-4.4×10^{-12}	-3.3×10^{-11}
Vertical Up/Down	6	8.7	5.1×10^{-1}	-2.3×10^{-12}	2.8×10^{-11}
Flapping Zero	—	—	—	—	—
Flapping One	—	—	—	—	—
Flapping Two	—	—	—	—	—
Flapping Three	—	—	—	—	—
Flapping Four	—	—	—	—	—
Lateral Wall Zero	—	—	—	—	—
Lateral Wall One	10	37.7	6.6×10^{-1}	1.2×10^{-12}	-3.3×10^{-12}
Lateral Wall Two—Mid	11	39.0	7.6×10^{-2}	-3.0×10^{-13}	-2.5×10^{-13}
Lateral Wall Two—Mid	12	39.4	1.5×10^{-9}	-1.4×10^{-10}	-2.7×10^{-13}
Lateral Wall Two—End	13	40.0	5.5×10^{-1}	-7.1×10^{-13}	-6.9×10^{-13}
Lateral Wall Three	14	45.4	-2.2×10^{-7}	8.8×10^{-13}	-2.4×10^{-13}
Lateral Wall Four—Mid	—	—	—	—	—
Lateral Wall Five—Mid	—	—	—	—	—
Pinch Crown Zero	8	21.9	-2.3×10^{-4}	1.5×10^{-12}	-5.9×10^{-12}
Pinch Crown One	9	23.8	-3.7×10^{-12}	7.2×10^{-12}	-1.7×10^{-12}

Table 8-3. Mode Shapes, Natural Frequencies, and Modal Participation Factors of the Drip Shield for Cantilever Constraint Conditions					
Mode Shape Designation	Mode Number	Frequency, Hz	Modal Participation Factors		
			Px	Py	Pz
Free Rigid Body Modes	0	0	—	—	—
Walking	—	—	—	—	—
Walk with Twist One	—	—	—	—	—
Vertical Up/Down	—	—	—	—	—
Flapping Zero	—	—	—	—	—
Flapping One	—	—	—	—	—
Flapping Two	—	—	—	—	—
Flapping Three	—	—	—	—	—
Flapping Four	—	—	—	—	—
Lateral Wall Zero	1	7.3	1.0×10^{-4}	-5.0×10^{-11}	-3.7×10^{-1}
Lateral Wall One	4	46.7	8.9×10^{-1}	1.5×10^{-7}	2.9×10^{-2}
Lateral Wall Two—Mid	—	—	—	—	—
Lateral Wall Two—Mid	—	—	—	—	—
Lateral Wall Two—End	—	—	—	—	—
Lateral Wall Three	—	—	—	—	—
Lateral Wall Four—Mid	—	—	—	—	—
Lateral Wall Five—Mid	—	—	—	—	—
Pinch Crown Zero	2	26.7	-4.0×10^{-11}	-1.6×10^{-1}	-1.1×10^{-11}
Pinch Crown One	3	28.6	-1.1×10^{-8}	-7.4×10^{-3}	1.7×10^{-8}

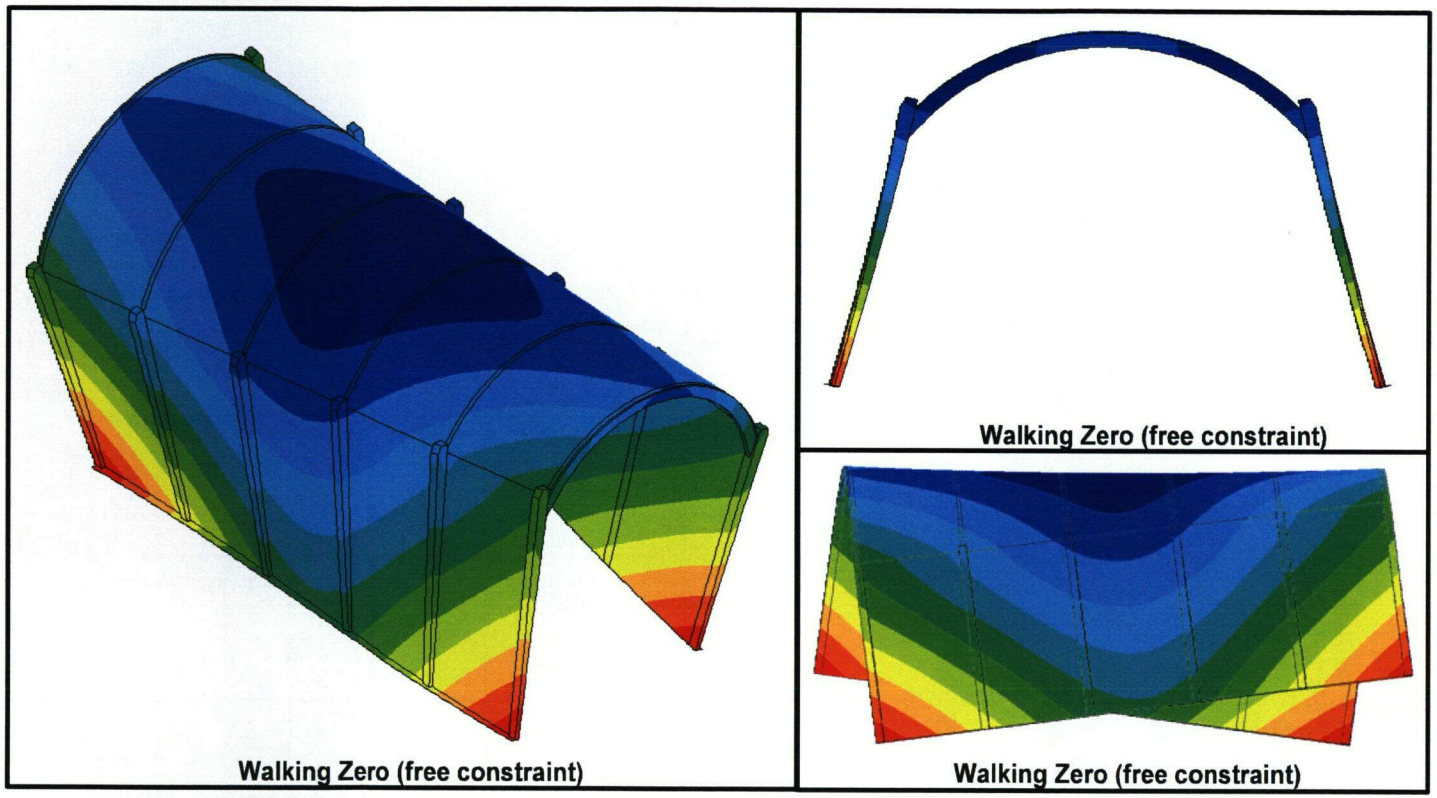

Contour colors represent relative deflection magnitude.

Figure 8-4. Illustration of the Drip Shield Walking Mode Shape

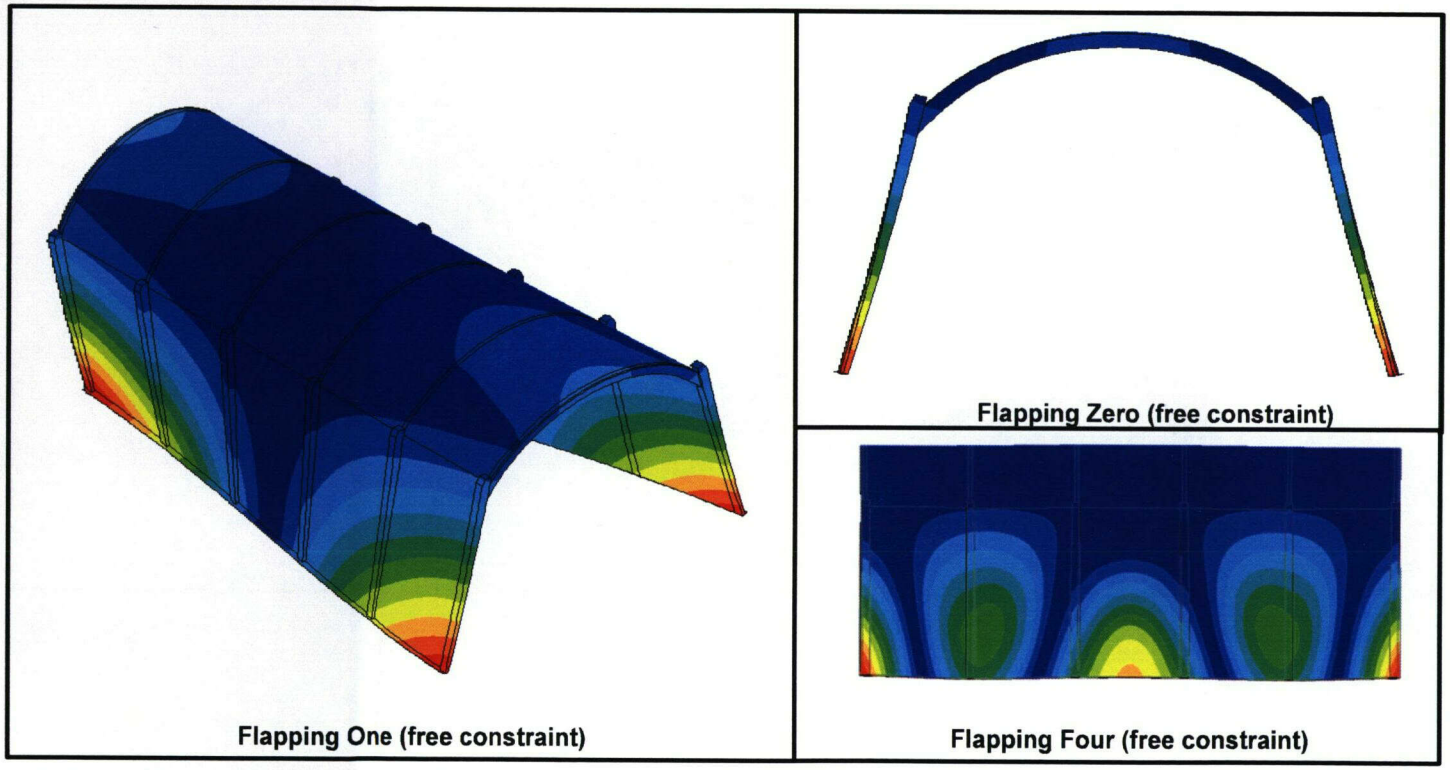

Figure 8-5. Illustration of the Drip Shield Flapping Mode Shape

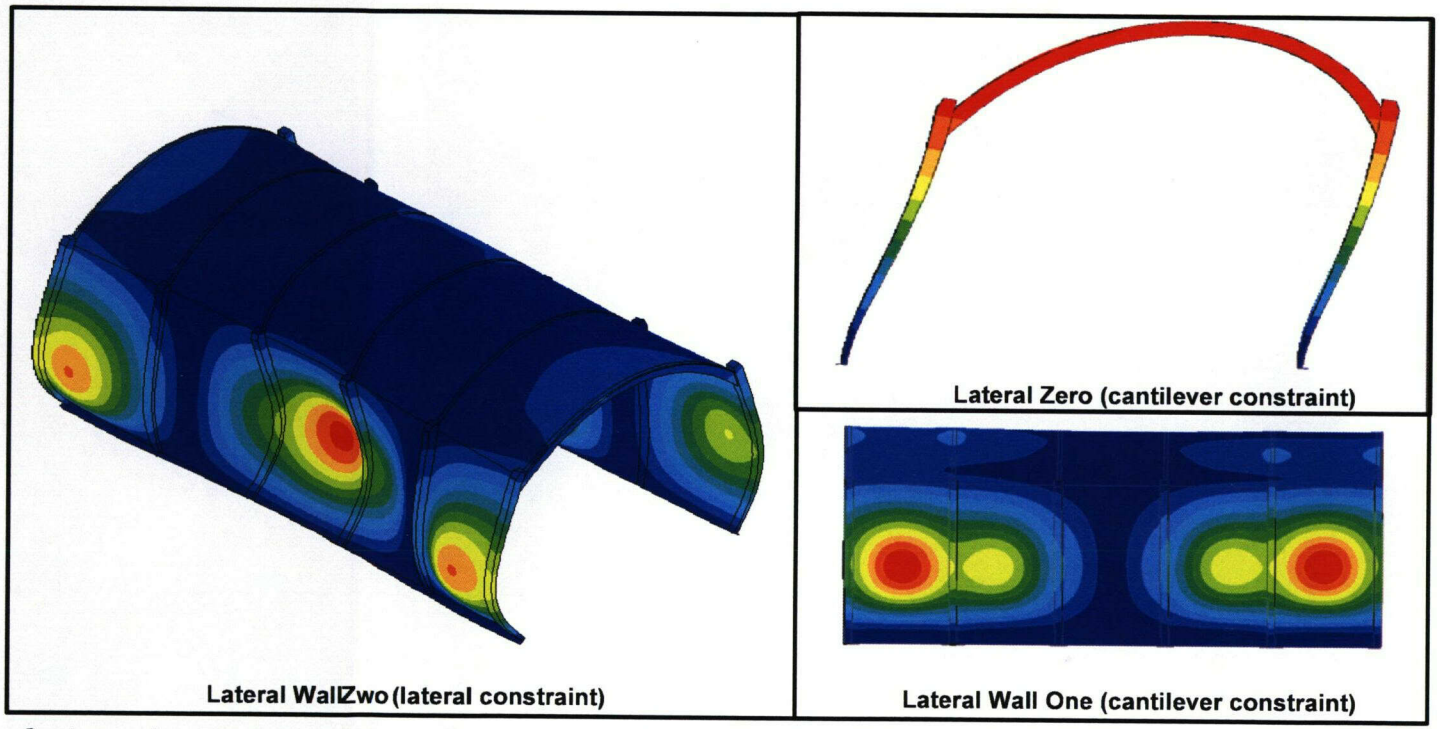

Contour colors represent relative deflection magnitude.

Figure 8-6. Illustration of the Drip Shield Lateral Wall Mode Shape

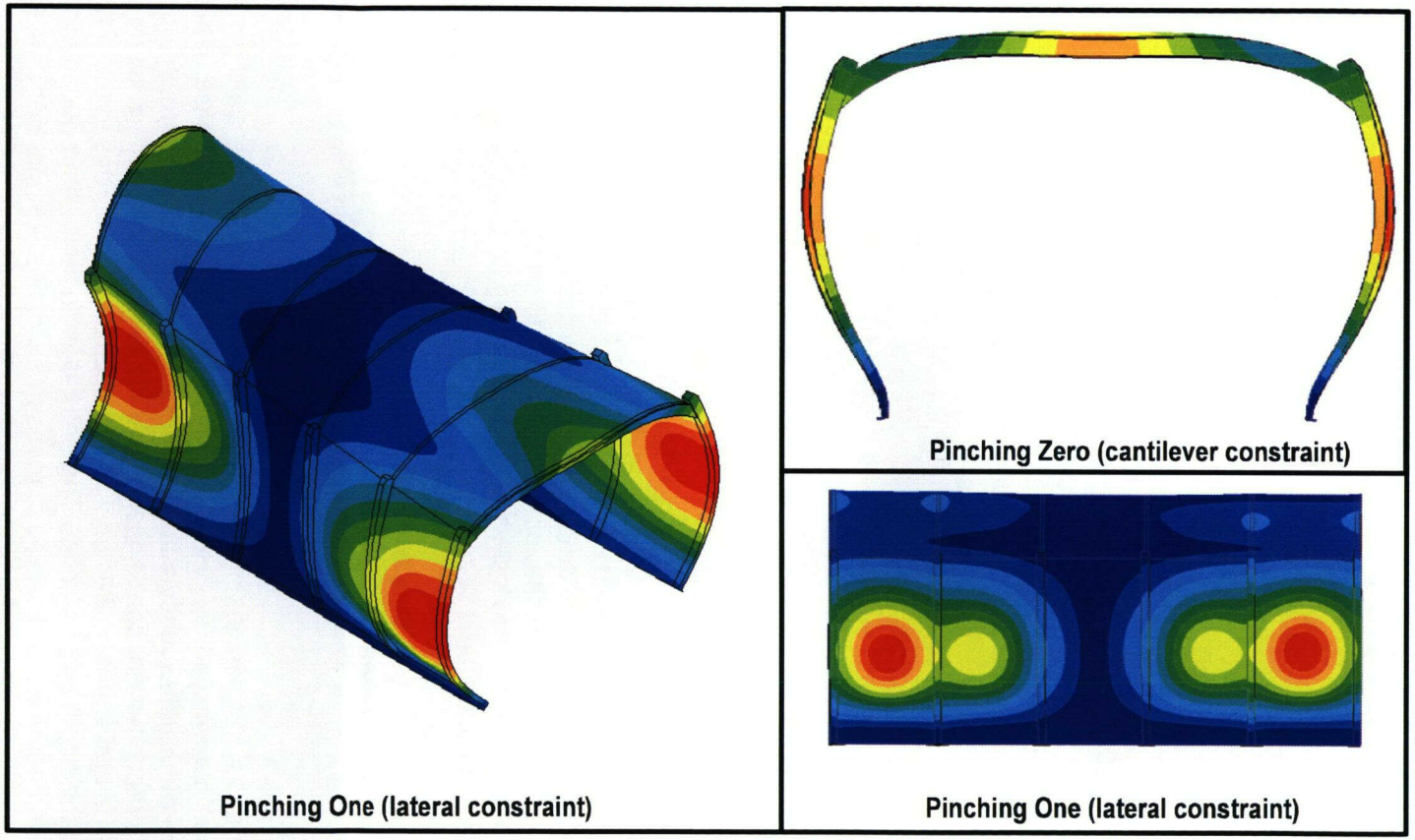

Contour colors represent relative deflection magnitude.

Figure 8-7. Illustration of the Drip Shield Pinch Crown Mode Shape

6/2/72

constraint condition has six rigid body modes because the structure is free to translate along the x-, y-, and z-axes as well as rotate about the x-, y-, and z-axes. Similarly, the lateral constraint has the effect of preventing x-axis translation and y-axis rotation. As a result, the lateral constraint condition has four rigid body modes. Finally, the cantilever constraint prevents any rigid body motions (i.e., no rigid body modes).

Walking mode shapes (see Figure 8-4) are characterized by the left and right sides of the drip shield moving forward on the right and aft on the left or vice versa. The visual effect is that the drip shield appears to be walking.

Before describing the remaining mode shape types, it is necessary to discuss what is meant by the order of these modes. Orders are included in the shape name starting at zero and increasing incrementally. Each order is an indication of the number of bends in the shape. For example, a zero order mode has no bends and represents a generally flat shape. An order of one indicates a simple arc shape while an order of two indicates an s-shape and so on. Specific features of each mode shape are described below and illustrated in Figures 8-5 through 8-7.

Flapping modes (see Figure 8-5) and lateral wall modes (see Figure 8-6) are very similar. They are both characterized by motion of the side walls but contrast in the deflection of the opposing wall. Flapping modes, as the name implies, have the appearance of the side walls flapping (i.e., the opposing wall motions are moving 180 degree out of phase with each other). In other words, the side walls deflect away or toward each other at the same moment. The lateral wall mode shapes, on the other hand, are dominated by motions wherein the opposing walls move in unison in the lateral direction (i.e., the opposing wall motions are in phase with each other). More succinctly, if the left wall moves laterally to the left, then the right wall also moves left and vice versa. It should also be noted that there are multiple lateral wall two mode shapes. It is quite common for natural frequency extraction analyses to calculate multiple shapes of the same basic pattern. Multiple mode shapes occur in the drip shield because the basic s-shape for the lateral wall two mode can have several permutations with the change of inflection occurring within different drip shield segments.

The pinch crown mode shapes (Figure 8-7) are similar to the flapping mode shapes except that the deformed shape is characterized by significant bending of the bulkhead and drip shield crown. In addition, the maximum deformation occurs above the drip shield base rather than on the base.

As expected, the natural frequencies of each of the constraint conditions were generally higher as kinematic constraints were added. However, this was not always the case between similar mode shapes. The natural frequency actually reduced for the two pinch crown mode shapes from the free to lateral constraint conditions. While the lateral constraint condition increased the drip shield's structural stiffness, this constraint condition also increased the mass participation along the direction of motion. The natural frequency was reduced for the pinch crown mode shapes because the increase in mass participation was greater than the increase in stiffness when changing from a free to lateral constraint condition.

The natural frequencies and mode shapes presented in Tables 8-1 through 8-3 clearly indicate that the type of constraint applied to the drip shield structure will have a significant influence on how the drip will respond to seismic excitations. For example, the number of modes within the

frequency range of a seismic event (i.e., less than or equal to 33 Hz) tended to decrease as additional constraints were added. In the case of the drip shield, the free constraint has 10 mode shapes, the lateral constraint has 5 mode shapes, and the cantilevered constraint has 3 mode shapes that were excited by frequencies less than 33 Hz. None of the 10 free constraint condition mode shapes exhibited a modal participation factor that would be considered to be more dominant than the others. The modal participation factors for the lateral constraint condition, however, indicate that two of the five mode shapes of interest can be considered to be more dominant for excitation frequencies below 33 Hz. These mode shapes are the Lateral Wall Zero and Pinch Crown Zero. Both of these mode shapes respond to excitation in the x-direction. All three of the mode shapes below 33 Hz for the cantilever constraint condition (i.e., Lateral Wall Zero, Pinch Crown Zero, and Pinch Crown One modes) have a relatively high modal participation factor in either the y- or z-direction (i.e., lateral or vertical direction).

Because the drip shield is emplaced as a free-standing structure in the current design of the engineered barrier subsystem, it is not clear how significant higher order effects caused by impact loads arising from the drip shield literally bouncing off of the invert foundation or waste package might be during an earthquake. The work described in the following section attempts to address this issue. The approximated effects of rock block impacts with the drip shield during an earthquake were discussed in Chapter 7.

8.2 Response of the Drip Shield to Seismic Excitations

This work has yet to be completed.

8.2.1 Finite Element Model Description

This work has yet to be completed.

8.2.2 Summary of Analysis Results

This work has yet to be completed.

8.2.3 Data Abstractions for MECHFAIL

This work has yet to be completed.

8.3 Approximation of Waste Package Natural Frequencies

This work has yet to be completed.

8.3.1 Finite Element Model Description

This work has yet to be completed.

8.3.2 Summary of Analysis Results

This work has yet to be completed.

8.4 Response of the Waste Package to Seismic Excitations

This work has yet to be completed.

8.4.1 Finite Element Model Description

This work has yet to be completed.

8.4.2 Summary of Analysis Results

This work has yet to be completed.

8.4.3 Data Abstractions for MECHFAIL

This work has yet to be completed.

9 SUMMARY OF RESULTS

The framework for a new Total-system Performance Assessment code module (MECHFAIL) designed to assess the effects of mechanical loading (i.e., static and dynamic rockfall loads and seismicity) on the engineered barrier subsystem was presented in Chapter 2. Specific components of the engineered barrier subsystem that are presently included in the MECHFAIL failure assessment are the drip shield, waste package, and drift. Potential failure mechanisms of the drip shield that have been accounted for include accumulated equivalent plastic strains that exceed the allowable ductility of the drip shield materials (i.e., the Titanium Grade 7 plates and Titanium Grade 24 bulkheads) attributable to dynamic rock block impacts and creep caused by static rockfall loads. The potential for drip shield buckling under static rockfall loads and seismic excitation are included as well. Although the abstractions have yet to be completed, the MECHFAIL module includes placeholders for assessing drip shield and waste package damage caused by direct seismic shaking and interactions with each other under static and dynamic rockfall loads.

As with the drip shield, the damage incurred by the waste package outer barrier was characterized in terms of the accumulated equivalent plastic strain. The von Mises stress of the waste package outer barrier was also evaluated to facilitate the assessment of stress corrosion cracking as a potential failure mechanism. Failure of the drift by way of thermal, mechanical, hydrological, and chemical degradation processes was accounted for using a time-based drift degradation rate. In addition, the effects of seismic events on drift degradation were explicitly included in the MECHFAIL module. The time varying aspects of drift degradation were correlated with the accumulation of static rockfall loads and occurrence of dynamic rockfall loads acting on the drip shield.

The seismic hazard curve implemented within the Total-system Performance Assessment code also was updated (see Chapter 3). This update reflects a new position taken by DOE at a recent public meeting[1]. This change in position is based on new geotechnical data that have not been released yet for review.

The new seismic hazard curve now uses the anticipated free surface ground motions at Yucca Mountain as the design basis subsurface ground motions for the repository horizon. The hazard curve was also expanded to include seismic ground motions for annual frequencies of exceedance to the 10^{-8} per year threshold required by 10 CFR Part 63. The updated seismic hazard curve is plotted in Figure 3-1.

The bounding static and dynamic rockfall loads and the approach taken to consider their spatial variability were presented in Chapter 4. Assuming an elliptical drift degradation geometry and bulking factors within the range of 1.15 to 1.5, it was demonstrated that the bounding static rockfall loads will lie somewhere in the range of 40 to 160 tonne/m [26,890 to 107,550 lb/ft] along the length of the drift. The rationale for assuming these loads will fully manifest themselves within the first 1,000 years was also provided. The methodology used to derive the distribution of rock block sizes within the lower lithophysal and middle nonlithophysal rock units was presented in Chapter 4 as well. It was determined from this study that the formation of

[1]DOE and NRC Public Meeting. Las Vegas, Nevada. August 6–8, 2002.

discrete rock blocks of any consequence within the lower lithophysal rock unit is unlikely because of its highly fractured nature.

The analysis of the middle nonlithophysal rock unit, however, indicated that there are rock blocks of sufficient size to cause damage to the drip shield and, potentially, the waste package (by driving the drip shield into the waste package after impact). The distribution of rock block sizes within the middle nonlithophysal rock unit is presented in Figures 4-11 and 4-12. These plots indicate that approximately 60 percent of these rock blocks have a volume of less than 1 m^3 [35.3 ft^3], which corresponds to a rock block mass of 2.7 tonne [5,955 lb] {assuming a rock mass density of 2.7 tonne/m^3 [169 lb/ft^3]}. Twenty-five percent of the rock blocks have a volume of 1 to 2 m^3 [35.3 to 70.6 ft^3] {2.7 to 5.4 tonne [5,955 to 11,910 lb]} and the remaining 15 percent have a volume greater than 2 m^3 [70.6 ft^3] {5.4 tonne [11,910 lbs]}.

The finite element models used for assessing the potential effects of static rockfall loads on the drip shield were described in Chapter 5. The results obtained from these analyses indicate the drip shield may buckle under static rockfall loads as small as 23 tonne/m [15,460 lb/ft]. Moreover, static rockfall loads sufficient to initiate creep of the drip shield Titanium Grade 7 plate can be as low as 15 tonne/m [10,083 lb/ft] and, for the Titanium Grade 24 bulkhead, 20 tonne/m [13,444 lb/ft]. These threshold loads were found to increase significantly if credit is taken for the structural support provided by the accumulated rockfall rubble that builds up around the drip shield side walls. The supporting effect of rock rubble accumulated around the drip shield side walls was difficult to precisely quantify, however, because of the sensitivity of the buckling and creep threshold loads to the effective Young's modulus assumed for the accumulated rockfall rubble. For example, the drip shield buckling load increased from 95 to 138 tonne/m [63,860 to 92,760 lb/ft] by only changing the rock rubble effective Young's modulus from 3 to 6 MPa [4.35×10^2 to 8.70×10^2 psi]. As a result, a beta function defining the drip shield buckling load was generated (see Figure 5-13). This curve was created assuming the drip shield will not buckle under static rockfall loads less than 25 tonne/m [16,800 lb/ft] and no more than 20 percent of the drip shields will have a buckling load threshold greater than 60 tonne/m [40,330 lb/ft]. In addition, Table 5-6 clearly indicated a correlation between the drip shield buckling load and the maximum von Mises stress within the drip shield plate and bulkhead components. Because the drip shield buckling load is assigned to each spatial grid element using a beta distribution curve as described in Section 5.3.1, the static rockfall load required to generate stresses within the drip shield plate and bulkheads that satisfy the initiation of creep stress threshold was abstracted in terms of the assigned drip shield buckling load.

Chapter 6 presented the concerns regarding potential drip shield and waste package interactions under static rockfall loads. Assuming a contact area between the drip shield bulkhead and waste package outer barrier of 7.6×10^{-4} m^2 [8.18×10^{-3} ft^2], the static rockfall load needed to breach (i.e., exceed the ultimate tensile strength) the Alloy 22 outer barrier is 76.3 tonne/m [51,290 lb/ft]. If the ASME International failure criterion is used, this threshold load is reduced to 68.7 tonne/m [46,180 lb/ft]. The static rockfall loads needed to breach the waste package will be even smaller if the effective increase in these loads during seismic events is considered. In addition to the concern pertaining to the contact stress created between the waste package and drip shield bulkhead, the contact stress between the waste package and supporting pallet is also a concern. The interaction between the waste package and pallet is more likely to generate localized contact stresses that will exceed the allowable material limits of Alloy 22 than those associated with the waste package and drip shield bulkhead interaction. The reason for this conclusion is the recognition that there will be at least

five bulkheads transmitting static rockfall loads to the waste package, and there are only four contact points between the waste package and pallet. Moreover, the effective contact area between the waste package and pallet is expected to be quite small because the waste package will tend to deflect in a manner consistent with a simply supported beam with pivot points located on the v-notched edge of the pallet support nearest the midspan of the waste package.

There are several important factors that have yet to be adequately considered in the waste package and drip shield interaction analysis: (i) the initial contact area that has been assumed for the drip shield and waste package interaction can be expected to increase significantly as the outer barrier plastically deforms under the applied load; (ii) the contribution of bending moments to the stress state of the Alloy 22 in the various contact regions created by the overall structural response of the waste package and localized deformations in the immediate areas of the various contact interactions; and (iii) a line load, as opposed to the assumed uniform area distribution, may be more appropriate to approximate the contact stress between the waste package and drip shield bulkhead. A line contact between the drip shield and waste package would require significantly more plastic straining of the outer barrier to develop a sufficient contact area for any potential state of equilibrium to be achieved before a breach occurs.

Several abstractions were developed to characterize the response of the drip shield to dynamic rock block impacts (see Chapter 7). Given the rock block mass and impact velocity, the following can be approximated: (i) the maximum deflection of the drip shield; (ii) the maximum von Mises stress and corresponding equivalent plastic strain for the drip shield plate and bulkhead; and (iii) the impact velocity of the drip shield with the waste package for different drip shield and waste package clearances. It was also found that impacts from rock blocks of 8 tonne/m [5,380 lb/ft] length will cause the drip shield to buckle. Smaller rock blocks are likely to cause the drip shield to buckle if they fall from heights greater than the initial 2.1 m [6.89 ft] distance between the drip shield crown and the drift ceiling. The presence of rock rubble was not included in the drip shield and rock block impact analyses because the primary focus of the parametric study was to establish the effects of varying rock block size and rock block impact velocity (i.e., fall height) on the structural behavior of the drip shield. If it is determined that rock block impact with the drip shield is risk significant, additional analyses can be performed to study the potentially beneficial and adverse effects associated with the presence of rock rubble buttressing the drip shield. It is expected that including the presence of rock rubble would reduce the deflection of the drip shield while increasing the likelihood of the Titanium Grade 7 plate being breached for a given rock block impact.

The natural frequencies and mode shapes for the drip shield with varying boundary conditions were presented in Chapter 8. These analyses demonstrated that the type of constraint applied to the drip shield structure will have a significant influence on how the drip will respond to seismic excitations. For example, the number of modes within the frequency range of a seismic event (i.e., less than or equal to 33 Hz) tend to decrease as additional constraints are added. In the case of the drip shield, the free constraint has 10 mode shapes, the lateral constraint has 5 mode shapes, and the cantilevered constraint has 3 mode shapes that are excited by frequencies less than 33 Hz. None of the 10 free constraint condition mode shapes exhibit a modal participation factor more dominant than the others. The modal participation factors for the lateral constraint condition, however, indicate two of the five mode shapes are more dominant for excitation frequencies below 33 Hz. These mode shapes are the Lateral Wall Zero and Pinch Crown Zero, which respond to excitation in the x-direction (i.e., axial direction).

All three of the mode shapes below 33 Hz for the cantilever constraint condition (i.e., Lateral Wall Zero, Pinch Crown Zero, and Pinch Crown One modes) have a relatively high modal participation factor in either the y- or z-direction (i.e., lateral or vertical direction). Because the drip shield is emplaced as a free-standing structure in the current design of the engineered barrier subsystem, it is not clear how significant higher order effects caused by impact loads arising from the drip shield literally bouncing off the invert foundation or waste package might be during an earthquake.

Only two MECHFAIL spatial grid elements are presently assigned to each Total-system Performance Assessment code Version 5.0 beta subarea. One represents the lower lithophysal rock unit, and the other represents the middle nonlithophysal rock unit. The results obtained for each of these spatial grid elements are weighted using the area percentage of the rock type for the given subarea. A stand-alone version of the MECHFAIL module was used to determine what effect, if any, increasing the number of spatial grid elements per subarea will have on the calculated number of drip shield and drift failures. After 100 realizations, the average number of drip shield and drift failures 520 years into the postclosure period do not appear to be affected by the number of spatial grid elements (see Figures 9-1 and 9-2). The standard deviation, however, for both the calculated number of drip shield and drift failures is nearly 35 percent when only two spatial grid elements per subarea are used. Figure 9-1 indicates that 30 spatial grid elements per subarea are required to reach a converged standard deviation value of approximately 9 percent for the number of drip shield failures. Similarly, Figure 9-2 shows that 20 spatial grid elements per subarea are required to reach a converged standard deviation value of approximately 12 percent for the number of drift failures.

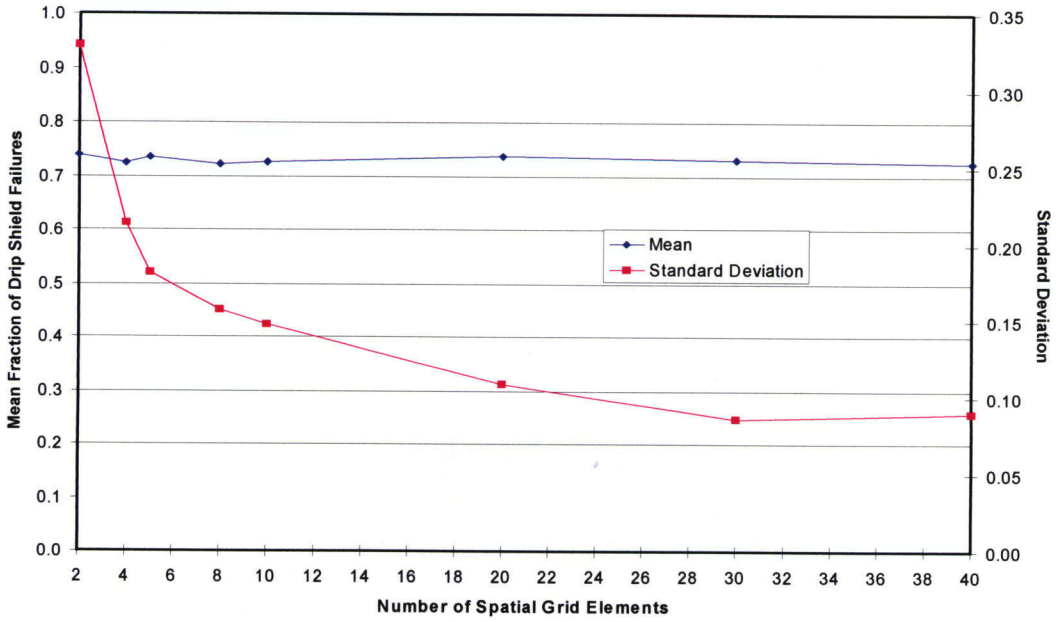

Figure 9-1. Mean Fraction and Standard Deviation of Drip Shield Failures as a Function of the Number of Spatial Grid Elements per Subarea

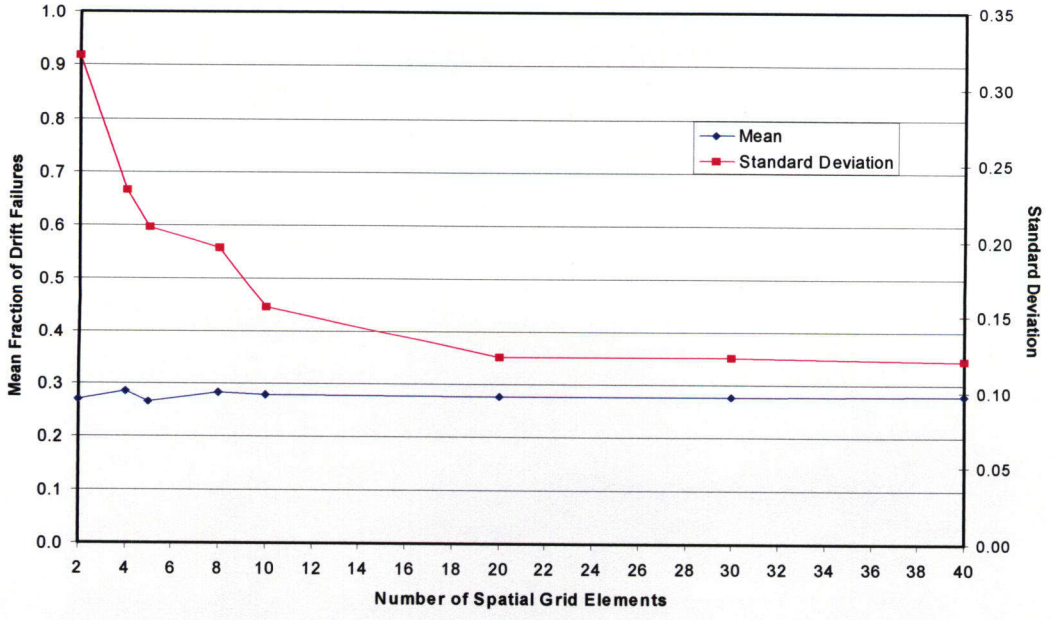

Figure 9-2. Mean Fraction and Standard Deviation of Drift Failures as a Function of the Number of Spatial Grid Elements per Subarea

10 FUTURE WORK

The abstraction of the accumulated rockfall loads and the long-term geometry of the emplacement drifts are completed. This abstraction could be improved, however, if site-specific data for the bulking factors of the lower lithophysal and middle nonlithophysal rock units can be obtained. In the case of discrete rock-block impact loads, estimates of the volume of rockfall associated with a given seismic event are based on generic observations and subjective assessments of drift damage. If it can be established that the current assumptions regarding the volume of rockfall for a given seismic event are bounding and the effects on the engineered barrier subsystem are negligible, then further refinement of the dynamic rockfall load parameters [i.e., g_o and g_{max} (see Figure 4-14)], may not be necessary. Recall that g_o and g_{max} define the range of mean peak horizontal ground accelerations at which damage to the drift is characterized as being minor (i.e., g_o), and major (i.e., g_{max}). Based on preliminary analyses performed using the MECHFAIL module, potential failure of the drip shield will likely be dominated by buckling under static rockfall loads. Moreover, discrete rock impact is only expected to occur in the middle nonlithophysal rock unit, which represents a relatively small percentage of the repository footprint.

The potential failure mechanisms of the drip shield associated with static rockfall loads are buckling and creep. The static rockfall loads needed to cause buckling or initiate creep are strongly dependent on the amount of structural support provided by the rockfall rubble that accumulates around the drip shield side walls. It is not clear if the assumed distributions of the static rockfall load threshold values for buckling and creep are in fact bounding. To be considered bounding, the static rockfall load threshold values used for buckling {23 tonne/m [15,460 lb/ft]} and creep {15 tonne/m [10,080 lb/ft]} for the drip shield plate and 20 tonne/m [13,440 lb/ft] for the drip shield bulkhead need to be established using the analysis results from models that do not take any credit for lateral support from rockfall rubble that may accumulate between the drip shield and the drift sidewall. Because the minimum static rockfall load will be 40 tonne/m [26,890 lb/ft] after 1,000 years, these bounding buckling and creep threshold values would result in a prediction that all of the drip shields will fail by buckling shortly after cessation of maintenance of the repository ground support system. Recognizing that U.S. Department of Energy (DOE) is presently adding structural reinforcement to its initial design of the drip shield, it is recommended that further analysis of the drip shield subjected to static rockfall loads be postponed until the new drip shield design is finalized.

Abstractions needed to assess the potential failure of the drip shield waste package caused by interactions between them under static or dynamic rockfall load conditions, direct seismic shaking, and direct rock block impacts have yet to be developed. The process level models needed to develop these abstractions are presently under construction.

The various abstractions for the drip shield response to dynamic rock block impacts acceptably represent the potential failures that may occur from this type of loading condition so long as the drip shield does not interact with the waste package.

Finally, no analysis has been done to develop the information needed for an abstraction of the potential mechanical failure modes of the various waste forms that DOE plans to dispose at the proposed repository. Of particular concern is the potential for spent nuclear fuel assembly cladding failures under seismic conditions. A review of DOE documents that address this

concern indicates that the full range of potential seismic event magnitudes have not been addressed. Moreover, the analyses used in the DOE documents employ unacceptable assumptions that underestimate the potential for cladding failures under seismic conditions. As a result, it is recommended that work should be pursued in this area to establish a better understanding of the critical parameters and issues regarding this matter.

11 REFERENCES

ASME International. *ASME International Boiler and Pressure Vessel Code.* New York City, New York: ASME International. 2001.

ASTM International. *Standard Specification for Low-Carbon Nickel-Molybdenum-Chromium, Low-Carbon Nickel-Chromium-Molybdenum, Low-Carbon Nickel-Chromium-Molybdenum-Copper, Low-Carbon Nickel-Chromium-Molybdenum-Tantalum, and Low-Carbon Nickel-Chromium-Molybdenum-Tungsten Alloy Plate, Sheet, and Strip.* Philadelphia, Pennsylvania: ASTM International. pp. B575–98. 1998.

ASM International. *Material Properties Handbook: Titanium Alloys.* Materials Park, Ohio: ASM International. 1994.

Brady, B.H.G. and E.T. Brown. *Rock Mechanics for Underground Mining.* London, United Kingdom. George Allen & Unwin. 1985.

CRWMS M&O. "Yucca Mountain Science and Engineering Report." DOE/RW–0539. Las Vegas, Nevada: CRWMS M&O. 2001.

———. "Design Analysis for the Ex-Container Components." ANL–XCS–ME–000001. Rev 00. Las Vegas, Nevada: CRWMS M&O. 2000a.

———. "Drift Degradation Analysis." ANL–EBS–MD–000027 Rev 01. Las Vegas, Nevada: CRWMS M&O. 2000b.

———. "Fracture Geometry Analysis for the Stratigraphic Units of the Repository Host Horizon." ANL–EBS–GE–000006. Rev 00. Las Vegas, Nevada: CRWMS M&O. 2000c.

———. "License Application Design Selection Report." B00000000–01717–4600–00123. Rev 01. Las Vegas, Nevada: CRWMS M&O. 1999a.

———. "Enhanced Design Alternative II Report." B00000000–01717–5705–00131. Rev 00. Las Vegas, Nevada: CRWMS M&O. 1999b.

———. "Drip Shields LA Reference Design Feature Evaluation #2." B00000000–01717–2200–00207. Rev 00. Las Vegas, Nevada: CRWMS M&O. 1999c.

———. "Seismic Ground Motion Hazard Inputs." WP–NEP–99309.T. MOL.19991005.0147. Las Vegas, Nevada: CRWMS M&O. 1999d.

DOE. "Viability Assessment of a Repository at Yucca Mountain, Overview." DOE/RW–0508. Las Vegas, Nevada: DOE, Office of Civilian Radioactive Waste Management. 1998a.

———. "Viability Assessment of a Repository at Yucca Mountain." Volume 2: Preliminary Design Concept for the Repository and Waste Package. DOE/RW–0508V2. Las Vegas, Nevada: DOE, Office of Civilian Radioactive Waste Management. 1998b.

———. "Seismic Design Methodology for a Geologic Repository at Yucca Mountain, Topical Report." YMP–0030NP. Las Vegas, Nevada: DOE. 1995.

Gute, G.D., A. Ghosh, S. Hsiung, and A.H. Chowdhury. "Assessment of Mechanical Response of Drip Shields Under Repository Environment—Progress Report 2." San Antonio, Texas: CNWRA. 2001.

Gute, G.D., A. Ghosh, S.M. Hsiung, and A.H. Chowdhury. "Assessment of Mechanical Response of Drip Shields Under Repository Environment—Progress Report." San Antonio, Texas: CNWRA. 2000.

Hoek E. and E.T. Brown. *Underground Excavations in Rock*. London, United Kingdom. Institution of Mining and Metallurgy. 1980.

Lambe, T.W. and R.V. Whitman. *Soil Mechanics*. New York City, New York: John Wiley &Sons, Inc. 1969.

Manteufel, R.D., M.P. Ahola, D.R. Turner, and A.H. Chowdhury. "A Literature Review of Coupled Thermal-Hydrological-Mechanical-Chemical Processes Pertinent to the Proposed High-Level Nuclear Waste Repository at Yucca Mountain." NUREG/CR–6021. NRC. 1993.

Marsal, R.J. "Mechanical Properties of Rockfill." *Embankment-Dam Engineering*, R.C. Hirschfeld and S.J. Poulos, eds. New York City, New York: John Wiley & Sons. 1973.

Neuberger, B.W., C.A. Greene, and G.D. Gute. "Creep Analyses of Titanium Drip Shield Subjected to Rockfall Static Loads in the Proposed Geologic Repository at Yucca Mountain." Scientific Basis for Nuclear Waste Management XXV. B.P. McGrail and G.A. Cragnolino, eds Symposium Proceedings 713. Pittsburgh, Pennsylvania: Materials Research Society. 2002.

NRC. "Input to Repository Design and Thermal-Mechanical Effects Issue Resolution Status Report." Rev 3. Washington, DC: NRC. 2000.

———. NUREG/CR–5440, "Critical Assessment of Seismic and Geomechanics Literature Related to a High-Level Nuclear Waste Underground Repository." Washington, DC: NRC. 1989.

Ofoegbu, G.I. "Thermal-Mechanical Effects on Long-Term Hydrological Properties at the Proposed Yucca Mountain Nuclear Waste Repository." CNWRA 2000-03. San Antonio, Texas: CNWRA. 2000.

Ofoegbu, G.I. "Variations of Drift Stability at the Proposed Yucca Mountain Repository. Rock Mechanics for Industry." *Proceedings of the 37th U.S. Rock Mechanics Symposium* 2. B. Amadei, R.L. Kranz, G.A. Scott, and P.H. Smeallie, eds. Rotterdam, Netherlands: A.A. Balkema. pp. 767–773. 1999.

Owen, G.N, and R.E. Scholl. *Earthquake Engineering of Large Underground Structures.* FHWA/RD–80/195. Washington, DC: U.S. Department of Transportation. 1981.

U.S. Department of Defense. "Military Handbook: Metallic Materials and Elements for Aerospace Vehicle Structures." MIL–DBK–5H. Washington, DC: U.S. Department of Defense. 1998.

United States Geological Survey. "Geological, Geophysical, and *In Situ* Stress Investigations in the Vicinity of the Dining Car Chimney, Dining Car/Hybla Gold Drifts, Nevada Test Site." Open-File Report 82-137. Denver, Colorado: USGS. 1982.

Wong, F., D. Tennant, J. Isenberg, C. Ludwig, R. Hart, B. Dasgupta, L. Lorig, P. Cundall, and E. Dawson. "Tunnel Size Effects." DNA–TR–91–19. Alexandria, Virginia: Defense Nuclear Agency. 1991.

APPENDIX A

APPLICABLE KEY TECHNICAL ISSUE AGREEMENTS

Table A–1 delineates the various key technical issue agreements between the U.S. Department of Energy (DOE) and U.S. Nuclear Regulatory Commission (NRC) that pertain to the performance assessment of the engineered barrier subsystem when subjected to rockfall and seismic ground motions.

Table A-1. Key Technical Issue Agreements that Pertain to the Performance Assessment of the Engineered Barrier Subsystem when Subjected to Rockfall and Seismic Ground Motions	
Key Technical Issue Agreement Number	**NRC and DOE Agreement**
CLST.1.14	Provide the justification for not including the rockfall effect and dead load from drift collapse on stress corrosion cracking of the waste package and drip shield. DOE will provide the justification for the rockfall and dead-weight effects in the next revision of the stress corrosion cracking Analysis and Model Report (ANL–EBS–MD–000005) prior to license application.
CLST.2.02	Provide the documentation for the point loading rockfall analysis. DOE stated that point loading rockfall calculations will be documented in the next revisions of Analysis and Model Reports ANL–XCS–ME–000001, Design Analysis for the Ex-Container Components, and ANL–UDC–MD–000001, Design Analysis for **UCF** Waste Packages, both to be completed prior to license application.
CLST.2.06	Provide the technical basis for the mechanical integrity of the inner overpack closure weld. DOE will provide the documentation in Analysis and Model Report, ANL–UDC–MD–000001, Revision 00, Design Analysis for UCF Waste Packages in the next revision, prior to license application.
CLST.2.08	Provide documentation of the path forward items in the "Subissue 2: Effects of Phase Instability of Materials and Initial Defects on the Mechanical Failure and Lifetime of the Containers" presentation, slide 16 [future rockfall evaluations will address: (1) effects of potential embrittlement of waste package closure material after stress annealing due to aging; (2) effects of drip shield wall thinning due to corrosion; (3) effects of hydrogen embrittlement on titanium drip shield; and (4) effects of multiple rock blocks falling on waste package and drip shield; future seismic evaluations will address the effects of static loads from fallen rock on drip shield during seismic events]. DOE stated that the rockfall calculations addressing potential embrittlement of the waste package closure weld and rock falls of multiple rock blocks will be included in the next revision of the Analysis and Model Report, ANL–UDC–MD–000001, Design Analysis for UCF Waste Packages, to be completed prior to License Application. Rock fall calculations addressing drip shield wall thinning due to corrosion, hydrogen embrittlement of titanium, and rock falls of multiple rock blocks will be included in the next revision of the Analysis and Model Report, ANL–XCS–ME–000001, Design Analysis for the Ex-Container Components, to be completed prior to license application. Seismic calculations addressing the load of fallen rock on the drip shield will be included in the next revision of the Analysis and Model Report, ANL–XCS–ME–000001, Design Analysis for the Ex-Container Components, to be completed prior to license application.
CLST.3.10	The agreement addresses CLST Subissues 3 & 4. Provide analysis of the rockfall and vibratory loading effects on the mechanical failure of cladding, as appropriate. DOE stated that the vibratory effects are documented in Sanders et al., 1992, SAND90–2406, A Method For Determining the Spent-Fuel Contribution To Transport Cask Containment Requirements. This will be discussed in the Structural Deformation and Seismicity Key Technical Issue meeting. The analysis of the rockfall effects on the mechanical failure of cladding will be addressed if the agreed to updated rockfall analysis in Subissue #2, Item 8 and Subissue #1, Item 14 demonstrate that the rock will penetrate the drip shield and damage the waste package.

Table A-1. Key Technical Issue Agreements that Pertain to the Performance Assessment of the Engineered Barrier Subsystem when Subjected to Rockfall and Seismic Ground Motions (Continued)	
Key Technical Issue Agreement Number	**NRC and DOE Agreement**
RDTME.3.17	Provide the technical basis for effective maximum rock size including consideration of the effect of variation of the joint dip angle. The DOE will provide the technical basis for effective maximum rock size including consideration of the effect of variation of the joint dip angle. This will be documented in revisions to the Drift Degradation Analysis, ANL–EBS–MD–000027, and the Rockfall on Drip Shield, CAL–EBS–ME–000001, expected to be available to NRC in fiscal year 2003.
RDTME.3.19	The acceptability of the process models that determine whether rockfall can be screened out from performance assessment abstractions needs to be substantiated by the DOE by doing the following: (1) provide revised **DRKBA** analyses using appropriate range of strength properties for rock joints from the Design Analysis Parameters Report, accounting for their long-term degradation; (2) provide an analysis of block sizes based on the full distribution of joint trace length data from the Fracture Geometry Analysis Report for the Stratigraphic Units of the Repository Host Horizon, including small joints trace lengths; (3) verify the results of the revised DRKBA analyses using: (a) appropriate boundary conditions for thermal and seismic loading; (b) critical fracture patterns from the DRKBA Monte Carlo simulations (at least two patterns for each rock unit); (c) thermal and mechanical properties for rock blocks and joints from the Design Analysis Parameters Report; (d) long-term degradation of rock block and joint strength parameters; and (e) site-specific groundmotion time histories appropriate for post-closure period; provide a detailed documentation of the analyses results; and (4) in view of the uncertainties related to the rockfall analyses and the importance of the outcome of the analyses to the performance of the repository, evaluate the impacts of rockfall in performance assessment calculations. DOE believes that the Drift Degradation Analysis is consistent with current understanding of the Yucca Mountain site and the level of detail of the design to date. As understanding of the site and the design evolve, DOE will: (1) provide revised DRKBA analyses using appropriate range of strength properties for rock joints from a design parameters analysis report (or other document), accounting for their long-term degradation; (2) provide an analysis of block sizes based on the full distribution of joint trace length data from the Fracture Geometry Analysis for the Stratigraphic Units of the Repository Host Horizon, ANL–EBS–GE–000006, supplemented by available small joint trace length data; (3) verify the results of the revised DRKBA analyses using: (a) appropriate boundary conditions for thermal and seismic loading; (b) critical fracture patterns from the DRKBA Monte Carlo simulations (at least two patterns for each rock unit); (c) thermal and mechanical properties for rock blocks and joints from a design parameters analysis report (or other document); (d) long-term degradation of joint strength parameters; and (e) site-specific ground motion time histories appropriate for post-closure period. This will be documented in a revision to the Drift Degradation Analysis, ANL–EBS–MD–000027, expected to be available to NRC in fiscal year 2003. Based on the results of the analyses above and subsequent drip shield calculation revisions, DOE will reconsider the screening decision for inclusion or exclusion of rockfall in performance assessment analysis. Any changes to screening decisions will be documented in analyses prior to any potential license application.
SDS.2.04	The approach to evaluate seismic risk, including the assessment of seismic fragility and evaluation of event sequences is not clear to the NRC, provide additional information. DOE believes the approach contained in the Features, Events, and Processes Analysis and Model Report will be sufficient to support the Site Recommendation. The updated Features, Events, and Processes Analysis and Model Report is expected to be available in January 2001.

Table A-1. Key Technical Issue Agreements that Pertain to the Performance Assessment of the Engineered Barrier Subsystem when Subjected to Rockfall and Seismic Ground Motions (Continued)	
Key Technical Issue Agreement Number	**NRC and DOE Agreement**
TSPAI.2.02 (Comments 34, 35, 37, 39, 78, and 79)	Provide the technical basis for the screening argument, as summarized in Attachment 2. See Comment # 3, 4, 11, 12, 19 (Parts 1, 2, and 6), 25, 26, 29, 34, 35, 36, 37, 38, 39, 42, 43, 44, 48, 49, 51, 54, 55, 56, 57, 59, 60, 61, 62, 63, 64, 65, 66, 68, 69, 70, 78, 79, J–1, J–2, J–3, J–4, J–7, J–8, J–9, J–10, J–11, J–12, J–13, J–14, J–15, J–17, J–20, J–21, J–22, J–23, J–24, J–25, J–26, and J–27. DOE will provide the technical basis for the screening argument, as summarized in Attachment 2, for the highlighted Features, Events, and Processes. The technical basis will be provided in the referenced Features, Events, and Processes Analysis and Model Report and will be provided to the NRC in fiscal year 2003.
TSPAI.3.06	Provide the technical basis for the methodology used to implement the effects of seismic effects on cladding in revised documentation. DOE will demonstrate that the methodology used to represent the seismic effects of cladding does not result in an underestimation of risk in the regulatory timeframe (ENG2.1.1). DOE will provide the technical basis for the methodology used to implement the effects of seismic effects on cladding in revised documentation. DOE will demonstrate that the methodology used to represent the seismic effects of cladding does not result in an underestimation of risk in the regulatory timeframe in Total-system Performance Assessment-License Application. The documentation is expected to be available to NRC in fiscal year 2003.
GEN.1.01 (Comment 3)	For NRC comments 3, 5, 8, 9, 10, 12, 13, 15, 16, 18, 21, 24, 27, 36, 37, 41, 42, 45, 46, 50, 56, 64, 69, 75, 78, 81, 82, 83, 93, 95, 96, 97, 98, 102, 103, 104, 106, 109, 110, 111, 113, 116, 118, 119, 120, 122, 123, 124, and 126, DOE will address the concern in the documentation for the specific Key Technical Issue agreement identified in the DOE response (Attachment 2). The schedule and document source will be the same as the specific Key Technical Issue agreement.